# Electrochemical Engineering Models of Electroanalytical Tools for Advanced Batteries

Qiu Ru Linnette Teo

A dissertation
submitted in partial fulfillment of the
requirements for the degree of

Doctor of Philosophy

University of Washington
2022

Reading Committee:
Daniel T. Schwartz, Chair
Venkat R. Subramanian
David S. Bergsman

Program Authorized to Offer Degree:
Chemical Engineering

University of Washington

## Abstract

# Electrochemical Engineering Models of Electroanalytical Tools for Advanced Batteries

Qiu Ru Linnette Teo

Chair of the Supervisory Committee:
Professor Daniel T. Schwartz
Chemical Engineering

Battery design and usage can be optimized through the use of electrochemical engineering models that detail the physicochemical processes occurring in a battery. While lithium-ion battery chemistry and models are well-established, lithium sulfur is still an active area of development and is a promising next-generation chemistry. The first part of this dissertation covers the ongoing challenges of continuum modeling of lithium sulfur, with efforts to accelerate model development using electroanalytical techniques – galvanostatic intermittent titration technique and electrochemical impedance spectroscopy (EIS). We explore the implications on thermo-kinetic parameters by modeling the thermodynamic equilibrium before adding further complexities of kinetics and transport. The second part of this work aims to improve diagnostics, sensing, and control of lithium-ion batteries by modeling a novel technique, dynamic EIS.

# Contents

# List of Figures

# List of Tables

# Acknowledgements

The work in this dissertation is the culmination of years of time and effort that a great number of people have put it to support me. I am deeply grateful to everyone who has helped me in one way or another. To my co-advisors, Venkat and Dan, thank you for giving me the opportunity to learn from the best of both worlds and I hope that this work will reflect that. Venkat, I really appreciate your support throughout my PhD. I have always been impressed by your love of math and algorithms and have learnt so much from you. Dan, thanks for being such a great mentor, training me to be an electrochemist, and always being excited about the work that we do. I appreciate all our conversations and your advice. My committee members, David and Corie, for your thoughtful feedback and taking the time to be on my committee.

I would also like to thank all past and present iterations of both my two labs, the EMI/Schwartz lab and Maple/Subramanian group. Every one of you have taken the time to help me out in some way and I have learnt a lot from all of you – Victor, Erica, Matt, Mihuyn, Rose, Yue Fan, Caitlin, Manan, Yanbo, Taejin, Maitri, Seongboem, Neal, Mengdi, Akshay, Surya, Krishna, Jerry, Lubhani, Kirutiga, and Chintan. All of you have made going through the whole journey a lot more fun and memorable. Shoutout to Victor and Erica for being part of my grad school family who I can go to for anything. Caitlin, for teaching me everything I know on LiS and being a great friend outside the lab (I miss Tuesday date nights). Manan, for getting me started and teaching me what a battery is. Thanks for always being willing to answer all my questions and making us delicious Indian food. Also thank you to honorary members, Luke, Olaf, & Biraj, for fun times, and also all other ChemEs and ECS buddies for being part of this journey.

Thank you too to all my Seattle friends for being part of my life and making Seattle feel more like home, special shout out to friends I quarantined with who are now my poker buddies – Raffi, Mira, Rob, Liz, Kevin, Cassandra. Singapore buddies and my first friend in Seattle, Zack. Frisbee friends past and present, especially Addie for always being a phone call away. Thank you Chris for being so patient, understanding, and supportive. And of course, my family, I appreciate your support over the many, many years that I have been in school and for valuing my education.

# Chapter 1: Introduction

Advanced battery technology currently plays an important role in the transition to renewable energy by enabling the electrification of transportation and short-term intermittent energy storage. To accelerate adoption, efforts are concentrated on material design improvement and better optimization of battery usage, both which benefit from being guided by powerful analytical tools. This work aims to connect electroanalytical measurements with computationally efficient physics-based models for lithium-ion and lithium sulfur batteries.

## 1.1 Battery chemistries

### *Lithium-ion batteries*

Lithium-ion is a well-established chemistry, with the inventors being recognized with the Nobel Prize in Chemistry in 2019 due to the prevalence of the technology in our society. Rechargeable lithium-ion batteries were first conceptualized in the 1970s, with the first cell being commercialized in 1991. Typically, a graphite anode is paired with a lithium metal oxide cathode, and the two electrodes are separated by a porous membrane separator. The electrolyte is conventionally an organic solvent, e.g., ethyl carbonate or dimethyl carbonate. Lithium-ion batteries operate due to insertion chemistry, where the lithium-ions move between the two electrode materials and are stored, or intercalate, into interstitial sites. When discharging a battery, the lithium-ions deintercalate from the layered anode structure, migrate across the separator, and into the cathode. This happens due to the difference in thermodynamic potential of the two electrodes, and as the lithium-ions move across the cell, electrons flow from the anode to cathode in the external circuit, driving a current. The opposite happens when the battery is being charged.

### *Lithium sulfur batteries*

Current lithium-ion technologies deliver energy densities around 150-200 Wh/kg while efforts focused on promising next generation chemistries include lithium sulfur with the ability to deliver energy densities higher than 500 Wh/kg. The theoretical capacity of the lithium sulfur anode is

1675mAh/g.[1] Coupled with a lithium metal anode, the theoretical gravimetric energy density of a lithium sulfur cell is 2500 Wh/kg.[2] The lithium sulfur chemistry is much more complicated than the relatively simple lithium-ion chemistry. It uses a conversion mechanism, which means that the cathode material undergoes chemical, phase, and structural transformations. The cathode is made of a composite of solid sulfur and conductive carbon. Under discharge, the solid sulfur dissolves and is reduced to higher order polysulfides that are soluble in the electrolyte. These species can then undergo a complex scheme of reduction, dissociation, or disproportionation reactions to lower order polysulfide intermediates. The final product, typically $Li_2S$, is insoluble in conventionally used ether-based electrolytes, dimethoxyethane (DME) and dioxolane (DOL).

While sulfur cathodes are close to commercialization, there are still fundamental challenges to overcome such as poor cycle life, high self-discharge rates, and limited power capability. These limitations are tied to the low electrical conductivity of sulfur and the polysulfide shuttle effect, where the sulfides from the cathode diffuse and react with the lithium metal anode.[3]

## 1.2 Battery models

Since batteries are closed, sealed systems, with the only measurable variables being current, voltage, and temperature, battery models are important to predict behavior and performance, including metrics such as state-of-charge (SOC) and state-of-health (SOH). Some detailed physics-based models can also be used to understand the internal physical processes occurring in the battery. For example, we can model the concentration of lithium-ions as a function of space and time, with higher concentration gradients build up leading to higher overpotentials that may drive degradative processes. Models can also be used to inform cell design, and also to guide battery usage through control and optimization techniques. Battery models can range in complexity and computational requirements – a few general types will be discussed below.

### *Equivalent circuit models*

Empirical models or equivalent circuit models (ECM) are most commonly used in battery management systems (BMS) for battery packs. BMS monitor, control, and estimate the SOC of the battery. ECMs use components like resistors and capacitors to model the battery as an electrical circuit. They are widely utilized due to their low model complexity (5-10 parameters) while being able to predict most battery behavior. When circuit elements are incorporated in a physically analogous manner to processes occurring inside a battery, ECMs are easily interpretable and fast to solve. However, they are also easy to overfit and may lose physical meaning and interpretability as processes and parameters are lumped together. The reduced order nature of ECMs make it a useful analytical tool but less of an accurate predictive tool for operating under different conditions or with new design parameters.

### *Continuum models*

There are also continuum models that model physiochemical processes occurring in a battery using fundamental transport, kinetics, and thermodynamic equations. The most common models used by lithium-ion battery researchers are the single particle model and the porous electrode pseudo-two-dimensional P2D model. The single particle model treats each electrode as a single particle. Diffusion of lithium-ions in the solid phase is modeled using Fick's law of diffusion, while Butler-Volmer kinetics is used for the electrochemical reactions. Notably, electrolyte concentration is not modeled and hence the model is less accurate when simulating high charge/discharge rates.

The Doyle-Fuller-Newman (DFN) P2D model is an isothermal electrochemical model that is widely used in the literature due to a good balance between accuracy, complexity, and CPU time. It is a considered the standard in battery research due to its inclusion of key physical processes and ability to provide understanding of batteries on a continuum level. It describes the behavior of a lithium-ion cell sandwich which consists of the two porous electrodes, a separator, and current collectors. It is based on porous electrode theory and involves the solution and solid phases – electrolyte in pores and spherical particles that make up the electrode material matrix – to be treated as superimposed continua. Diffusion of lithium-ions in both phases are considered, along with Ohm's law for the potentials, and Butler-Volmer kinetics for the pore wall flux. Concentrated solution theory is used to describe concentration and potentials in the electrolyte. The variables that are solved are potentials and concentrations in the solid and solution phases for the anode, separator, and cathode. An example of the full set of governing equations can be found in

***Table 5.5*** and there are ~25 parameters needed. The impedance form of this P2D model has been developed by Meyers, Doyle, and Newman and further impedance models developed in this work are largely built on this effort.[4,5]

Similarly, there are also a range of continuum-level lithium sulfur battery models, from microscale to macroscale, and zero- and one-dimensional models. This will be reviewed in detail in Chapter 2. While the P2D model for lithium-ion has well-established governing equations and parameters, continuum models that model the behavior of lithium sulfur cells are still in the developmental phase. The exact reaction mechanism of this complex chemistry is still up for debate and new research is still underway in developing better models that improve the modeling of the reaction scheme, precipitation reactions, transport behavior and more. Furthermore, due to sulfur chemistry having multiple species and phases, a standard 1D porous electrode model has ~40+ parameters, with many being assumed or adjusted without experimental or computational backing. The community's current metric for model validation is to fit the model to a discharge curve and observe trends at different discharge rates. In this dissertation, we hope to address some of these issues by using other analytical tools beyond discharge curves.

### *More detailed models*

We can certainly add more physics to increase the fidelity of a model, though at greater computational cost and increased complexity. For instance, there are 3D models, thermal models, and stress-strain models. Atomistic models such as Kinetic Monte Carlo, molecular dynamics, and quantum chemistry also allow for more detailed understanding of atomistic level interactions. These models are typically solved offline and beyond the scope of this work. Ref 6 provides a good summary. In Chapter 2, we also cover the importance of coupling atomistic models to continuum-level models for lithium sulfur systems, by taking calculated molecular properties as input bulk parameters.

## 1.3 Electroanalytical tools

Electroanalytical tools are useful to separate the many complex physical phenomena occurring during a typical operation of a battery by isolating one or a few dominating processes. As mentioned above, a battery model with full physics can have more than 20 parameters for a lithium-ion system and more than 40 parameters for lithium sulfur. A typical voltage curve of a battery charging, or discharging, is not sensitive to all the parameters. Isolating processes and making electroanalytical measurements can give us information about a few specific parameters. For example, we can carry out a galvanostatic intermittent titration technique (GITT) experiment find the diffusion coefficient of lithium-ion in a specified electrode material.

Analytical tools can also be used as diagnostics for batteries. We can take measurements at various SOCs and SOHs of the battery or under different operating conditions to gain insight on what is occurring internally. Changes in the measurement signal can be connected to the changing internal processes, and with a suitable physics-guided model, we can fit experimental data to a model to track changing parameters. A few examples of analytical measurements commonly used in batteries are discussed in this work.

*Galvanic Intermittent Titration Technique (GITT)*

GITT is carried out by applying a series of current steps during charge or discharge, each followed by a period of relaxation where the current is turned off. The voltage is allowed to relax to an equilibrium value during this time. For insertion chemistry such as lithium-ion, GITT is commonly used to find diffusivities as that can be assumed as the limiting or dominant behavior. For lithium sulfur batteries, experimental GITT has not been used to find diffusivities, though simple, model systems have been explored using GITT for this purpose.[7] Experimental GITT carried out on lithium sulfur batteries are mainly used to find the internal resistance as a function of voltage,[8] or to find the thermodynamic equilibrium voltage. The thermodynamic equilibrium voltage obtained using GITT has been used to compare different electrolyte systems,[9] to compare overpotentials due to different electrolyte to sulfur ratios (E/S),[10] or to understand $Li_2S$ precipitation.[11]

*Electrochemical impedance spectroscopy (EIS)*

Electrochemical impedance spectroscopy (EIS) is typically carried out by perturbing an electrochemical system at steady-state with an input AC modulation (current or voltage) and measuring the resulting response. This is a widely used diagnostic tool due to its powerful ability to ascribe separate physical processes based on their timescales. A requirement of EIS is that the modulation amplitude is small to ensure a linear response, and this also makes the method non-destructive for use in battery systems. EIS has been applied to both lithium-ion and lithium sulfur batteries to obtain kinetic and mass transport parameters,[12] observe aging effects,[13] and track growth of passivation layers.[14]

*Dynamic EIS*

A fundamental condition for EIS is that the system exhibits stationarity, i.e., the cell must be operating at a steady periodic state. For a closed system like a sealed battery, stationarity requires the cell to be relaxed to an equilibrated state, with no applied DC current, before the AC current of an EIS measurement is applied. Transient impedance-like signals can be measured in sealed cells being discharged or charged – a technique sometimes call dynamic EIS (DEIS). Variations of this technique has been carried out on lithium-ion battery systems to investigate deviations between dynamic and stationary charge transfer resistance,[15,16] and solid-electrolyte interphase formation.[17,18] Understanding these deviations will help inform how we can use DEIS while the battery is in operation for optimization and control purposes.

## 1.4 Numerical methods and model reformulation

The work in this dissertation employs mathematical tools that speed up computation and solving of these complex models. This makes computation of such systems more accessible with the eventual goal of online computation for control applications in some scenarios, where computations solved in milliseconds or seconds are needed.

The 1D physics-based battery models used contain coupled sets of differential algebraic equations (DAE). The governing equations in the P2D model for a typical lithium-ion battery cell sandwich is a system of 10 nonlinear coupled partial differential equations (PDE) with two spatial coordinates, $x$ and $r$, and a time coordinate $t$. There are also highly nonlinear algebraic expressions (AE) to describe the transport and kinetics. For the full 1D lithium sulfur model, we have 20 PDEs and 3 AEs with only one spatial dimension $x$. To aid computation, the equations can be rescaled by the length of each region (length of electrode/separator and particle size) by coordinate transformation such that length scales go from 0 to 1.

The next step in model reformulation would be to discretize the PDEs to ordinary differential equations (ODE). Typical discretization methods include finite difference methods, which to solve with sufficient accuracy, would result in ~3000-10,000 DAEs. In this work, the numerical method used to discretize the equations in space is orthogonal collocation, where each dependent variable is described by a sum of orthogonal polynomial functions. This method is detailed by Northrop et al.[19] and converges faster than finite difference approaches, resulting in <100 DAEs. Methods developed by the Subramanian group to ensure consistent initialization and robust computation of nonlinear DAE systems are used.[20]

## 1.5 Scope of the dissertation

This dissertation aims to show the value of modeling electroanalytical tools in lithium sulfur models that are in the developmental phase and lithium-ion models which are more established.

In Chapter 2, we conduct a comprehensive literature review highlighting the essential components of lithium sulfur modeling. We make a distinction between macro- and microscale continuum models and examine how they can inform or be validated by different types of experiments, including electroanalytical ones. The research areas highlighted include reaction mechanisms and speciation, charging and reversibility, nucleation and precipitation, microscale models of the cathode, degradation and the shuttle phenomena, and transport effects of concentrated solutions at low electrolyte-to-sulfur (E/S) ratios. The efforts towards optimization and parameter estimation are also reviewed. We believe this review emphasizes the unique role continuum modeling plays and the greater collaboration needed between continuum modelers, other scales of modeling, and experimental work.

In Chapter 3 and 4, we focus on the thermodynamics and kinetics underlying the reaction mechanisms modeled and try to use systems level metrics such as E/S ratios that are relevant for commercially viable high energy density lithium sulfur batteries. We show that looking at the fundamental thermodynamics underpinning the system is valuable as a starting point before building more complicated models and hence introduce a new model that solves for the thermodynamic equilibria of a lithium sulfur cell in Chapter 3. The thermodynamic equilibria and transient kinetic relaxation behavior can be found experimentally through GITT, and in this chapter, we simulate GITT experiments to explore these. This is a relatively simple experiment to carry out to uncover fundamental thermo-kinetic parameters which are affected by the speciation and solubility of polysulfides. Specifically, we explore $Li_2S$ precipitation and $S_6^{2-}$ to $S_3^{\bullet-}$ dissociation chemistry. This has implications for accelerating cell design and optimization, particularly in furthering our understanding of thermo-kinetic parameters in relation to solvent engineering.

In Chapter 4, we look at modeling EIS of lithium sulfur cells. EIS measurements can be used to characterize electrochemical processes occurring in the system by timescale and give insight on the evolution of mechanisms as the cell degrades.[21] We show ability to simulate EIS spectra using sophisticated numerical techniques and analyze these spectra over a wide range of frequencies. We also compare the EIS of a 0D model without transport effects and a 1D model with transport effects.

In Chapter 5, we shift the focus to the more established lithium-ion battery models and explore a novel diagnostic technique, dynamic EIS (DEIS). DEIS experiments have shown deviation in dynamic compared to stationary impedance in lithium-ion battery systems. In this work, we develop two computational approaches based on the DFN P2D model to explore the value and interpret effects of dynamic operation. The first method is a brute force time domain calculation followed by short-time Fourier transform. The second method is a fast-computing method that separates the timescales of the AC measurement and the DC charge/discharge to compute dynamic impedance. This second method allows us to easily explore the physics that drive differences between stationary and dynamic signals, and to highlight the sensitivity of diagnostic DEIS signals to interfacial processes at each electrode. We show that a possible use case for this technique is a 1 Hz DEIS diagnostic signal during charging as a sensitive end point indicator to prevent lithium plating.

# Chapter 2: Progress on Continuum Modeling of Lithium Sulfur Batteries

*Note: this chapter was published as an article*

Parke, C. D[=].; Teo, L.[=] ; Schwartz, D. T.; Subramanian, V. R. Progress on Continuum Modeling of Lithium–Sulfur Batteries. *Sustainable Energy Fuels* **2021**, *5*, 5946–5966. https://doi.org/10.1039/D1SE01090E.[22]

[=] These authors contributed equally to this work.

## Abstract

While lithium sulfur batteries are a promising next-generation chemistry due to their high theoretical energy density, commercialization has been slow due to low coulombic efficiency and poor cycle life. This review explores the ways in which continuum modeling contributes to the understanding of lithium sulfur (LiS) battery mechanisms and cell-level performance through the lens of micro- and macroscale phenomena. We examine different approaches to modeling important physical phenomena such as reaction mechanisms, cathode microstructure, shuttling, nucleation and precipitation, and transport limitations. This paper also emphasizes the significance and challenge of connecting typical modeling parameters and assumptions to systems-level metrics of a standard state-of-art high performing lithium sulfur cell. Particularly important, the considerations for high energy density cells and the areas where continuum models can facilitate better collaboration are discussed. We also summarize a few selected works to highlight experimentally-driven modeling, use of electroanalytical techniques, and parameter identification approaches to enable model-based design and advanced battery management systems.

## 2.1 Introduction

Research on lithium sulfur (LiS) batteries has increased as electric transportation scales-up, with a push for higher energy density chemistries and elimination of costly, low abundance, or insecure commodity materials from the battery supply chain. Lithium sulfur batteries are projected to have about 3 times the energy density of lithium-ion batteries. Sulfur as a cathode material is cheap and abundant, two important considerations for both cost and supply chain availability.[3] Despite their promise, many challenges have slowed the commercialization of these batteries. Development of the lithium anode has been fraught with safety concerns and poor capacity retention.[23] During cycling, the sulfur cathode produces soluble polysulfide species that can travel to the anode and participate in deleterious side reactions, called polysulfide shuttling.[24] Efforts to control speciation and mitigate this parasitic shuttle phenomena have focused both on electrolyte engineering and protection of the lithium anode.[3,25] Additionally, the sulfur solid species within the cathode are insulating, which can lead to passivation and overall poor sulfur utilization.[26] To mitigate this, carbon and other additives are included to improve conductivity, but which decreases overall energy density. Work on nano-structured cathodes that can anchor polysulfide species to the surface have been developed to overcome this. Carbon-to-sulfur (C/S) and electrolyte-to-sulfur (E/S) ratios are important metrics for development of practical high energy density cells as calculations show that “lean” cell conditions are vital to reach these goals.[27,28]

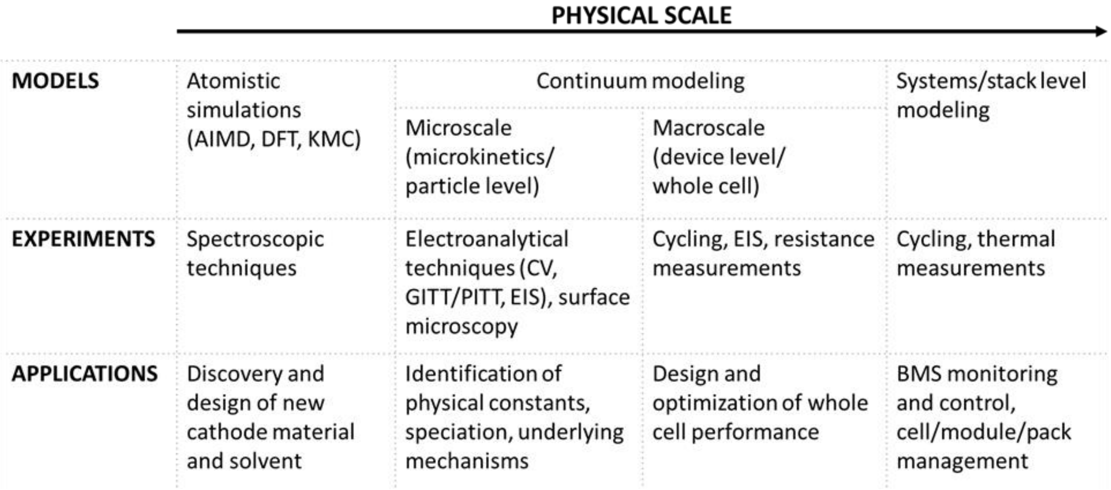

**PHYSICAL SCALE** →

| | | | | |
|---|---|---|---|---|
| **MODELS** | Atomistic simulations (AIMD, DFT, KMC) | Continuum modeling | | Systems/stack level modeling |
| | | Microscale (microkinetics/ particle level) | Macroscale (device level/ whole cell) | |
| **EXPERIMENTS** | Spectroscopic techniques | Electroanalytical techniques (CV, GITT/PITT, EIS), surface microscopy | Cycling, EIS, resistance measurements | Cycling, thermal measurements |
| **APPLICATIONS** | Discovery and design of new cathode material and solvent | Identification of physical constants, speciation, underlying mechanisms | Design and optimization of whole cell performance | BMS monitoring and control, cell/module/pack management |

***Figure 2.1 A spectrum of modeling scales that can inform and be validated by different types of experiments for various applications in the lithium sulfur field.***

Modeling can be useful to accelerate the progress of lithium sulfur battery development. Battery models span a wide range of scales from atomistic simulations on the angstrom scale all the way to packs of battery used in a vehicle on the scale of meters. The focus of this paper is on continuum modeling which lies in between these two extremes (see Figure 2.1). We can further split continuum modeling into the microscale and macroscale. Taking traditional chemical engineering reaction kinetics as an analog, there are also two scales of modeling. Microkinetic modeling focuses on breaking down reactions to elementary steps with individual activation energies and species, whereas macroscale chemical reaction modeling takes the bulk reaction rate constants and rate limiting steps to design a chemical reactor where an engineer is concerned about flow rate and product yield. Similarly, we will structure this paper by describing continuum modeling of lithium sulfur batteries using microscale and macroscale terminology. Microscale modeling is about representing key physical phenomena in a mechanistic manner to elucidate underlying mechanisms. Besides microkinetics, this can be looking at the cathode structure in greater morphological detail, modeling sub-micron level internal transport into a particle, or nucleation and growth of precipitates for example. This kind of modeling on the microscale can be aided by electroanalytical experiments (e.g., cyclic voltammetry (CV), galvanostatic or potentiostatic intermittent titration techniques (GITT/PITT), electrochemical impedance spectroscopy (EIS)) to identify physical constants and speciation, specialized setups like rotating disc electrodes, or microscopy to probe surface and structure evolution. Macroscale modeling is on the scale of whole cell and device level and is focused on modeling effective properties to relate to overall cell performance such as voltage curves. Macroscale models are typically used to explore experimentally-relevant conditions by revealing how important cell parameters like thickness, porosity, and sulfur loading impact the internal states of the battery, such as the speciation, kinetics, and transport, without the time and cost of traditional experiments. Modeling can explore design space and optimize for multiple metrics at once, which can point experimentalists in a new direction.

Continuum modeling covers a broad range of possible applications and is an exciting field as it can tie in with the opposite two ends of the modeling spectrum. Atomistic simulations such as *ab initio* molecular dynamics (AIMD), density functional theory (DFT), and kinetic Monte Carlo (KMC) techniques can perform first principles calculations and simulations on fundamental interactions to determine molecular properties like surface and absorption energies, transport properties, or reaction pathways that can be used as a parameter to be varied in continuum modeling to aid solvent engineering, for example. On a systems/stack level, for applications like a battery management system (BMS) in a vehicle's battery pack, continuum models are used for monitoring and control, computationally efficient macroscale continuum models for a cell can be extended to more extensive module and pack level systems. In this review, we highlight the areas where continuum models have collaboratively improved understanding of lithium sulfur batteries and touch on other areas where further model development is key.

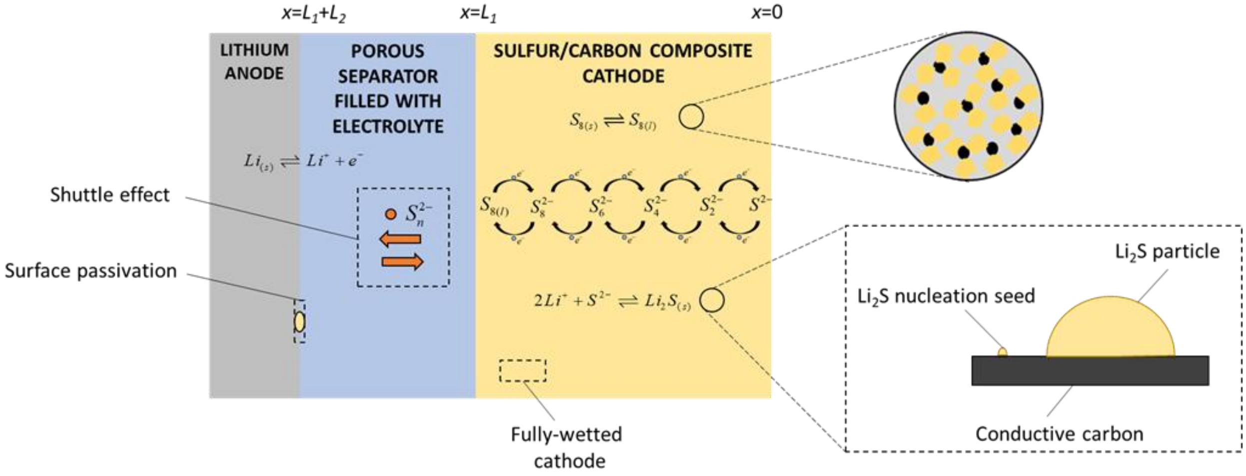

***Figure 2.2 Schematic of lithium sulfur sandwich layer with lithium anode, porous separator, and composite cathode with yellow solid sulfur particles, black conductive carbon, and binder. The reaction scheme in the cathode is a commonly proposed formulation but is by no means the best formulation. Other processes that can occur is $Li_2S$ film formation in the cathode through a nucleation and growth process, shuttling of polysulfides across the cell, and the resulting surface passivation at the anode.***

In continuum modeling, the lithium sulfur cell can be thought of as having three domains to be modeled as a cell sandwich - the lithium anode, porous separator, and composite cathode - as seen in Figure 2.2. For a fully charged cell, the cathode starts off as a composite of solid $S_8$(s) and carbon particles with assumed uniform porosity (more complex cathode morphology will be discussed in the Cathode Structure section). The solid sulfur dissolves and is electrochemically reduced through a series of cascading steps to lower order polysulfides. The 5-step reduction mechanism shown in Figure 2.2 is a popular proposed scheme and simplifications/variations are discussed later. The higher order polysulfides are typically soluble in conventional electrolytes while the lower order polysulfides such as $Li_2S$ and sometimes $Li_2S_2$ are insoluble products. Solid products such as $Li_2S$ form as a film on the cathode and surface passivation of the carbon structure occurs towards the end of discharge. Shuttling also occurs which is when the dissolved polysulfides are transported back and forth between the two electrodes and can be reduced at both. A resulting phenomenon of shuttling is surface passivation at the anode which results in irreversible capacity loss. In this work, we will review papers that model cathode structure, nucleation and growth of solid products, shuttling, and degradation processes such as anode passivation. We will also relate models with experimental trends observed, and importantly, experimental design and metrics. For macroscale models to be deemed useful, simulated voltage discharge curves are typically compared to that of high-performance experimental cells, where the three key features are: two voltage plateaus and a voltage dip and recovery as a transition between the two plateaus (refer to Figure 2.3b and Figure 2.4 for examples). This dip, or negative differential resistance, is normally attributed to solid nucleation processes which we will describe further in the Precipitation section. This review will cover both lumped/zero-dimensional (0D) models, and one-dimensional (1D) models, where 1D models capture the spatial variation in each domain, and 0D models generally only model the cathode as a singular point. The typical equation set for the 1D model is shown in Table 1, which describes the thermodynamics, kinetics, and transport detailed by Kumaresan et al.[29] Included within Table 1 are degradative redox reactions from polysulfide shuttle, taken from Mistry and Mukherjee (detailed within Shuttling, degradation, and lithium anode dynamics).[30]

***Table 2.1 1-D Lithium Sulfur Mathematical Discharge Model***

| Governing Equations | Boundary Conditions |
|---|---|
| Positive Electrode (Region 1) | |
| $\frac{\partial \varepsilon_1 C_{1,i}}{\partial t} = -\frac{\partial N_{1,i}}{\partial x} + r_i - R_{1,i}$ | $N_{1,i}\big\|_{x=0} = 0$ |
| $N_{1,i} = -D_{1,i}\frac{\partial C_{1,i}}{\partial x} - z_i \frac{D_{1,i}}{RT} F C_{1,i} \frac{\partial \phi_{1,e}}{\partial x}$ | $-\sigma \frac{\partial \phi_s}{\partial x}\Big\|_{x=0} = i_{app}$ |
| $i_s = -\sigma \frac{\partial \phi_s}{\partial x}$ | $i_{1,e}\big\|_{x=0} = 0$ |
| $i_{1,e} = F \sum_i z_i N_{1,i}$ | |

$$\frac{\partial \varepsilon_{1,k}}{\partial t} = \tilde{V}_k R'_k$$

$$\frac{\partial \varepsilon_1}{\partial t} = -\sum_k \tilde{V}_k R'_k$$

Separator (Region 2)

$$\frac{\partial \varepsilon_2 C_{2,i}}{\partial t} = -\frac{\partial N_{2,i}}{\partial x} - R_{2,i}$$

$$C_{1,i}\Big|_{x=L_1} = C_{2,i}\Big|_{x=L_1}$$

$$N_{2,i} = -D_{2,i}\frac{\partial C_{2,i}}{\partial x} - z_i \frac{D_{2,i}}{RT} F C_{2,i} \frac{\partial \phi_{2,e}}{\partial x}$$

$$i_{1,e}\Big|_{x=L_1} = i_{2,e}\Big|_{x=L_1}$$

$$i_{2,e} = F\sum_i z_i N_{2,i}$$

$$N_{1,i}\Big|_{x=L_1} = N_{2,i}\Big|_{x=L_1}$$

$$\frac{\partial \varepsilon_{2,k}}{\partial t} = \tilde{V}_k R'_k$$

$$-\sigma \frac{\partial \phi_s}{\partial x}\bigg|_{x=L_1} = 0$$

$$\frac{\partial \varepsilon_2}{\partial t} = -\sum_k \tilde{V}_k R'_k$$

Anode/Separator Interface with Shuttle Equations

$$i_{2,e}\Big|_{x=L_1+L_2} = F\sum_i z_i N_{2,i}$$

$$N_{2,Li^+}\Big|_{x=L_1+L_2} = \frac{i_{iapp}}{F} + r'_i$$

$$N_{2,i}\Big|_{x=L_1+L_2} = r'_i$$

$$\phi_s\Big|_{x=L_1+L_2} = 0$$

$$r'_i = \sum_j s_{i,j} k'_j \left(\frac{C_i}{C_i^{ref}}\right)^{s_{i,j}}$$

$$k'_j = \frac{i_{0j}}{F}\exp\left(-\frac{F\eta}{2RT}\right)$$

Other Expressions

$$r_i = -a\sum_j \frac{s_{i,j} i_j}{n_j F}$$

$$a = a_0\left(\frac{\varepsilon}{\varepsilon_{initial}}\right)^{\xi}$$

$$\frac{\partial i_s}{\partial x} + \frac{\partial i_e}{\partial x} = 0$$

$$\frac{\partial i_e}{\partial x} = a\sum_j i_j$$

$$\eta_j = \phi_s - \phi_e - U_{j,ref}$$

$$U_{j,ref} = U_j^{\theta} - \frac{RT}{n_j F}\sum_i s_{ij}\ln\left[\frac{C_{i,ref}}{1000}\right]$$

$$R_i = \sum_k \gamma_{i,k} R'_k \qquad R'_k = k_k \varepsilon_{1,k}\left(\prod_i C_{1,i}^{\gamma_{i,k}} - K_{sp,k}\right) \qquad D_i = \varepsilon^{\xi} D_{i0}$$

$$i_j = i_{o,j_{ref}}\left\{\left(\frac{C_{i,anodic}}{C_{i,ref}}\right)^{s_{a,j}}\exp\left(\frac{\alpha_{a,j}F}{RT}\eta_j\right) - \left(\frac{C_{i,cathodic}}{C_{i,ref}}\right)^{-s_{c,j}}\exp\left(-\frac{\alpha_{c,j}F}{RT}\eta_j\right)\right\}$$

## 2.2 Cathode Reaction Scheme

There are two different commonly employed reduction schemes for the sulfur cathode. The first scheme employs the two reactions shown below.

$$S_{8(l)} + 4e^{-} \rightleftharpoons 2S_4^{2-} \tag{2.1}$$

$$S_4^{2-} + 4e^{-} \rightleftharpoons 2S^{2-} + S_2^{2-} \tag{2.2}$$

This simple reduction scheme was first shown in the work by Mikhaylik and Akridge in a lumped model.[31] Other lumped or simplified 1D models[32–34] employed the same reaction scheme but included chemical reactions of $S_8$ dissolution or precipitation of $Li_2S$. In general, the relatively simple reaction scheme is used for the express purpose of predicting trends and ease of parameterization. The voltage curve only qualitatively matches the relevant features, like the two plateaus and voltage dip. Work by Erisen et al.[34] concluded that modeling the first plateau with a single reaction does not adequately describe the behavior and that the presence of several long-chain polysulfides are needed to replicate the first plateau more quantitatively. Using this simple reduction scheme inadequately describes the complexity of the chemistry at play but can be very useful to understand trends due to the low computational footprint. This is an example of macroscale continuum modeling where deliberate approximations are made to simply match key experimental traits of a voltage curve.

On the other hand, microscale modeling aims to break down this reaction scheme to the most accurate representation. A more complex reduction scheme was proposed in the model by Kumaresan et al.[29] In contrast to the earlier work by Mikhaylik, the reaction scheme included a 5-step reduction of sulfur from dissolved $S_8$ to $S^{2-}$. This 5-step reduction is a step towards a more microscale understanding of the reaction scheme by breaking down the lumped steps further. The electrochemical reaction steps are shown in Figure 2.2. For each of the charged polysulfides, the model includes precipitation of $Li_2S_n$(s). Other models have tweaked this reaction scheme. For example, some models only consider $Li_2S$(s) and occasionally $Li_2S_2$(s) because there is still debate about the presence of other solid precipitates.[33,35,36]

This more complex reduction scheme is able to reproduce the important features of the discharge curve, but even so, it is a simplification of the complicated schemes that have been proposed, which include disproportionation and dissociation reactions with multiple pathways.[37–40] Elucidating the reaction scheme is an important step to identifying the underlying phenomena that contribute to performance limitations. We can go even further to the left of the microscale spectrum by using electroanalytical techniques and spectroscopic methods to figure out detailed speciation. CV experiments give a wealth of information about the redox behavior of electrochemical systems, and some studies have combined CV experiments with modeling to analyze the reaction scheme.

Work by Schön and Krewer[41] coupled identification of species via high performance liquid chromatography and CV experiments and modeling to analyze two proposed reaction mechanisms. The electrolyte system consisted of 1 M LiTFSI and a 1:1 mixture of 1,3-Dioxolan (DOL):DME. The simplified reaction mechanism, originally proposed by Lu et. al.,[42] is made of two electrochemical reactions and an irreversible chemical reaction (EEC); the sulfur species are left unidentified (written as X and Y) since it is empirically derived.

$$X \rightleftarrows \dots \xrightleftarrows{-5.4e^-} X^{5.4-} \tag{2.3}$$

$$X^{5.4-} \rightleftarrows \dots \xrightleftarrows{-2e^-} X^{7.4-} \tag{2.4}$$

$$X^{7.4-} \longrightarrow \dots \xrightarrow{+7.4Li^+} Y \tag{2.5}$$

When modeling CV with the EEC mechanism, the reduction and oxidation peaks are reproduced, but within the diffusion limited regime, the model predictions missed a second cathodic peak and exhibited a cathodic current not seen experimentally. The authors recommended using the EEC reduction scheme when the electrolyte composition is not relevant, such as reproducing voltage trends. In order to match the variety of species seen in high performance liquid chromatography (HPLC), the other reaction mechanism (E3C4) included three electrochemical reactions and four chemical reactions with both dissociation and disproportionation.

$$S_8 + 2e^- \rightleftharpoons S_8^{2-} \tag{2.6}$$

$$S_8^{2-} + 2e^- \rightleftharpoons S_8^{4-} \tag{2.7}$$

$$S_4^{2-} + 2e^- \rightleftharpoons 2S_2^{2-} \tag{2.8}$$

$$S_8^{4-} \rightleftharpoons 2S_4^{2-} \tag{2.9}$$

$$3S_4^{2-} \rightleftharpoons S_8 + S_2^{2-} + 2S^{2-} \tag{2.10}$$

$$2S_3^{2-} \rightleftharpoons S_4^{2-} + S_2^{2-} \tag{2.11}$$

$$2S_2^{2-} \rightleftharpoons S_3^{2-} + S^{2-} \tag{2.12}$$

The E3C4 kinetic model is able to reproduce both kinetic and transport limited behavior shown in CV experiments. The authors noted that the redox behavior varies with both SOC and direction of the current, and the disproportionation reactions were necessary to reproduce a circular conversion of shorter polysulfides to $S_{8(l)}$. This work suggests that the oxidation and reduction behavior for charge and discharge is different, and to reproduce full-cell charging behavior it may be necessary to include more complex chemistry than previously modeled. The E3C4 kinetic model is well-suited to more detailed modeling of the interplay of the electrolyte system and the speciation on the cell limitations, such as polysulfide shuttle or surface passivation by sulfur precipitates.

Recent work by Thangavel et al.[43] studied the CV behavior of a three electrode cell with a planar glassy carbon working electrode in a tetraethylene glycol dimethyl ether:dioxolane (TEGDME:DOL) electrolyte with 1 M lithium bis(trifluoromethanesulfonyl)imide (LiTFSI) and with $S_8$, $Li_2S_8$, and $Li_2S_6$ as the starting electroactive species. With a 1D model of the working electrode and adjacent electrolyte diffusion layer, the model was unable to model all the features of the redox behavior with the standard 5-step reduction scheme described previously. After the addition of an alternative reaction pathway including $S_3^{\bullet-}$ and $S_2^{\bullet-}$ radical species, the CV results were successfully reproduced, and reasonable estimates for the new reaction parameters were obtained. The added pathway includes:

$$S_8^{2-} \rightleftharpoons 2S_4^{\bullet-} \tag{2.13}$$

$$S_4^{\bullet-} + e^- \rightleftharpoons S_4^{2-} \tag{2.14}$$

$$S_6^{2-} \rightleftharpoons 2S_3^{\bullet-} \tag{2.15}$$

The CV modeling represents a promising step forward in improving the proposed reaction scheme for lithium sulfur batteries and extracting meaningful parameter values that can be further analyzed in a battery setup with sparse electrolyte amounts and high surface area electrodes.

Studies have shown that the speciation is dependent on the electrolyte system, additives, and solvent.[44] Here we highlight another example of macroscale modeling where reaction rates are adjusted to match experimentally observed cell voltage for a system with additives. Work by Shim et al.[45] combined experimental and modeling work to explore the effects of the $LiNO_3$ additive. $LiNO_3$ has been used to mitigate polysulfide shuttling by promoting a beneficial anode protective layer, thus preventing side reactions with polysulfides at the anode. However, $LiNO_3$ has been reported as negatively impacting the reduction of $Li_2S_2$ at the cathode and causing a distortion of the voltage curve and creating a third plateau. Their work found that the cells with high concentrations of $LiNO_3$ exhibited a third plateau. By controlling the exchange current density for the reduction of $S_2^{2-}$ to $S^{2-}$ and decreasing the reduction rate with excess $LiNO_3$ present, the model was able to reproduce the results seen experimentally. In the presence of excess $LiNO_3$, the model attributed the middle plateau to production of $Li_2S_2(s)$ and the third plateau as a further reduction to $Li_2S(s)$. The final two reduction reactions ($S_4^{2-}$ to $S_2^{2-}$ and $S_2^{2-}$ to $S^{2-}$) usually occur simultaneously; with excess LiNO3, the two reactions occur one at a time, causing the distinctive separation of the second plateau.

Electrolyte engineering is another important area of study as different electrolytes have been shown to stabilize different species and affect the reduction scheme. A simple experiment by the Manthiram group[46] mixed $Li_2S_6(s)$ with DOL:DME and 3 other promising electrolytes and measured the UV-vis spectra. Each of the electrolytes stabilized different species, including a commonly reported radical anion $S_3^{\bullet -}$. Parke et al.[47] explored the effects of the $S_3^{\bullet -}$ radical formation on the cell-level behavior of a battery for the first time. The reaction scheme in Figure 2.2, an E5C2 mechanism, was modified by including an additional chemical dissociation step (Eq. (2.15)) that formed $S_3^{\bullet -}$, creating a E5C3 model that matches experimentally observed speciation better. Both the thermodynamics and kinetics of radical anion formation was shown to have a dramatic effect on the voltage curve. With instantaneous kinetics, the low depth-of-discharge voltage actually increased while the rest of the curve was depressed compared to no $S_3^{\bullet -}$ chemistry. With slower kinetics, the dissociation reaction served as a sink of sulfur and resulted in reversible capacity loss. This work represents an important step in understanding the effects of electrolyte stabilization on the full-cell behavior and underlies the need for accurate thermodynamic and kinetic parameters. Such parameters could be obtained by using molecular simulations to study polysulfide stability.[48,49]

### 2.2.1 Reversibility of cathode for charging models

Most models have been able to simulate discharge voltage curves that match experimental features well. However, simulating charge curves using the same set of governing equations have proven to be challenging. Each of the electrochemical and precipitation reactions proposed in the Kumaresan model have reversible terms (see Table 1), which indicates that the model should be intrinsically reversible and be able to discharge and charge. However, Ghaznavi and Chen[50] found that the Kumaresan model[29] was unable to charge due to a low saturation concentration of $Li_2S$. In a later paper, Ghaznavi and Chen[51] varied the solubility product of $Li_2S$, $Ksp_{Li2S}$, and showed that increasing that by seven orders of magnitude, *i.e.*, a factor of $10^7$, from the commonly assumed value of $9.95 \times 10^{-4}$ $mol^3\ m^{-9}$, allowed for charging to be simulated at a low 0.02C rate. There have been no reported values of experimentally measured $Ksp_{Li2S}$ beyond the assertion of it being highly insoluble. The range of values of $Ksp_{Li2S}$ used in the modeling literature[29,52] is large and range from $10^{-5}$ to $10^7$ $mol^3\ m^{-9}$. There is a need for careful measurement of precipitation related parameters in conventionally used electrolytes for more accurate models. Perhaps, atomistic-scale simulations, such as quantum chemistry calculations or MD,[53] can inform solubility and rate constants, at least to an order of magnitude range. $Li_2S$ precipitation determines the $S^{2-}$ concentration, hence shifting the reduction potential. This shift in reduction potential has been observed in GITT experiments[11] and Zhang et al.[54] suggested that GITT might be useful to estimate precipitation rate constants and solubility products.

In terms of capturing specific features of charging curves, Ghaznavi and Chen[51] compared their simulated charging voltage curves to experimental curves and reported inability of the model to reproduce the experimentally observed sharp voltage peak at the start of charge. Their simulated charging curve also has an additional peak in the middle of charging, that can be attributed to sulfur precipitation, but is not seen experimentally. Additionally, Kumaresan model's precipitation rate expression includes the solid volume fraction of the precipitate to account for the slow nucleation process at the start of precipitation. This has been reported to be numerically unstable for precipitation when the volume fractions are close to zero. Yoo et al.[55] introduced the addition of extra aphysical terms for the precipitation reactions of $S_8$ and $Li_2S$ to overcome this challenge of numerical instability. Using the rate of change of the volume fraction of $Li_2S$, $\epsilon_{Li_2S_{(s)}}$, as an example,

$$\frac{\partial \epsilon_{Li_2S_{(s)}}}{\partial t} = V_{Li_2S_{(s)}} \left[ k_{Li_2S_{(s),1}} (C^2_{Li^+} C_{S^{2-}} - Ksp_{Li_2S}) + k_{Li_2S_{(s),2}} \frac{C^2_{Li^+} C_{S^{2-}}}{\epsilon_{Li_2S_{(s)}}} \right] \tag{2.16}$$

where $V$, $k$, $C$, are the molar volume, precipitation/dissolution rate constant, and concentration respectively, the first term on the right-hand side of Eq. (2.16) describes the precipitation rate and is the same as in Table 1, while the second is the additional aphysical term. They were able to simulate a charging curve but were not able to capture all features well.

Better parameterization of the models mentioned above might solve some of the charging challenges and numerical instabilities observed. Another possibility might be due to the proposed models having inaccurate or missing mechanisms. This can be due to the limiting phenomena being mass transfer rather than charge transfer, for example. Zhang et al.[56] used a simple 0D model with transport-limited kinetics and was the first to demonstrate the voltage kink at the start of charge (more details about this model in Transport section). It is clear that macroscale modeling is unable to fully resolve the inconsistences in charging and a deeper dive into microscale mechanistic models is necessary.

On a microscale level, for example, missing mechanisms that might help solve the charging challenge are reactions and species that are unaccounted for such as the radical species $S_3^{\bullet-}$ highlighted by Parke[47] and the fact that dissolution/precipitation phenomena are not well captured in earlier models. As discussed earlier within the Cathode reaction scheme section, CV modeling by Schön and Krewer[41] indicated different redox behavior for charge and discharge, which was replicated only with additional chemical dissociation and disproportionation reactions providing parallel pathways. With the addition of nucleation and growth phenomena to describe the precipitation process, Xiong et al.[57] were able to replicate the charging curves well (see Figure 2.3a) but they did not explore discharge. Danner et al.[52] explored both charging and discharging, but even with the addition of detailed nucleation and growth phenomena, were still unable to capture charging features well (discussed in more detail in Precipitation section). Having a comprehensive model that captures both discharge and charge features remains a major challenge. We recommend sustained efforts in developing more accurate and validated charging models, including thoughtful coordination of analytical, electroanalytical, and engineering approaches to determine trustworthy physicochemical parameters, so that continuum modeling may impact development of LiS batteries by both model-based design and performance optimization.

## 2.3 Precipitation Phenomena in the Cathode

In macroscale modeling, the voltage dip during discharge is usually described by having initially slow precipitation kinetics mimicking a nucleation overpotential where supersaturation occurs (see Other Expressions in Table 1). The precipitation rate is a function of the volume fraction of precipitate which is slow at first and as the volume fraction increases, so does the rate of precipitation. Therefore, precipitation phenomena is described macroscopically using a balance of the precipitation rate constant and solubility limit (as demonstrated in the Ghaznavi and Chen[51] parameter study mentioned in the Charging section).

This section will highlight papers that have focused on capturing the precipitation/dissolution phenomena with more detailed microscale models. Microscale continuum models that couple bulk transport and electrochemical kinetic processes with particle-level nucleation and growth theory might resolve some of the discrepancies seen between experiments and macroscale continuum models that model only model precipitation as a bulk process.

The first model to incorporate nucleation and growth to describe the precipitation reactions in a 1D lithium sulfur model is by Ren et al.[58] , who modeled $Li_2S$ precipitation as an electrochemical reaction between $Li^+$ and $S_4^{2-}$ (Eq.(2.17)) using Tafel kinetics (Eq. (2.18)), which is typically used for irreversible reactions:

$$\frac{4}{3}Li^+ + \frac{1}{6}S_4^{2-} + e^- \rightarrow \frac{2}{3}Li_2S \tag{2.17}$$

$$i_L = i_{0,L}(1-\theta)\exp\left(\frac{\alpha\eta_L F}{RT}\right) \tag{2.18}$$

where $i_L$ is the current density describing the lower voltage plateau, $i_{0,L}$ is a rate constant, $\theta$ is the fraction of surface covered by $Li_2S$, $\alpha$ is the charge transfer coefficient, $\eta_L$ is the overpotential, $F$ is Faraday's constant, $R$ is the molar gas constant, and $T$ is temperature.

They specifically assumed $Li_2S$ dissolution does not occur and hence there is no backward dissolution reaction modeled, rendering the model only applicable for discharge. In their model, the equation for nucleation rate is based on electrolytic nucleation of metals and considers overpotential for $S_4^{2-}$ adsorption, where the nucleation rate, *P*, expressed as:

$$P = P_0 (\tilde{C}_{Li^+})^{\frac{4}{3}} (\tilde{C}_{S_4^{2-}})^{\frac{1}{6}} (1-\theta) \exp\left( \frac{\alpha \eta_L F}{RT} \right) \qquad (2.19)$$

where $P_0$ is the initial nucleation rate and $\tilde{C}$ are dimensionless concentrations. For the growth portion, Ren et al. assumed hemispherical particles, used Kolmogorov phase transformation theory to account for overlap, and presented expressions for surface coverage and radial growth rate. They were able to simulate discharge curves from 0.5C to 5C and show that both plateaus are shortened, and hence higher capacity loss is seen, with increased C-rate, as shown in Figure 2.3b. In comparison with experimental data, average errors found are less than 3%. Additionally, they showed the distributions of $Li_2S$ particle radius with C-rate (Figure 2.3c). They found that at higher rates, larger overpotentials enable higher nuclei density, resulting in uniform morphology of small particles. At lower rates, growth of particles is the dominating process, which results in fewer but larger particles. This description of particle size matched SEM images of surface coverage. Analysis of the impact of initial nuclei density on specific capacity showed a non-monotonic trend, which indicates the need for optimization to balance between a high average particle size and a uniform particle distribution. By incorporating the relation between overpotential and surface coverage, Ren et al. was able to relate rate-dependent morphology of $Li_2S$ precipitation to show rate-dependent capacity trends.

Similar to Ren et al, Andrei et al.[59] used a standard set of multispecies cell-level charge and transport equations to describe the bulk and coupled that to nucleation and growth of polysulfide precipitates. They used classical nucleation theory to derive and relate the driving force of nucleation to oversaturation instead of using electrolytic nucleation that Ren et al. adopted. However, Andrei et al. demonstrated how both nucleation rate equations are mathematically similar. There were a few approximations made to reduce the number of fitting parameters and also a linear diffusive concentration gradient of polysulfides away from the carbon surface was assumed. To keep track of nuclei size distribution spatially across the cell, Andrei et al. used the differential form of Kolmogrov equation to describe surface coverage.

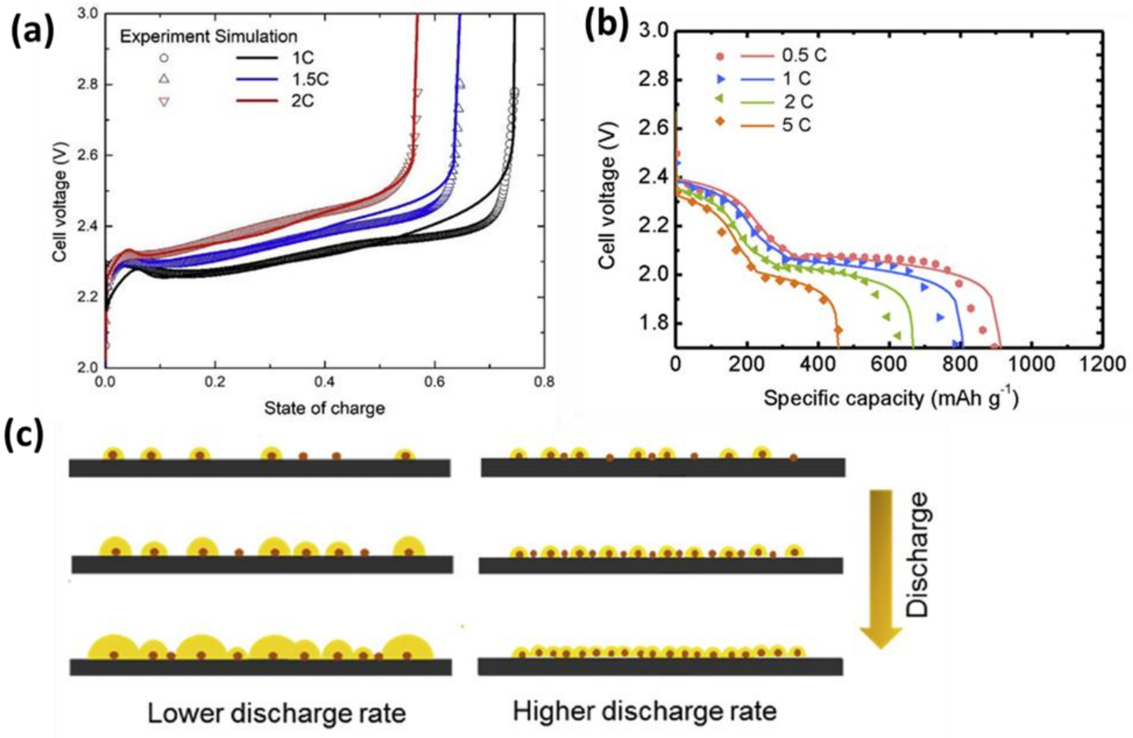

***Figure 2.3 Nucleation and growth models can reproduce the rate-dependent (a) charge and (b) discharge voltage curves. (c) For lower discharge rates, fewer Li2S nuclei form, leading to more uneven distribution of and larger particle sizes; at higher discharge rates, the nucleation rate is higher and particle growth is more uniform. (a) is reprinted from Ref [57] with permission from Electrochimica Acta. (b) and (c) are reprinted from Ref [58] with permission from the Journal of Power Sources.***

Upon qualitative comparison to experimental data, simulations by Andrei et al. were able to match the trend of discharge capacity decreasing with increasing rate for 0.1C to 1C. They were able to attribute this trend to cathode passivation due to solid products by showing surface coverage and number of $Li_2S$ nuclei changing during discharge, with complete surface coverage occurring earlier for higher rates. They also explored supersaturation trends during discharge and advised for the use of an electrolyte that enables high solubility of intermediate polysulfides to prevent intermediate products from forming on the cathode surface and taking a long time to dissolve (though this might contribute to higher degradation from shuttling phenomena). Through a variable discharge rate experiment, they found that different dynamics of nuclei growth occur at different C-rates. Their simulations matched their experiment qualitatively, and they were able to ascribe the difference in rate of surface coverage to different starting points of nucleation.

The previous two models look at the impact of adding more detailed precipitation expressions to describe discharge, while Xiong et al.[57] focused on modeling the charging process. Their model introduced the concept of a redox mediation phenomenon during rate-dependent $Li_2S$ dissolution based on experimental evidence.[37,60] They start with an assumption of a bimodal particle size distribution where small and large $Li_2S$ particles are distributed evenly at the beginning of charge. Dissolution of the $Li_2S$ particles is modeled as an electrochemical oxidation process to $Li_2S_4$, which is further oxidized to $Li_2S_8$.

$$\frac{4}{3}Li_2S \rightleftharpoons 2Li^+ + 2e^- + \frac{1}{3}Li_2S_4 \tag{2.20}$$

$$2Li_2S_4 \rightleftharpoons 2Li^+ + 2e^- + Li_2S_8 \tag{2.21}$$

$Li_2S_8$ is further oxidized and eventually precipitates out as $S_8$ solid.

$$Li_2S_8 \rightleftharpoons 2Li^+ + 2e^- + S_{8(l)} \tag{2.22}$$

Since the small particles have a larger specific surface area, the dissolution process is faster than the larger particles. A second dissolution reaction is modeled and termed as a redox mediation reaction where the oxidized $Li_2S_8$ in solution reacts with and promotes the dissolution of $Li_2S$ solids.

$$Li_2S_8 + \frac{4}{3}Li_2S \rightleftharpoons \frac{7}{3}Li_2S_4 \tag{2.23}$$

This second dissolution mechanism only occurs for the larger $Li_2S$ particles and is independent of cell potential. Similar to the previous two models, this additional precipitation/dissolution phenomenon is coupled with 1D bulk transport in dilute solution with standard mass and charge conservation expressions. They have an additional equation to track $Li_2S$ particle size growth and growth is assumed to be the same across the cathode.

Xiong et al. were able to simulate charging curves that mostly match experimental curves from 1C to 2C, shown in Figure 2.3. Specifically, they were able to simulate the charging curve with a spike at the beginning that they attribute to higher activation overpotentials due to limited surface area from the large particles. They varied the redox mediation reaction rate to show the effect on voltage and particle size. They also performed simulations with the redox mediation reaction and without. Without this reaction, there are two voltage plateaus seen with the high voltage plateau duration correlated to the volume fraction of large particles. In experimental charging curves with only one voltage plateau observed, they conclude that the charging process differs from the discharge process, where two plateaus are commonly observed, as the large particles dissolve through a redox mediation reaction instead of oxidation.

Danner et al.[52] explored fully reversible nucleation and growth through both charging and discharging while keeping track of the particle size distribution of $S_8$ and $Li_2S$. They used a two-step classical theory of nucleation and growth to model precipitation/dissolution with the diffusion-limited nucleation rate based on free energy of formation. The nucleation rate is also dependent on the number of nucleation sites, affinity of nucleation to different material surfaces, and specific surface area. The growth step is radial and described as a two-step diffusion to and reaction on the particle surface. Again, the nucleation and growth mechanisms are coupled to 1D bulk mass and charge transport governing expressions through species concentrations and active surface area. This model also includes electrochemical double layer charging at the solid-electrolyte interface and uses an empirical correlation relating electrolyte viscosity to total sulfur concentration. It is worth noting that Danner et al. made a good attempt at explaining where each set of parameters comes from.

The simulations from Danner et al.'s model for discharge curves and particle size distributions only match experimental cycling and *operando* XRD data[61] in a qualitative manner (at C/5 and C/10). Surface energy was found to be the most important parameter in a sensitivity analysis with respect to cell capacity. Ability to model the surface energy through atomistic simulations, and to model the impact of changing this surface energy parameter in the above continuum model, can help in selection of electrolyte additives which can modify surface energy. Danner et al. also carried out a PITT simulation and found that almost all the $Li_2S$ particles nucleate and form in a short time period after the maximum supersaturation is reached. This time period occurs during a long constant voltage period slightly above 2.1V, and similar voltage/current behavior has been observed in the experimental literature.[62] PITT experiments, and also simulations, can be useful to look at the minimum overpotential for nucleation initiation that might vary with surface or E/S ratio.

Danner et al. then used the same parameters fit from the discharge curves to simulate charge curves, which do not match experimental voltage data well, thus highlighting a parameter or mechanism discrepancy. However, the final particle distribution size of $S_8$ match well with *operando* XRD,[61] and most $Li_2S$ dissolves before $S_8$ precipitates. The simulated charging curves show two distinct plateaus at all C-rates with the first voltage plateau being most sensitive to $Ksp_{Li2S}$. The authors also simulated a shallow cycling experiment - discharge to 2.2V and charge using varied C-rates - and found that the small $S_8$ nucleation feature seen in the upper plateau disappears with increased C-rate due to high overpotentials. Also, at increased C-rates, there is less time to grow and so the $S_8$ particles are smaller, which agrees with the XRD literature.

All the above models are able to show a decrease in specific capacity with increased rate and attribute ability to predict rate-dependent capacity to the addition of more descriptive nucleation and growth mechanisms. Ren et al. and Xiong et al., both papers from the Zhao group, are able to fit their models to experimental data well as opposed to in a qualitative manner. They also model dissolution/precipitation of $Li_2S$ as an electrochemical step while Andrei et al. and Danner et al. use chemical reactions. A common idea proposed that could utilize these precipitation models to maximize capacity is to seed the carbon electrode surface with preferential adsorption sites or nucleation seeds. This can be done by adding doped sites with high affinity towards $Li_2S$ [52] or catalyst particles.[59] Modeling can be used to optimize the number of initial nucleation sites by striking a balance between size and number of nuclei to promote uniform growth, maximize specific surface area, and prevent large surface oversaturation. Clearly, we still lack a unified model that is able to explain charge and discharge with a relevant set of parameters. The knowledge gap can be alleviated through insights from molecular simulations on kinetic rate parameters and nucleation phenomena. Out of all the charging models in the literature, Xiong et al.'s proposed model does the best job of capturing experimental charge features.

An alternative to the nucleation and radial growth theory is modeling precipitation phenomena as 2D vs 3D growth. This can be done through mesoscale modeling as the morphology of the precipitate affects pore space evolution in the cathode. An example of this is Mistry and Mukherjee's work[63] which assumes that there are different energetic interactions between the carbon substrate and the $Li_2S$ precipitate. Because of this, precipitate morphology can range from depositing at the carbon-pore interface, leading to more film-like structures (2D) or precipitates self-depositing at the precipitate-pore interface, leading to more finger-like structures (3D). Mistry and Mukherjee vary this morphology factor in a coarse-grain mesoscale model based on deposition energy involving surface affinity. They found that low-order morphologies lead to surface passivation, and high-order morphologies lead to pore blockage. These two events lead to cathode starvation -- no active reaction area -- and no further reaction can happen, causing the cell voltage to drop. Importantly, they showed the effect of microstructure evolution on electrochemical performance by relating mesoscale level variables (morphology factor, porosity, precipitation amount) as effective microstructural properties (tortuosity, conductivity, active area) that are used in a continuum-level electrochemical model. This meant that they could show the effect of morphology or porosity on cell operating condition trends such as capacity dependence on C-rate. This is a good example of multiscale modeling where modeled mesoscale interfacial phenomena is coupled with macroscopic cell-level performance. Note that pretty much all the existing meso/micro-scale models have not reported on mesh convergence/simulation efficiency and error. For a recent paper on the importance of mesh convergence, in particular in the presence of corner singularities, see Ref [64].

We can borrow insights from models at a smaller atomistic scale too. First-principles DFT calculations can show the strength of interaction between $Li_2S$ in solution and an adsorbed solid $Li_2S$ site.[65] Liu and Mukherjee created a coarse-grained lattice-based mesoscale model and used KMC to simulate $Li_2S$ adsorption, desorption, and diffusion on the surface. Since the nature of growth is related to fundamental interactions (pore/solvent structure etc.) that manifest as surface energetics, engineering of carbon structure and electrolyte to make it unfavorable for 2D film formation is an area of research with plenty of opportunity to be driven by a combination of atomistic, mesoscale, and continuum models.

## 2.4 Cathode Structure

The development and optimization of structured cathodes[66,67] has gained a lot of attention as a strategy to mitigate low sulfur utilization. Because both $S_8$ and $Li_2S$ solids are insulating, strategies to overcome poor electronic conduction are important in achieving high sulfur utilization. Cathode structure is also important for polysulfide entrapment to mitigate shuttling and to combat volume expansion during lithiation. However, most of the continuum modeling literature assume a macroscale composite carbon/sulfur cathode with effective properties, captured by the electronic conductivity, carbon fraction, and active surface area. More sophisticated microscale models are needed to understand the complex behavior and structure of the cathode. A study by Danner et al.[32] explored the implications of a nanostructured cathode with meso- and micro-porous carbon particles. Their work employed a simplified reaction scheme with a 1+1D model, where all the polysulfides remain trapped within the particles; their modeled cathode is similar to the porous electrode pseudo two-dimensional (P2D) model, where transport through the cathode and into the particle is considered. Comparing with experimental data, the model captured trends but missed the plateau transition and end of discharge regions, most likely due to the simplified 2-step reaction mechanism. Their work explored the effect of sulfur loading and salt concentration on the voltage and the simulated pore volume fraction. With lithium-ion as the sole charge carrier, the transport overpotential is significant to overcome the concentration gradient.

Work by Thangavel[68] describes a structured cathode with mesoporous carbon particles. The model includes transport on two different scales, within inter-particular pores (between carbon particles) and filling the mesopores of the carbon particle. The model also captures $Li_2S$ film passivation on the surface of the particles and within the mesopores. The work explored the sensitivity of microstructural properties on the discharge capacity. The predictions were able to reproduce rate capability seen experimentally.[69–71] When considering particle and mesopore sizes, the discharge capacities of larger particles were lower than small particles due to decreased surface area. The large particles showed faster $Li_2S$ film thickness growth, which led to earlier choking of the mesopores within the carbon particle and leaving unutilized sulfur. The $Li_2S$ film passivated the cathode, resulting in lower voltage. Meanwhile, the smaller particles had a higher discharge capacity overall; the clogging of the inter-particular pores signaled the end of discharge because the $Li_2S$ film did not reach the threshold thickness for choking the mesopores. The effect of C/S ratio was also explored by varying the sulfur loading; the highest sulfur loadings also exhibited the lowest capacities. The results from this work suggest that the microstructural properties can be tuned to delay the negative effects of $Li_2S(s)$ precipitation; the highest surface area for particles is recommended to alleviate clogging and film growth that leads to passivation of the cathode and poor sulfur utilization. Microscale models more accurately represent the competing phenomena of pore clogging and surface passivation and can guide design of the cathode. Furthermore, continuum models may need guidance from statistical-based models, such as KMC, or molecular dynamics to further understand evolution of the cathode dynamics and derive experimentally relevant parameters. The structure and material of the cathode is also highly engineered to suppress shuttle, and with guidance from DFT, adsorption and diffusion of polysulfides can be found,[72] and these values can be expressed as continuum level transport properties.

## 2.5 Shuttle, Degradation, and Lithium Anode Dynamics

Continuum modeling papers focused on lithium sulfur have traditionally modeled the anode as a flux boundary condition (lithium foil that supplies unlimited lithium ions), as a protected anode domain with Butler-Volmer kinetics describing the lithium redox reaction (although the anode overpotential is commonly taken to be negligible due to evidence that the cathode overpotential is dominant[34]), or as an active participant in the reduction of polysulfides that have shuttled over and in passivation reactions involving polysulfides at the anode surface. A few papers have modeled the effects of shuttle on the anode surface by approximating passivation with decreasing electrochemical active surface area, which changes the reactivity of the surface and affects the overpotential of lithium oxidation; this represents a first step towards understanding the impact of the lithium metal anode and consequent degradation and side reactions on cell operation. For high specific capacity batteries, we anticipate that future models will include both electrodes with experimentally-derived mechanisms, using a suitable electrolyte, to best represent a state-of-art cell. In all the models reviewed in this paper, SEI and dendrite formation on the lithium metal anode are not considered although they are important phenomena that remain hurdles for commercialization of lithium metal batteries. Models with detailed dendrite growth modes to describe lithium metal electrodeposition and stripping[73–75] can be coupled with 1D electrochemical models[76,77] to describe the lithium metal system. Understanding the behavior of the lithium metal anode in tandem with the complex polysulfide speciation behavior will give insights into cell design and operation to overcome current cycle life limitations. First-principles calculations and atomistic simulations can also shed light on electrolyte decomposition[78] and film formation[79] on the anode; the calculated molecular-level reaction and surface energies can be incorporated as side reaction rate constants and passivation rates in continuum models.

The main degradation mechanism for lithium sulfur batteries is the shuttle phenomena. During charge, lithium ions that are liberated from the cathode travel to the anode to be reduced to lithium metal to store the incoming charge. Since the polysulfides are also soluble in the electrolyte, they diffuse to the anode and are reduced as well, consuming the electrons meant to be stored there. The reduced polysulfides then travel back to the cathode and can be oxidized, only to repeat the process. Additionally, lower-order polysulfides may react with lithium at the anode to produce $Li_2S(s)$ that can further contribute to passivation of the anode and cell resistance.[11] Understanding the shuttle phenomena is key to development and operation of long-life high energy density lithium sulfur batteries. The modeling literature has approached the study of shuttle with both 0D and 1D models using macro- and microscale mechanisms.

The first 0D model by Mikhaylik and Akridge[31] included the shuttle degradation as consumption of the higher-order polysulfides at the anode during the higher plateau. The rate of shuttling is proportional to the concentration of higher-order polysulfides multiplied by the shuttle reaction rate (second term of Eq. (2.24)) and is included in a mass conservation differential equation:

$$\frac{d[S_H]}{dt} = \frac{I}{q_H} - k_s[S_H] \tag{2.24}$$

where $[S_H]$ is concentration of higher-order polysulfides normalized to specific volume or surface, $I$ is the normalized charge/discharge current, $q_H$ is the sulfur specific capacity for the higher voltage plateau, and $k_s$ is the shuttle rate constant. Shuttling only occurs during charging and is assumed to start during the second cycle. The model also included self-heating from the shuttle current and an Arrhenius expression to describe the temperature dependence of the shuttle rate. Their model also focused on overcharge protection due to infinite charging. This happens when the shuttle current is equal to or greater than the applied current, and the voltage curve levels off into a plateau ad infinitum with no increase in the stored charge.

Another 0D model with the shuttle mechanism is the study by Marinescu et al.[80] In their work, a fraction of the shuttled polysulfides becomes permanently inactive, described by a dimensionless loss rate, $f_s$. The rate of shuttle or loss sulfur, $S_l$, is proportional to the mass of dissolved sulfur, $S_8^0$, the shuttle rate constant, $k_s$, and the sulfur that has already been shuttled, $S_s$, which means that the shuttle rate increases with aging.

$$\frac{dS_l}{dt} = \frac{f_s}{m_s} S_s k_s S_8^0 \tag{2.25}$$

where $m_s$ is the mass of active sulfur per cell. The authors relate the increased rate of shuttle to increased surface area available for precipitation as more solids precipitate on the anode although in a lumped model the sulfur loss is area nonspecific. The model is used to explore experimentally seen voltage drift with cycling, and the authors attributed it to SOC drift. Therefore, traditional SOC estimation techniques like coulomb counting or voltage reading are not adequate for cycling of LiS batteries. The model also classified capacity loss as either reversible or irreversible, depending on the conditions. Predictions from the model indicated that reversible capacity loss is due to the bottleneck of slow dissolution of solids from high charging rates while irreversible capacity is due to shuttle at low charging rates.

The description of the shuttle phenomena with a 0D model inherently ignores the transport of the polysulfides from the cathode to the anode. Several 1D models have incorporated the shuttle as a microscale mechanism to understand the role that transport plays in degradation. Hofmann et al.[81] explored the polysulfide shuttle mechanism with the simplified 2-step reduction scheme. Their mechanism included the reduction of $S_8$ to $S_4^{2-}$ and precipitation of $Li_2S$ at the anode; furthermore, the $Li_2S$ at the anode is classified as either active or passivating the surface. The passivating $Li_2S$ decreases the anode reactive surface through a heuristic expression,

$$f\left(\varepsilon_S\right) = \left(\frac{\varepsilon_{pore} - \varepsilon_{Li_2S}}{\varepsilon_{pore}}\right)^{3.5} \tag{2.26}$$

where $f\left(\varepsilon_S\right)$ approximates the active surface on the anode, $\varepsilon_{pore}$ is the volume fraction of usable anode, and $\varepsilon_{Li_2S}$ is the volume fraction of passivating $Li_2S$ on the anode surface. This heuristic approximates the degradation of the anode surface through loss of electrochemical active area. As the cell degrades, resulting in both loss of active material and less reactive surface area on the anode, the anode overpotential increases, decreasing the voltage plateaus. The model predicts higher capacity loss per cycle initially, which levels off; this is in agreement with experimental studies that show high capacity loss during the initial cycles.[82]

Another study by Yoo et al.[55] uses the 5-step reduction scheme with the shuttle mechanism at the anode. During charge, the polysulfides are able to travel to the anode, where they are reduced at a rate proportional to their concentration and their individual shuttle constant; this represents lost charge due to shuttle.

$$\left.\frac{\partial C_i}{\partial t}\right|_{x=L_1+L_2} = -k_{ps,i}C_i + k_{ps,i-1}C_{i-1} \tag{2.27}$$

where $k_{ps}$ is the shuttle rate constant. The first term is the sink while the second term is the source from a higher-order sulfur species denoted with $i$-$1$. The model does not include precipitation of solids on the anode surface. This work explored cycling performance of cells with various diffusivities and reduction rates; predictably, the degradation worsened for high diffusivities of polysulfides and increased reduction rates. Kamyab et al.[83] followed a similar approach to including shuttle on the anode, where the rate of precipitation is proportional to the shuttle rate and concentration.

Mistry and Mukherjee[30] extended their previous work using concentrated solution theory to study the effects of speciation and lean electrolyte conditions on polysulfide shuttle and degradation. The shuttle is modeled as an interfacial flux due to the redox reaction at the anode/separator interface, shown in Table 1. (When modeling without shuttle, flux at the interface is zero for all species except lithium.) The capacity loss is characterized as either reversible or irreversible, due to reduction of higher-order polysulfides at the anode or precipitation of $Li_2S$ on the anode surface, respectively. With increasing C-rate, the overall capacity loss due to shuttle decreases due to decreased operation time. However, the limitations from the cathode and electrolyte have the largest contribution at high C-rates, indicating an optimum intermediate rate to balance degradation phenomena. This is in contrast to the macroscale/0D modeling of shuttle, where capacity loss increases with rate. Taking a closer look at electrode conditions, E/S ratio and porosity show a nonlinear relationship with limiting phenomena. At lower E/S ratios and porosity, the transport limitations dominate while increasing these parameters leads to capacity loss from polysulfide shuttle. Incorporating a detailed model for lithium metal morphology will allow a closer look at the relationship between shuttle, speciation, and high energy cell conditions.

The study by Danner et al.[32] explored degradation with nanostructured cathodes where all of the polysulfides except for $S^{2-}$ are assumed to be trapped within the carbon particles. After $S^{2-}$ diffuses out of the particle, the model assumes that it is now electrochemically inactive representing the maximum amount of irreversible loss of sulfur; realistically, the diffused $S^{2-}$ could still participate in reactions as long as it is within the cathode matrix. The capacity loss is linear initially and then increases steeply with more cycles. This work also explored the effect of $Li_2S$ solubility product and salt concentration on the cycling capacity loss. With higher Ksp for $Li_2S$, more of the $S^{2-}$ is able to leave the particle resulting in increased loss. The cycling study shows that increasing the salt concentration increases capacity retention; however, high salt concentrations will have a negative effect on both ionic conductivity and the energy density of a cell. This work highlights the importance of modeling to optimize multiple variables simultaneously for practical high energy cells.

Polysulfide shuttle can also occur in the absence of current and can lead to self-discharge. This is due to the lithium anode being strongly reducing. To understand the self-discharge behavior due to shuttling, Al-Mahmoud et al.[84] fabricated LiS cells with varying numbers of separators between the electrodes, and measured the voltage signal measured from a fully charged state. The 1D model considers transport through the separator and redox reactions at the electrodes as boundary conditions; the only species in the model are $S_8$ and $S_8^{2-}$ that continuously oxidize or reduce at the electrodes. The net current is zero, and the current that oxidizes $S_8^{2-}$ is equal to the change in potential multiplied by the capacitance of the carbon. Mahmoud et al. found that including the capacitive behavior of the carbon within the sulfur cathode was necessary to reproduce the open circuit potential of a battery with 5 separators. Without including the capacitance, the voltage sharply drops, leveling off within 30 minutes, while the model with capacitance predicts a gentler slope to the final voltage at around 2 hours, matching the experimental curve. Their simple model can predict the evolution of the open circuit potential of batteries well with 2 to 5 separators. The model was also able to capture the difference between the self-discharge behavior of a cell with no initial dissolved sulfur and a cell with saturated electrolyte by altering the initial conditions of sulfur in the electrolyte.

Another approach of measuring and modeling the shuttle current during self-discharge was demonstrated by Moy et al..[85] They measured the shuttle current by holding the electrode potential constant and waiting till the current reaches a steady state value. The steady state current is equal to the diffusional flux of polysulfides between the electrodes. They found that the shuttle current decreases to zero with depth of discharge since insoluble products are present at the end of discharge. They also found that with the addition of $LiNO_3$, the shuttle current is reduced to almost zero due to $LiNO_3$ forming a passivation layer on the anode. With a simple model based on algebraic equations of flux balances, and the assumption that the anode is strongly reducing such that all higher order polysulfides are reduced to $S_4^{2-}$ at the anode, Moy et al. were able to model the shuttle current as a function of SOC that match experimental values well. They also assumed linear concentration gradients from diffusive fluxes and that the conversion of $S_4^{2-}$ to $Li_2S_2$ and $Li_2S$ solids at the anode is 100-3000 times slower than the interconversion of polysulfides and hence do not model this process in their calculations of shuttle current. However, this phenomenon is observed in their experiments in the form of the slow decay of shuttle current at long timescales. Moy et al. used an average value of this decay rate over a discharge cycle and calculated irreversible capacity fade as a function of cycle life. Being able to quantify the shuttling rate with SOC and shuttle decay is important to help predict the effectiveness of modifications without excessive cycling.

Research by Wen et. al.[86] modeled self-discharge in a 1D LiS sandwich cell to explore reversible versus irreversible capacity loss. The self-discharge behavior of coin cells at different cycles was explored, and the cells underwent ex-situ X-ray diffraction experiments to analyze precipitation. The relationship among self-discharge, polysulfide shuttle, and the resting voltage was proven to be important and rate-dependent. Self-discharge was more rapid at higher voltages due to higher-order polysulfide reduction at the anode; the capacity loss was highest at high SOCs. Resting during the lower voltage plateau leads to formation of precipitate and minimal capacity loss. The authors recommend resting at 2.10 V to minimize capacity loss, and the model results indicate that the focus should be on anode protection to mitigate degradation.

Multiple phenomena, such as intermediate polysulfide transport and lithium metal passivation, play an important and complex role in both calendar and cycle life, and continuum modeling has furthered our understanding of degradation through incorporating these mechanisms. Moving forward, models should include more detailed dynamics of the lithium metal surface evolution for a full cell view of these issues.

## 2.6 Transport Properties, Limitations, and Solution Phase Dynamics at Low E/S Ratios for a Cell

It is important for a model to capture transport limitations in a cell to mimic conditions such as a battery with low E/S ratio undergoing fast charging. In the 1D literature, the resistance within the electrolyte is not adequately captured.[54] Experimentally, ohmic resistance as a function of state-of-charge (SOC) can be measured using EIS (the high frequency real-value limit). In the case where electronic conductivity is high, electrolyte resistance can be assumed to be the bulk of ohmic resistance. To adequately capture electrolyte effects, both micro and macroscale liquid phase dynamics have been incorporated.

Zhang et al.[54] calculated the variation of the electrolyte resistance with SOC using the Kumaresan model and found that this variation does not match experimentally measured electrolyte resistance. To accurately represent the electrolyte transport in a macroscale manner, Zhang et al. expressed electrolyte conductivity as a linear function of $Li^+$ concentration, which represents the sum of anion concentrations since measurement of transport properties of each individual polysulfide anion is challenging. With this expression of ionic conductivity,

$$\kappa = \epsilon^{1.5}(\kappa_0 - b\,|C_{Li^+} - C_{Li^+,0}|) \tag{2.28}$$

where $\epsilon$ is porosity, $\kappa_0$ and $b$ are fitted parameters, and $C_{Li^+}$ is the concentration of lithium-ion with $C_{Li^+,0}$ being the initial concentration, they introduced two new parameters and were able to reproduce both the trend and magnitude of the electrolyte resistance during discharge from experimental data. This result is shown in Figure 2.4. We note that they used a 0D lumped model without mass transport (reactions modeled off Kumaresan et al.) and incorporated the electrolyte resistance as an ohmic potential drop contribution in the overall cell voltage. Zhang et al. found that the voltage dip during the transition between the two plateaus occurs not only due to supersaturation of $S^{2-}$ but also due to a peak in electrolyte resistance, consistent with modeling results from the concentrated solution model by Mistry et al (reviewed later in this section).[87] Other papers have also used expressions of ionic conductivity as a function of lithium ion concentration and these are empirical expressions found using fits to experimental conductivity data.[58,59] These papers represent a macroscale view of modeling effective transport properties.

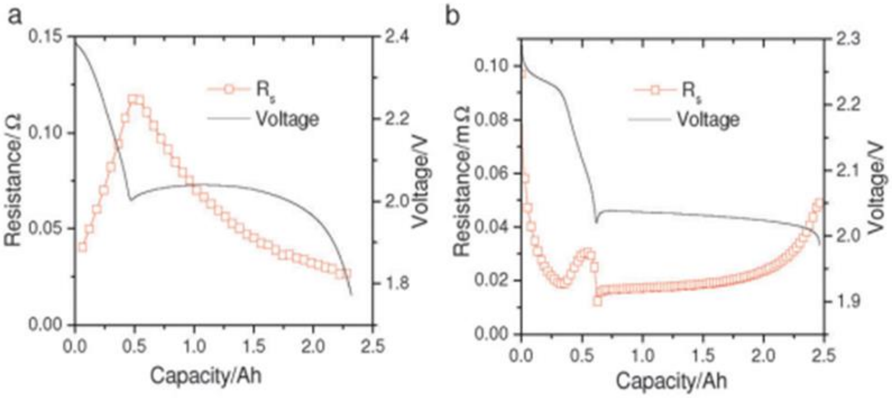

***Figure 2.4 Discrepancy between experimental and modeled electrolyte resistance as a function of depth of discharge. (a) Electrolyte resistance of a commercial LiS pouch cell measured using EIS. (b) Simulated electrolyte resistance from the Ref [29] model. Reproduced from Ref [54] with permission from the PCCP Owner Societies.***

For a high energy density cell, the E/S mass ratio should be less than 5 uL/mg,[26] hence a lean and concentrated electrolyte would mean solubility and transport limits sulfur utilization. Also in line with macroscale modeling, Zhang et al.[35] reduced the diffusion coefficients of all species by two orders of magnitudes to demonstrate a transport-limited cell. They use a 1D Kumaresan-type model with the only precipitate being $Li_2S$. They are able to match experimental discharge curves qualitatively, with the ability to capture the reduction of the low plateau capacity at higher currents which has not been shown previously. However, they were unable to capture curvature of the first plateau and some features at higher rates. To test their theory of the cell being transport-limited, they carried out an experiment and corresponding simulation where the cell is discharged, relaxed, and allowed to be discharged further. Since some capacity is recovered after relaxation, Zhang et al. concluded that for a high energy density LiS cell, the discharge capacity reduction due to higher current can be attributed to transport limitations, and less so due to surface passivation or pore blockage from precipitates. If transport is indeed a limiting factor for LiS cells, models might need to move away from the macroscale dilute solution theory towards a concentrated solution theory to better capture diffusive effects.

For a microscale approach, using recent nucleation and growth models that are able to predict reduction in capacity of the lower plateau with increasing rate, Andrei et al.[59] repeated an experiment by another Zhang et al.[56] paper. Andrei et al. used a 0.2C-1C-0.2C variable discharge rate and compared the specific capacity of certain portions to a standard 1C discharge. Their results did not match Zhang et al.'s conclusion that rate-dependent discharge capacity is due to slow transport (here, Andrei et al. are unable to recover all capacity at a slower rate), but rather found that different dynamics of nuclei growth occurs at different C-rates. There is a disagreement between the nucleation papers[58,59] and the Zhang et al.[35,56] papers about whether capacity reduction at high discharge rates is due to rate-dependent surface coverage or rate-dependent transport limitations. Furthermore, Zhang et al. used EIS to show that charge transfer resistance, commonly associated with surface coverage, is SOC-dependent and rate-independent. The discrepancy in experimental results is likely due to Andrei et al. using coin cells with low loading while Zhang et al. used OXIS pouch cells with presumably low E/S ratio. There needs to be a clear understanding that a single model will not be able to capture different limiting phenomena due to differently engineered cells. Comparing their simulations to an experimental cell with lean electrolyte, Zhang et al.[56] used a simple 0D model with a modified transport-limited Butler-Volmer kinetics expression (includes limiting current):

$$\frac{I_j}{a_v V i_j} = \left(1 - \frac{I_j}{I^{lim}}\right)\exp\left(\frac{-F\eta_j}{2RT}\right) - \left(1 + \frac{I_j}{I^{lim}}\right)\exp\left(\frac{F\eta_j}{2RT}\right) \tag{2.29}$$

where $I_j$ is the current of reaction $j$, $i_j$ is the exchange current density, $a_v$ is the specific surface area of the cathode, $V$ is cell volume, $I^{lim}$ is the limiting current due to mass transfer. Not only were they able to match their variable discharge rate experiment very well, but they are also the first model to demonstrate the kink at the start of charging. Review of these two papers demonstrate the complicated nature of lithium sulfur systems and the existence of competing phenomena. We want to highlight that the cell conditions dictate the limitations and ultimately there should be a model that can accurately predict both precipitation phenomena and transport limitations in line with experimental work.

An improvement to prevent shuttling is to use gel polymer or gelled liquid electrolytes to trap polysulfides by limiting their transport and solubility. Gel electrolytes are also less flammable and help suppress dendrites at the lithium anode. Shebert et al.[88] effectively combined experiment and simulation to explore mass transport limitations introduced by gel electrolytes. Through experimental work, they showed that the specific capacity of a liquid electrolyte system is still better than the gel electrolyte systems, though the cycling performances of the gel electrolyte systems are better. They also showed that for an LiS cell with gel electrolyte, the first discharge voltage plateau is extended while the second plateau is shortened, relative to a conventional electrolyte. The former effect suggests that the gel electrolyte system promotes entrapment of polysulfides and improved sulfur utilization. This latter effect implies slow conversion of soluble to insoluble polysulfides and could be due to slow transport of intermediate polysulfides or passivation of reaction sites. To investigate this, Shebert et al. conducted an experiment where they discharged a cell to 1.8V, let it rest for an hour, and discharged it further. They showed ability to recover more capacity in the second discharge, which indicates that this effect could not be due to all polysulfides being reduced or all sites being passivated, but rather due to mass transport limitations. The gel electrolyte system had greater capacity recovery than the liquid electrolyte system. Shebert et al. also varied the pause time and measured capacity recovery as a function of C-rate. Then, they were able to match their experimental results qualitatively using a continuum model with a fast and slow diffusion rate of $S_4^{2-}$ (slower diffusion represents the gel system). Similar to Zhang et al.[56] , they used a mass-transport limited Butler-Volmer expression to model kinetics of the electrochemical reactions; however, this is a 1D instead of a 0D model. In this model, the limiting reaction rate has two extra fitting parameters with the assumption that the maximum mass transport rate to reaction sites decrease as solid deposits clog the pores in the cathode and the bulk concentrations of reactants decrease. For the discharge-pause-discharge experiment, during the pause, $S_4^{2-}$ has time to diffuse back to the cathode to get additional capacity. Mass transport limitations are only seen at the end of discharge when there is low concentration of $S_4^{2-}$ and a lot of surface passivation from $Li_2S$ deposits. Since the discharge capacity of LiS cells with gel electrolytes is still smaller compared to conventional electrolytes, this investigation shows that the capacity can be improved by limiting the polysulfide flux out of the cathode or speeding their return to the cathode.

Transport properties can also be modeled in a microscale manner to consider the effects of complex solvent interactions. Mistry et al.[87] developed a 1D model based on concentrated solution theory that describes the complex transport behavior during discharge. Concentrated solution theory, derived from nonequilibrium thermodynamics, captures interactions among the polysulfides by accounting for the self- and inter-species transport at high concentrations. The fluxes are defined by the following:

$$N_i = -D_{ii}\nabla C_i - \sum_{j\neq i} D_{ij}\nabla C_j + t_i \frac{I}{z_i F} + C_i V_0 \tag{2.30}$$

where $N_i$ is the flux for species *i*. The first term is the self-gradient flux where $D_{ii}$ is the diffusion and $C_i$ is the concentration of species *i*. The second term is the contribution of dissimilar species to the diffusion where $D_{ij}$ is the cross-diffusivity and $C_j$ is the concentration of species *j*. The third term describes the migrational contribution to flux, where $t_i$ is the transference number and $z_i$ is the charge number. The final term is due to advection of the bulk flow of the species due to solvent motion where $V_0$ is the velocity of the solvent. Within this model, the limitations due to surface passivation from insulating precipitates, pore blockage, and electrolyte resistances are calculated and compared. The work uses a microstructurally resolved model to describe the changing morphology during discharge. They attributed part of the voltage recovery before the second plateau to ionic conduction of medium chain polysulfides, in agreement with Zhang et al.[54] The dominant species that contribute the most to high concentrations and consequent transport limitations are $Li^+$ ions due to accumulation until $Li_2S$ precipitation, and medium-chain polysulfides ($S_4^{2-}$) due to solubility and higher production rate compared to the higher-order polysulfides. The model is able to capture competing dynamics, like the rate dependence of passivation, pore blockage, and ionic conduction.

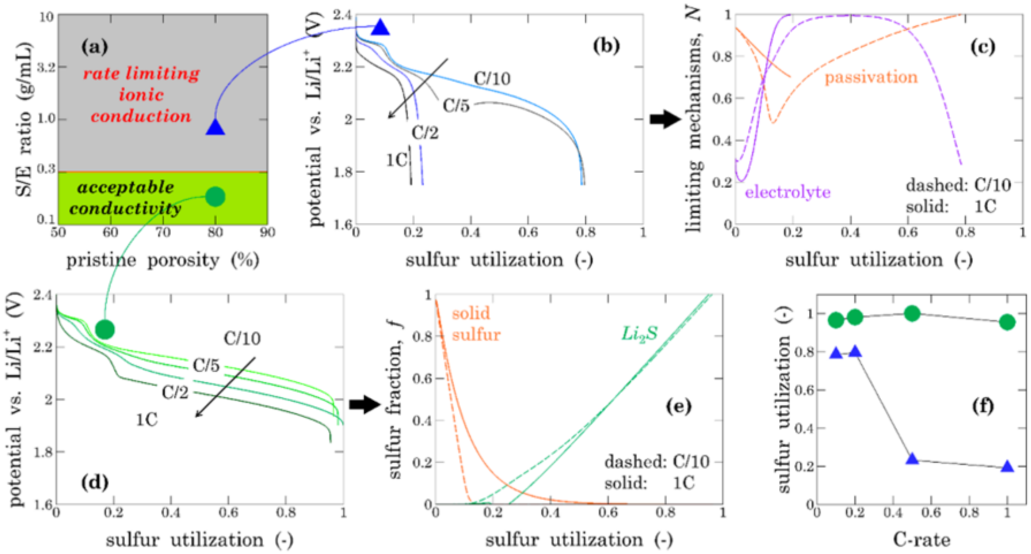

***Figure 2.5 Electrolyte transport regimes, (a) porosity versus S/E (sulfur to electrolyte) ratio with green showing acceptable conductivity and higher values in the rate limiting ionic conduction, (b) potential curves within the rate limiting regime, (c) plot showing the limiting mechanism with sulfur utilization, (d) potential curves with acceptable conductivity, (d) solid species with sulfur utilization, (f) shows the sulfur utilization with C-rate for both regimes. Reprinted with permission from Ref [87]. Copyright 2018 American Chemical Society.***

Their work classifies E/S ratio in two regimes, rate-limiting and acceptable, shown in Figure 2.5. When considering the rate-limiting ionic conduction with low E/S ratios (or high S/E ratios), the sulfur utilization is highly C-rate dependent (Figure 2.5f). At low rates, the ionic conductivity increases with an increased rate due to overlap in the speciation; consequently, there is a lower concentration of medium-chain polysulfides, resulting in less transport resistances. This is balanced with increased potential drop due to transport limitations of higher rates. For the increase from C/10 to C/5, shown in Figure 2.5b, there is an increase in sulfur utilization. However, at higher rates, the increased ionic conductivity is not enough to overcome the resistance due to transport at higher rates (Figure 2.5c). For acceptable conductivity behavior (Figure 2.5d-e), the sulfur utilization is fairly constant with C-rate, and there is a decrease in the voltage for increasing rate. Within a practical high energy density cell, the conditions are expected to cause high concentrations and viscous electrolyte conditions, highlighting the importance of studying electrolyte transport limitations through this lens.

## 2.7 Considerations for Scale-up and High Energy Density Cells

Testing and development of new battery materials first occur on the coin cell scale. Many times, the results from coin cell experiments fail to scale up for larger-format cells.[89] Coin cells often have excess electrolyte resulting in flooded cell conditions. In a flooded cell, the excess electrolyte masks limitations and is not practical for high energy cells. In particular, the negative effects of electrolyte consumption are delayed, and issues surrounding cell wetting or transport limitations due to viscous solutions and high concentrations of polysulfides are masked by the excess electrolyte. Flooded cells mean higher cost and lower energy density. There has been a concerted effort to set standards for cell conditions to test high energy format cell conditions.[90] The E/S ratio is an important metric that describes the volume of electrolyte to the mass of sulfur. It has been calculated that high energy cells should have an E/S ratio of less than 5 uL/mg.[26]

Modeling tools can help explore the effect of E/S ratio. Previous work by our group[47] explained that the original model formulation from Kumaresan[29] is not able to replicate appropriate E/S ratios for high energy density cells. For the 1D lithium sulfur model, the sulfur/carbon/porosity are all constrained, and the E/S ratio is simply a calculation based on the ratio of the sulfur volume fraction to porosity within the cell. The porosity is constrained by sulfur mass conservation while the electrolyte volume is not explicitly conserved. However, within a real cell, electrolyte amounts are not completely constrained by the porosity, sulfur loading, and filler fractions since overfilling or underfilling can occur. The E/S ratio for the 1D model work greatly underestimates the E/S ratio. Another aspect that is not captured currently within models is the wetting of the cathode. The modeling literature assumes perfect wetting and effective cathode properties. However, for E/S ratios for a practical high energy cell, the problem of cathode wetting is very relevant as high carbon content reduces wettability due to solvophobicity of carbon.[26] Perhaps development of microscale models that study the interactions among sulfur, carbon infrastructure, and electrolyte would be insightful to optimizing E/S ratio and other important metrics for high energy cells. Modeling groups will facilitate better communication with experimentalists by reporting and calculating important metrics like E/S and C/S ratios in their work. Closer collaboration with molecular simulation groups is recommended to help model physical interactions and provide relevant parameters.

A series of papers by the Eroglu group[34,91–94] have investigated both E/S and C/S ratios in their macroscale modeling work. Their work coupled cell-level predictions of voltage, overpotentials, and area-specific-impedance with systems-level predictions of energy densities from the publicly available software called Battery Performance and Cost (BatPaC). The 1D model is used to predict the effect of E/S ratio on voltage and capacity trends. Coupling the results with the calculations from BatPaC, the cell-level specific energy and energy densities can be calculated for various sulfur loadings and maximum thicknesses. This work extends optimizing for capacity to systems-level parameters that are relevant for commercialization. For example, increasing electrolyte amount improves both voltage and capacity, but the excess material comes at a specific energy penalty. With the electrochemical predictions feeding into the cell-level model, the balance between improved performance and energy density can be understood. The model predicts the best performance with an E/S ratio of 20 uL/mg, but E/S = 13 uL/mg provides an optimum for specific energy and energy density. This result is surprising as the E/S ratio is higher than what is typically considered desirable for state-of-art cells. For example, with high E/S ratios of over 11 mL/g, the pouch cell specific energy will be below 140 Wh/kg, less than advanced Li-ion batteries.[89,95] This highlights the need to push for consistent and relevant metrics to relate models to high performing LiS cells.

## 2.8 Electroanalytical Methods for Whole Cells

Electroanalytical techniques can be useful to provide information on mechanisms and physical processes beyond what we can learn from standard charge/discharge voltage curves. For example, we looked at work in the Cathode reaction scheme section where CV was modeled as a means to propose reaction pathways.[41,43] There might be other ways to disaggregate physical processes from each other. For example GITT is commonly used to find diffusion parameters in lithium-ion systems but has only been used experimentally in lithium sulfur systems to look at internal resistance[8] and thermodynamic equilibrium. [9–11] There has been work done to apply diffusive concepts from GITT theory to a lithium sulfur cell using a simplified example system[7] but no lithium sulfur continuum model has been applied to understand thermodynamics separately from transport and kinetic processes. However, PITT has been simulated by Danner & Latz[52] (more detail in Precipitation section) to explore nucleation overpotential.

Another useful electroanalytical measurement is EIS, which can separate processes occurring on different time scales. For lithium sulfur cells, EIS measurements are commonly fitted to equivalent circuit models and circuit elements that represent physical processes, such as charge transfer resistance, are quantitatively compared. For example, Lee et al.[96] compared the magnitude of the charge transfer resistance of a cell with and without a coated separator to suppress shuttling. There have been detailed studies[97–99] using equivalent circuits to fit to EIS measurements at different SOCs, states-of-health (SOHs), and temperatures, but it remains challenging to elucidate the origins of each feature (e.g. multiple semi-circles). Physics-based models can help improve diagnostics by attributing specific features to physical processes compared to degenerate equivalent circuit models. Fronczek and Bessler[100] are the only authors that have demonstrated the use of full physics-based continuum models to simulate impedance of LiS cells. They use a similar set of governing equations and reaction schemes to Kumaresan[29] except that the kinetic reactions are written as elementary steps following Arrhenius law instead of Butler-Volmer expressions.

$$\dot{s}_i = v_i \left( k_{fwd} \prod_j a_j^{\nu'_j} - k_{rev} \prod_j a_j^{\nu'_j} \right) \tag{2.31}$$

$$k = k_0 \exp\left( -\frac{E^{act}}{RT} \right) \exp\left( -\frac{\alpha z F}{RT} \Delta\phi \right) \tag{2.32}$$

where $\dot{s}_i$ is the rate of reaction $i$, $v$ are stoichiometric coefficients, $k$ are forward and reverse rate constants, $a_j$ are activities of species $j$, $E^{act}$ is activation energy, $z$ is number of electrons transferred, and $\Delta\phi$ is the potential difference between solid and electrolyte. They also included an electrochemical double layer which is important for fast timescales. Fronczek and Bessler simulated the impedance using a voltage step of 1mV in 0.1 microsecond, and took the fast Fourier transform of the current relaxation over 1000s. They showed the ability to simulate EIS spectra but with very limited discussion on the results. Their simulated impedance also decreased in magnitude with SOC which does not agree with the experimental literature listed above. This disconnect might be due to the parameters used in their model, the concentration dependent ionic conductivity highlighted by Zhang et al,[54] or other missing mechanisms in the model.

The field can greatly benefit from using a variety of electroanalytical techniques to validate a model to uncover underlying physics that dominate behavior and cell performance. There is also opportunity for the above continuum models to be applied to electroanalytical methods and explore how they are analyzed as functions of state of the cell such as SOCs.

## 2.9 Parameter Identifiability and Estimation of Cells

A natural next step after model development is parameter identification through estimation. If the purpose of a model is to eventually be used in a BMS for control purposes such as optimal charging, then online state estimation is important for identifying parameters that define the most current state of the battery. Parameter identification is a daunting optimization task for a highly nonlinear system. Some strategies to approach this would be conducting a sensitivity analysis to understand the physical range and impact of varying parameters, careful model reduction to improve computation efficiency (as fitting a model requires running it iteratively), and building frameworks for online optimization.

Ghaznavi and Chen wrote a series of three papers covering sensitivity analysis of the Kumaresan model with respect to different sets of parameters. Their objective was to explore the possible range of physical parameters and mathematical limits of the model. In their first paper,[101] they studied the effect of discharge rate and electronic conductivity on cell performance. They found that at high rates and low conductivity, large amounts of $Li_2S$ precipitate close to the cathode/current collector interface and fill up the porous matrix, thus reducing active surface area. This type of study might be useful when looking at additives or binders to improve conductivity. In their second paper,[50] for the case where intermediate polysulfides precipitate and block pores, they found an upper limit for the optimal sulfur content for greater capacity (only cells with less than 20% sulfur content by cathode volume can be fully discharged). They also varied the precipitation rates for each reaction and found a “critical interval” for each rate constant, where a small variation in rate constant results in a large change in voltage response and capacity. These findings are only for this set of parameters and for the case where we are considering intermediate polysulfides precipitating, which is not typically considered since they are highly soluble. Although in the context of low E/S ratios, it is possible the polysulfide species may precipitate out due to high concentrations. A thorough study with physical parameters (such as solubility) that are relevant for a state-of-art cell, and precipitation mechanisms that can be cross-referenced with experimentally observed species might be more useful to build representative models.

In their third paper, Ghaznavi and Chen[51] first looked at the effect of exchange current densities. By changing the exchange current densities relative to each other, they can determine the dominant reaction and observe shifts in the voltage plateau. This might be useful for elucidating the rate-limiting steps to engineer specific improvements for kinetics. The diffusion coefficients were also varied where a decrease in an order of magnitude showed no effect. They explored optimal cathode thickness and also the need to increase the solubility product by a factor of $10^8$ for the model to charge. This set of papers was useful to understand the impact of each physical parameter and demonstrated the ability of models to predict and optimize cell performance in relation to an engineered change. However, this theoretical study based on assumed parameters needs to be taken a step further to align with experimentally observed and measured parameters, trends, and speciation.

Work by our group[102] focused on reducing the computational demand of the standard 1D model by considering each region as a tank connected in series. The Tank-in-Series model has connected mass flow between the regions through continuity of flux; a new fitting parameter describes the fraction of each region where gradients are assumed to be, usually ½ or ⅓. The reduced model is able to reproduce the trends shown in the 1D model under even transport-limited conditions. A parameter study of rates (up to 1C), diffusion coefficients (as low as to $1 \times 10^{-12}$ $m^2/s$), and cathode thicknesses explored the suitability of the model predictions under various conditions. A map of the errors was calculated and shown to be under 25mV for all conditions with most errors falling below 15mV. The Tank model was calculated to run in under 1 second, representing a speed increase of over 150x compared to the 1D model; the model also implements a logarithmic scaling of the differential variables, resulting in a more robust model that can simulate to lower voltages at the end of discharge where the 1D model sometimes experiences a singularity. This work bridges the gap between computationally efficient 0D models and 1D models with transport effects. With the improved computational efficiency, the Tanks-in-Series model is promising for parameter estimation, optimization, and battery management systems.

Two papers by Xu et al. demonstrate parameter identification for 0D LiS models. The first paper[103] focuses on model selection and a parameter sensitivity study to determine the important parameters to be identified. They started by carrying out a systematic comparison of four different 0D models to the same experimental dataset. All four 0D models are based on Ref. [33] and Ref. [54] where there is no diffusion or migration terms. The four 0D models differ based on the number of electrochemical reduction reactions, with a range of two reduction reactions to the full set of five reactions to describe the two plateaus. They assumed that all $S_8$ is dissolved at the start of discharge. Xu et al. also carried out a sensitivity analysis by changing one parameter at a time for the full model. Upon comparing the derivative of voltage with respect to the varied parameter, they found that the most significant parameters are the standard potentials, morphology factor (power of the relative porosity), porosity change rate constant, and mass of initial sulfur. The porosity change rate constant is treated as a fitting parameter although it should be a constant relating to density of the precipitated solids. Then, they chose to identify these significant parameters by fitting all four models to experimental data. They concluded that the model with 4 electrochemical reactions ($S_4^{2-}$ is directly reduced to $S^{2-}$) performs the best in terms of computation time and capturing features well. The full model with 5 reactions does not capture the nucleation dip well. Since it is sufficient to capture features well with a less complicated scheme and with less parameters, Xu et al. used this model with 4 reactions in their following paper about online state estimation. We point out that this approach towards sensitivity analysis by varying one parameter at a time is not useful when the base parameters (initial guesses) change as this is a nonlinear model. Bayesian estimation maybe be more useful for parameter estimation.[104]

In this second paper,[105] the focus is on online estimation of the mass of different sulfur species during a discharge. They reformulated the model by converting the system of differential algebraic equations to ordinary differential equations by analytically solving the current equation and writing an analytical expression for voltage. They found that the model is locally observable. A model is locally observable if the estimated initial states are close to the true value, it is possible to construct an estimator/observer that converges to the true value. They also found that the lowest estimation errors are at the voltage dip while the greatest errors occur at the flat low plateau region. This means that the estimation of parameters is more challenging in the flat region as the voltage is less sensitive to parameters. The largest standard deviation of error is linked to the mass of precipitated $Li_2S$ since the output voltage is not sensitive to mass. Xu et al. proposed the use of mass conservation to eliminate two of the seven state variables, mass of solid $Li_2S$ and porosity, and thus improving observability. This can be achieved by assuming that the total sulfur is known and enforcing a mass balance constraint. They used an unscented Kalman filter to perform state estimation during a constant discharge. Based on their results, they recommend that estimation is carried out in two steps: first at the high plateau region using the full model and estimating the total active sulfur mass, then using the reduced model to estimate the low plateau. Xu et al. laid out a framework and demonstrated ability to perform online state estimation, showing a viable path for incorporating physics-based models onto BMS for control applications. It is important to note that since this is a 0D model, it will have limited performance at higher rates or if the system is transport-limited.

## 2.10 Conclusions

We reviewed and outlined the advancement of macroscale and microscale continuum modeling literature for lithium sulfur batteries. Simplified reaction schemes typically employed in lumped models are useful for minimization of parameters while enhancing computational efficiency. Microscale modeling efforts have focused on incorporating insights from experimental methods, such as high-performance liquid chromatography and cyclic voltammetry, to further understand the speciation and the impact of electrolyte engineering. A critical area of research is the reversibility of models. Most models are not able to reproduce all the charging features, and there is still debate about whether the discrepancy is due to missing mechanisms of precipitation phenomena or inaccuracies of the reaction scheme. The presence of multiple phases and mixed speciation within a lithium sulfur battery means changing conditions throughout a single cycle. Significant progress has been made to model the microscale precipitation within the cathode, and particle-level nucleation and growth mechanisms have been able to capture the rate-dependent dynamics. Experimental efforts have focused on micro and nano-structured cathodes to overcome issues like conductivity, pore clogging, and active material loss due to the high solubility of polysulfides while most models only consider the cathode as a composite material. A microscale model for the cathode has been implemented and considers a mesoporous structure that captures effects of particle size; future modeling work should adopt similarly resolved cathode models. The polysulfide shuttle has been modeled to understand degradation. While lumped macroscale models include shuttling proportional to the current, macroscale modeling of shuttle predicts a more complicated relationship between operating conditions and other limiting phenomena, like transport limitations within the cathode. Lithium metal morphology and reactivity have been approximated by a passivation of the electrochemical active surface with deposition of $Li_2S$. As cells trend toward lean electrolyte conditions for high energy density, solution phase dynamics become more important due to increased transport limitations. Microscale modeling is key to accurate predictions of speciation and practical operating range; models have focused on areas such as improving experimental agreement for electrolyte resistance and utilizing concentrated solution theory. For scale up and meeting high energy density targets, work has focused on parameters like electrolyte to sulfur and carbon to sulfur ratios for insight into performance under relevant conditions. Electroanalytical methods like EIS and GITT can greatly inform mechanisms and phenomena occurring at different time scales, and the field would benefit from further model development and collaboration in this area. Another important aspect of modeling is alignment of model parameters and predictions to experimental data. Efforts in this area include parameter sensitivities, development of computationally efficient models, and parameter estimation. This research area will become more important as the focus moves from active development (electrolyte engineering, etc.) to cell optimization.

Although the progress of continuum models is encouraging and there are many studies that have used experimental data to validate their models, to date, there is no study that utilizes macroscale models to contribute directly to the development of better lithium sulfur cells. For experimentalists to use modeling insights to engineer better cells, the modeling community should focus on models that closely resemble state-of-the-art high energy density lithium sulfur cells. This would require alignment of parameters that are physically meaningful and reporting cell-level metrics that are relevant as there is currently a disconnect between model parameters and cell-level design. Also, models that pay attention to details like concentration-dependent electrolyte resistance, concentration solution theory, and transport limitations will be able to model accurate cell performance under low E/S conditions.

Models can guide electrolyte engineering efforts as they can help elucidate reaction schemes through validation with voltage curves but also other electrochemical measurements like CV. However, there is still a fundamental gap that exists due to the inability of existing models to replicate voltage features for both discharging and charging. Possible approaches to resolve this charging challenge are to more thoroughly validate parameters experimentally, understand parallel mechanisms that may allow different pathways during charge versus discharge, or include limiting phenomena that a cell undergoes when charging. It is key to recognize that many parameters in LiS modeling have been assumed without proper independent validation. Creative electroanalytical approaches to measuring these key parameters under realistic battery electrolyte conditions is essential, e.g., solubility products. Likewise, continuum models can be coupled with DFT and AIMD simulations to inform reaction rate constants and conductivities.[23] Only then should the remaining parameters be estimated through fits to experimental data.

Shuttling remains one the major challenges for lithium sulfur as it is the main cause of irreversible capacity loss. Experimental strategies like coatings, additives, and design of cathode structure can help retain and trap polysulfides in the cathode or preventing passivation on the anode can be informed by modeling. Continuum-scale physics-based models can go beyond describing experimental observations to helping ensure these novel engineering strategies result in quantitatively optimal designs. An important aspect of this optimal design will include more detailed morphological modeling of the lithium anode to improve cycling performance. Note that detailed meso-scale models should also be carefully studied with proper boundary conditions for mass and charge conservation,[106] and numerical mesh/grid convergence studies should be reported to make sure that the results have at least qualitatively converged. As cathode engineering becomes more sophisticated, such as developing micro- and nano-structures for improved conductivity while reducing surface passivation and pore clogging effects, models that move beyond a typical porous composite structure can help understand the evolution of morphology under different conditions and can help optimize engineering designs like particle and pore sizes.

List of Symbols

| | |
|---|---|
| $a$ | *Specific surface area of cathode, $m^2/m^3$* |
| $a_0$ | *Initial value of a, $m^2/m^3$* |
| $b$ | *Bruggeman coefficient* |
| $C_{i,ref}$ | *Reference concentration of species i, $mol/m^3$* |
| $C_{m,i}$ | *Concentration of species i in region m, $mol/m^3$* |
| $D_{i0}$ | *Diffusion coefficient of species i in the bulk medium, $m^2/s$* |
| $D_i$ | *Diffusion coefficient of species i in the porous medium, $m^2/s$* |
| $F$ | *Faraday constant, C/mol* |
| $i_{0,jref}$ | *Exchange current density of reaction j at reference concentrations, $A/m^2$* |
| $i_{app}$ | *Applied current density, $A/m^2$* |
| $i_j$ | *Current density from reaction j, $A/m^2$* |
| $i_{m,e}$ | *Superficial current density in the electrolyte phase in region m, $A/m^2$* |
| $i_s$ | *Superficial current density in the solid phase, $A/m^2$* |
| $k_k$ | *Rate constant of precipitate k, varying units, see Ref.* [29] |
| $K_{sp,k}$ | *Solubility product of precipitate k, varying units, see Ref.* [29] |
| $l_1$ | *Thickness of the cathode, m* |
| $l_2$ | *Thickness of the separator, m* |
| $N_{m,i}$ | *Superficial flux of species i in region m, mol $m^2$ $s^{-1}$* |
| $n_j$ | *Number of electrons transferred in electrochemical reaction j* |
| $R$ | *Gas constant, J $mol^{-1}$ $K^{-1}$* |
| $r_i$ | *Production rate of species i from electrochemical reactions, mol $m^3$ $s^{-1}$* |
| $r_i'$ | *Production rate of species i from electrochemical reactions at the interface between the separator and anode, mol $m^{-2}$ $s^{-1}$* |
| $R_k'$ | *Rate of precipitation of solid species k, mol $m^3$ $s^{-1}$* |
| $R_{m,i}$ | *Production rate of species i due to precipitation reactions in region m, mol $m^3$ $s^{-1}$* |
| $s_{a,j}$ | *Stoichiometric coefficient of anodic species in electrochemical j* |
| $s_{c,j}$ | *Stoichiometric coefficient of cathodic species in electrochemical j* |
| $s_{i,j}$ | *Stoichiometric coefficient of species i in electrochemical reaction j* |
| $T$ | *Temperature, K* |
| $t$ | *Time, s* |
| $U_j^{\theta}$ | *Standard Open Circuit Potential (OCP) of electrochemical reaction j, V* |
| $U_{j,ref}$ | *OCP of electrochemical reaction j at reference concentrations, V* |
| $\tilde{V}_k$ | *Molar volume of the precipitate k, $m^3/mol$* |
| $z_i$ | *Charge number of species i* |

*Greek symbols*

| | |
|---|---|
| $\alpha_{aj}$ | *Anodic transfer coefficient of reaction j* |
| $\alpha_{cj}$ | *Cathodic transfer coefficient of reaction j* |
| $\gamma_{i,k}$ | *Number of ionic species i produced by the dissociation of precipitate k* |
| $\varepsilon_m$ | *Porosity of region m* |
| $\varepsilon_{m,k}$ | *Volume fraction of precipitate k in region m* |
| $\eta_j$ | *Overpotential for electrochemical reaction j* |
| $\xi$ | *Morphology parameter* |
| $\sigma$ | *Effective conductivity of solid phase of the cathode, S/m* |
| $\phi_{m,e}$ | *Potential in the liquid phase in region m, V* |
| $\phi_s$ | Potential in the solid phase, V |

# Chapter 3: Model-Guided Strategies for Probing Lithium Sulfur Batteries through GITT

Note: this chapter is in preparation to be published as an article

## Abstract

The thermodynamic equilibrium voltage of lithium sulfur (LiS) batteries is an important starting point for designing LiS cells and for building complex physics-based models. This can be found by the electroanalytical method of galvanostatic intermittent titration technique (GITT). In this work, we simulate GITT experiments with parameters that correspond to a practical high energy density LiS cell using a previously established 1D full physics model. We also present a simpler thermodynamic model to easily obtain the thermodynamic equilibrium voltage. We explore the thermodynamic speciation and solubility of polysulfides using these models, specifically $Li_2S$ precipitation and $S_6^{2-}$ to $S_3^{\bullet-}$ dissociation chemistry. This has implications for accelerating cell design and optimization, particularly in furthering our understanding of thermo-kinetic parameters in relation to solvent engineering.

## 3.1 Introduction

Lithium sulfur (LiS) is a promising cathode chemistry as it has a theoretical capacity of 1675 mAh/g, thus unlocking energy densities that are projected to be two to three times higher than that of lithium-ion batteries.[1] Sulfur is also a cheap and abundant material which is attractive for cost reduction and supply chain reliability of batteries. However, there are significant challenges standing in the way of the widespread commercial adoption of LiS cells. LiS cathodes are conventionally paired with a lithium metal anode and an organic liquid electrolyte. During discharge of an LiS cell, solid sulfur is reduced to soluble higher order lithium polysulfides, which go through a series of reduction, dissociation, or disproportionation reactions to form lower order polysulfides which can be insoluble (mainly $Li_2S$ , but sometimes $Li_2S_2$, depending on solvent). The process reverses during charging. Solid sulfur and its solid discharge product are insulating, so composites are made with conductive carbon, which lowers the net energy density, impacts charge transfer rates, contributes to high internal resistance, and presents a barrier for efficient electrochemical reaction pathways.[46] More facile charge transfer kinetics can occur for the polysulfides in solution, but soluble polysulfides can travel to the anode and react with the lithium metal. This shuttling phenomenon causes low Coulombic efficiency and active material loss, leading to self-discharge and capacity loss over time. A passivating layer of lithium polysulfides can also form on the anode because of this, and coupled with the dendrite formation and dead lithium issues typical of lithium anodes, can lead to safety and cyclability issues.[107] There has been active research to tackle the above challenges such as the design of advanced composite cathode structures (e.g. micro-/meso-porous carbon spheres and nanoparticles, hollow carbon nanofibers, etc.), the use of engineered coatings on the cathode, separator, and anode, as well as electrolyte engineering, including solvent design and the use of additives that passivate the lithium metal surface (e.g. $LiNO_3$).[1] These and other fundamental issues associated with the performance and modeling of LIS batteries have recently been reviewed.[22] Models, in theory, can help accelerate the development of LiS batteries by providing insight on internal states of an operating cell, thereby quickening the design and optimization process. However, the intrinsic complexity of LiS battery chemistry makes the testing of mechanistic assumptions and estimating parameters especially challenging.

The vast majority of continuum models are tested against experimental discharge curves under a limited number of C-rates.[29,31] Only a few continuum models have been tested against other standard battery cycling measurements such as charging curves[57] and capacity fade.[83] Likewise, more advanced electroanalytical methods such as cyclic voltammetry (CV),[43] potentiostatic intermittent titration technique (PITT),[52] and electrochemical impedance spectroscopy (EIS)[100] are also rarely compared to detailed LiS models. Instead, electroanalytical experiments involving LiS chemistries tend to be interpreted phenomonologically. For example, galvanostatic intermittent titration technique (GITT) of LiS batteries has mainly been used to find the internal resistance as a function of voltage,[8] or to find the thermodynamic equilibrium voltage after relaxation following the cessation of current. The thermodynamic equilibrium voltage obtained using GITT has been used to compare different electrolyte systems,[9] to compare overpotentials due to different electrolyte to sulfur ratios (E/S),[10] or to understand $Li_2S$ precipitation dynamics.[11]

Despite the special challenge of LiS model validation and parameterization, and the value experimentalists have placed on the interpretive power of more advanced dynamic and thermodynamic measurements like GITT, there is a dearth of literature on model-guided electroanalytical experimental design to identify testing conditions that are sensitive to model physics and specific parameters. The focus of this work is to show the potential insights model-guided electroanalysis can have in LiS modeling by considering how different chemical assumptions and governing physics plays out in the dynamic and thermodynamic response of simulated GITT experiments. Here we model the dynamics of a GITT experiment and its relation to equilibrium using an established 1D physics model that contains thermodynamics, kinetics, and transport that embodies two chemical mechanisms for discharge. We also present a simpler model that only has thermodynamics. Using these two models we explore the additional information GITT can give us beyond typical discharge curves – thermodynamic equilibrium voltages and transient relaxation voltage responses. This can be helpful in identifying thermo-kinetic parameters in the literature especially given there are ~42+ parameters in similar models, some of which are assumed, and some of which discharge curves are wholly insensitive to. In particular, we look at parameters relating to $Li_2S$ precipitation and alternative reaction speciation mechanisms, in this case, the presence or absence of homogeneous $S_6^{2-}$ to $S_3^{\bullet -}$ dissociation chemistry. While not a comprehensive set of different polysulfide and ion-paired species that have been modeled for the

LiS system, we use these alternatives to show the value of model-guided electroanalysis for distinguishing parameters and behaviors associated with each set of chemical mechanisms.

## 3.2 Methods

### 3.2.1 Overview of reaction mechanisms

The electrochemical reactions we model in this work are:

$$Li \rightleftharpoons Li^{+} + e^{-} \tag{3.1}$$

$$\frac{1}{2}S_{8(l)} + \mathrm{e}^{-} \rightleftharpoons \frac{1}{2}S_8^{2-} \tag{3.2}$$

$$\frac{3}{2}S_8^{2-} + \mathrm{e}^{-} \rightleftharpoons 2S_6^{2-} \tag{3.3}$$

$$S_6^{2-} + \mathrm{e}^{-} \rightleftharpoons \frac{3}{2}S_4^{2-} \tag{3.4}$$

$$\frac{1}{2}S_4^{2-} + \mathrm{e}^{-} \rightleftharpoons S_2^{2-} \tag{3.5}$$

$$\frac{1}{2}S_2^{2-} + \mathrm{e}^{-} \rightleftharpoons S^{2-} \tag{3.6}$$

The dissolution and precipitation reactions are:

$$S_{8(l)} \rightleftharpoons S_{8(s)} \tag{3.7}$$

$$2Li^{+} + S^{2-} \rightleftharpoons Li_2S_{(s)} \tag{3.8}$$

Later in the paper, if specified, we also add an additional dissociation reaction:

$$S_6^{2-} \rightleftharpoons 2S_3^{\bullet-} \tag{3.9}$$

This is to account for the formation of a radical anion which has been detected in common LiS electrolytes using Raman and NMR spectroscopy summarized by Steudel and Chivers.[108] The above reaction (Eq. (3.9)) can be described by the reaction equilibrium constant, $K_{S3}$,

$$K_{S3} = \frac{k_{f,S3}}{k_{b,S3}} = \frac{[S_3^{\bullet -}]^2}{[S_6^{2-}]} \tag{3.10}$$

where $k_{f,S3}$ and $k_{b,S3}$ are the forward and backward rate constants of the reaction, and [*i*] represent concentrations of species *i* in mol/m$^3$.

### 3.2.2 Governing equations for 1D full physics model

The 1D full physics model is based on equations developed by Kumaresan et al. which includes Nernstian equilibrium thermodynamics, Butler-Volmer and precipitation kinetics, diffusive and migrative transport, and porous electrode theory.[29] The result is a highly coupled differential algebraic system containing 20 partial differential equations and 3 algebraic equations. The set of governing equations can be found in

***Table 3.1***. A number of other papers using the Kumaresan model have provided good summaries of the governing equations.[101] In this work, the noteworthy deviations are:

- We do not include solid precipitates of intermediate polysulfides, the only solids we consider are S8(s) and Li2S(s).
- The anode is not modeled and is taken as a boundary condition. Instead of modeling the electrochemical reaction at the anode, we model it as a perfectly protected lithium foil which provides a constant source of lithium ions at the anode-separator interface,

$$N_{s,Li^+} = -\frac{i_{app}}{F} \tag{3.11}$$

where $N_{s,Li^+}$ is the flux of $Li^+$ ions in the separator, $i_{app}$ is the applied current density in $A/m^2$, and $F$ is Faraday's constant. Overpotential at the anode is very small and can be assumed to be negligible here.

- The dependent variable, concentration of an arbitrary anion in the salt, $C_{A-}$, is eliminated through substitution of the following electroneutrality expression into the flux, $N_{A-}$.

$$C_{A-} = C_{Li^+} - 2*(C_{S_8^{2-}} + C_{S_6^{2-}} + C_{S_4^{2-}} + C_{S_2^{2-}} + C_{S^{2-}}) \tag{3.12}$$

$C_i$ represents the concentration of species *i*.

- We use an effective electronic conductivity $\sigma_{eff} = \sigma(1-\varepsilon_c)^{brug}$ with $\varepsilon_c$ as the cathode porosity and *brug* as the Bruggeman coefficient.
- We rewrite the open-circuit potential and Butler-Volmer kinetic equations to eliminate the use of arbitrary reference concentrations, $C_{i,ref}$, present in Kumaresan et al.[29] and other following papers. Instead, we write the open circuit potential as a standard Nernst equation.

$$U_j = U_j^\theta - \frac{RT}{n_j F}\left(\sum_i s_{i,j} ln\left[\frac{C_i}{1000}\right]\right) \tag{3.13}$$

where $U_j$ and $U_j^\theta$ are the equilibrium potential and standard equilibrium potential of reaction j respectively. R is the molar gas constant, T is temperature, $n_j$ is the number of electrons transferred in reaction j, F is Faraday's constant, $s_{i,j}$ is the stoichiometric coefficient of species i in reaction j, and 1000 in the denominator is to convert units from mol/m3 to mol/L. We also follow the Butler-Volmer equation formulation in Chapter 8 of Newman and Thomas-Alyea[109] (equations 8.24 and 8.30) for the current density of reactions j, in A/m2,

$$i_j = k_j \prod_{i=red} C_i^{\alpha p_{i,j}} \prod_{i=ox} C_i^{(1-\alpha) q_{i,j}} \left[ e^{\frac{(1-\alpha) n_j F}{RT}\eta_j} - e^{\frac{-\alpha n_j F}{RT}\eta_j} \right] \tag{3.14}$$

Where $k_j$ is the rate constant of reaction *j* with units of $\frac{A}{m^2}\left[\frac{m^3}{mol}\right]^{\alpha p_{i,j}+(1-\alpha)q_{i,j}}$, $p_{i,j}=s_{i,j}$ for anodic or reduced species, and $q_{i,j}=-s_{i,j}$ for cathodic or oxidized species, $\alpha$ is the charge transfer coefficient, and $\eta_j$ is the overpotential. This formulation of Eq. (3.13) ensures that the overpotentials of each reaction j is zero when the individual faradaic reaction currents densities, $i_j$, and the total applied current are zero, which is not true for the Kumaresan equation formulation and other work that use the same equation set. The formulation we use here is same as in Danner and Latz,[52] and through mathematical rearrangement, consistent with Kumaresan et al., where the value of $k_j$ defined here can be expressed using Kumaresan's reference exchange current densities and concentrations as,

$$k_j = i_{0,j,ref}\prod_{i=red}\left(\frac{1}{C_{i,ref}}\right)^{\alpha p_{i,j}}\prod_{i=ox}\left(\frac{1}{C_{i,ref}}\right)^{(1-\alpha)q_{i,j}} \tag{3.15}$$

The values of $k_j$ provided in Table 3.3 is calculated using this formula from assumed $i_{0,j,ref}$ values taken from Kumaresan et al., unless stated otherwise.

***Table 3.1 Equations for 1D full physics lithium sulfur model***

| Governing Equations | Boundary Conditions |
|---|---|
| Cathode | |
| $\frac{\partial \varepsilon_c C_{c,i}}{\partial t} = -\frac{\partial N_{c,i}}{\partial x} + r_i - R_{c,i}$ | $N_{c,i}\big\|_{x=0} = 0$ |
| $N_{c,i} = -D_{eff,i}\frac{\partial C_{c,i}}{\partial x} - z_i\frac{D_{eff,i}}{RT}FC_{c,i}\frac{\partial \phi_{c,2}}{\partial x}$ | $i_1\big\|_{x=0} = -i_{app}$ |
| $i_1 + i_{c,2} = -i_{app}$ | $i_{c,2}\big\|_{x=0} = 0$ |
| $\frac{\partial i_1}{\partial x} = a\sum_j i_j$ | $i_{c,2}\big\|_{x=L_{cat}} = i_{s,2}\big\|_{x=L_{cat}}$ |
| $\frac{\partial \varepsilon_{c,k}}{\partial t} = \tilde{V}_k R'_{c,k}$ | $\phi_{c,2}\big\|_{x=L_{cat}} = \phi_{s,2}\big\|_{x=L_{cat}}$ |

| | |
|---|---|
| $\frac{\partial \varepsilon_c}{\partial t} = -\sum_k \tilde{V}_k R'_{c,k}$ | $i_1 \rvert_{x=L_{cat}} = 0$ |
| Separator (Region 2) | |
| $\frac{\partial \varepsilon_s C_{s,i}}{\partial t} = -\frac{\partial N_{s,i}}{\partial x} - R_{s,i}$ | $C_{c,i} \rvert_{x=L_{cat}} = C_{s,i} \rvert_{x=L_{cat}}$ |
| $N_{s,i} = -D_{eff,i} \frac{\partial C_{s,i}}{\partial x} - z_i \frac{D_{eff,i}}{RT} F C_{s,i} \frac{\partial \phi_{s,2}}{\partial x}$ | $N_{c,i} \rvert_{x=L_{cat}} = N_{s,i} \rvert_{x=L_{cat}}$ |
| $i_{s,2} = -i_{app}$ | |
| $\frac{\partial \varepsilon_{s,k}}{\partial t} = \tilde{V}_k R'_{s,k}$ | $N_{s,i} \rvert_{x=L_{cat}+L_{sep}} = 0, \quad N_{s,Li^+} \rvert_{x=L_{cat}+L_{sep}} = -\frac{i_{app}}{F}$ |
| $\frac{\partial \varepsilon_s}{\partial t} = -\sum_k \tilde{V}_k R'_{s,k}$ | $\phi_{s,2} \rvert_{x=L_{cat}+L_{sep}} = 0$ |
| Other Expressions | |
| $r_i = -a \sum_j \frac{s_{i,j} i_j}{n_j F}$ | $a = a_0 \left( \frac{\varepsilon}{\varepsilon_{initial}} \right)^{\xi}$ |
| $i_1 = -\sigma \frac{\partial \phi_1}{\partial x}$ | $i_2 = F \sum_i z_i N_i$ |
| $\eta_j = \phi_1 - \phi_2 - U_j$ | $U_j = U_j^{\theta} - \frac{RT}{n_j F} \left( \sum_i s_{i,j} ln \left[ \frac{C_i}{1000} \right] \right)$ |
| $D_{eff,i} = \varepsilon^{brug} D_{0,i}$ | $\sigma_{eff} = \sigma (1 - \varepsilon_c)^{brug}$ |
| $R_i = \sum_k \gamma_{i,k} R'_k$ | $R'_k = k_k \varepsilon_k \left( \prod_i C_i^{\gamma_{i,k}} - Ksp_k \right)$ |
| $i_j = k_j \prod_{i=red} C_i^{\alpha p_{i,j}} \prod_{i=ox} C_i^{(1-\alpha) q_{i,j}} \left[ e^{\frac{(1-\alpha) n_j F}{RT} \eta_j} - e^{\frac{-\alpha n_j F}{RT} \eta_j} \right]$ | |

### 3.2.3 Governing equations for the thermodynamic equilibrium model

The thermodynamics of a lithium sulfur cell, modeling both the cathode and separator domains, can be described by 8-9 algebraic equations given the following assumptions:

1. The system is in an equilibrated relaxed state.
2. There are three regions of depths-of-discharge (DODs) that have different sets of governing equations – region 1 at low DOD has only the solid $S_8$, region 2 has no solids, and region 3 at has only the solid product $Li_2S$.

3. $S_{8(s)}$ is completely reduced to the final form $Li_2S_{(s)}$. Our definition of DOD is defined by the average oxidation state of sulfur going from 0 to 2 for 0-100% DOD.
4. Volume fractions of $S_{8(s)}$ and $Li_2S_{(s)}$ in the separator are negligible. All $S_{8(s)}$ stays in the cathode and any $Li_2S_{(s)}$ formed happens in the cathode. This is not strictly true, but previous dynamic simulations show that volume fractions of the two solids in the separator are several orders of magnitude smaller than that in the cathode.

All three regions have the same 8 unknowns – concentrations of 7 ionic species *i*, $C_i$ , and the solid phase potential, $\phi_1$, – with region 1 and 3 having a ninth unknown variable, the volume fraction of $S_{8(s)}$ and $Li_2S_{(s)}$, or $\varepsilon_{S_8}$ and $\varepsilon_{Li_2S}$ , respectively. In an equilibrated cell, concentrations in the cathode are the same as that in the separator. The volume fractions of the solids refer to that in the cathode as we assume volume fractions in the separator are zero.

There are 5 Nernst equations describing each of the 5 electrochemical reactions *j*. The classic Nernst equation in Eq. (3.13) is modified as the system at equilibrium can have only one voltage, so $U_j = V = \phi_1 - \phi_2$.

$$\phi_1 = U_j^\theta - \frac{RT}{n_j F}\left(\sum_i s_{i,j} ln\left[\frac{C_i}{1000}\right]\right) \tag{3.16}$$

where $\phi_1$ and $\phi_2$ are the solid and liquid phase potentials respectively. The liquid phase potential is assumed to be zero as a reference point and eliminated from this equation.

The total number of moles of sulfur atoms per cross-sectional area, $S_{bal}$ , with units mol/m$^2$, is conserved in the system,

$$S_{bal} = (\varepsilon_c L_{cat} + \varepsilon_s L_{sep}) * (8C_{S_8^{2-}} + 6C_{S_6^{2-}} + 4C_{S_4^{2-}} + 2C_{S_2^{2-}} + C_{S^{2-}}) + \frac{8 * \varepsilon_{S_8} L_{cat}}{\tilde{V}_{S_8}} + \frac{\varepsilon_{Li_2S} L_{cat}}{\tilde{V}_{Li_2S}} \tag{3.17}$$

where $\varepsilon_c$ and $\varepsilon_s$ are cathode and separator porosity, $L_{cat}$ and $L_{sep}$ are the cathode and separator thickness, $\tilde{V}_{S_8}$ and $\tilde{V}_{Li_2S}$ are the molar volume of $S_{8(S)}$ and $Li_2S_{(s)}$. All species in the solution phase have their concentrations multiplied by respective cathode or separator porosity to account for volume in the porous electrode. Concentrations of the solid phase species are represented by their volume fraction and molar volume.

There is a charge balance constraint where the amount of charge stored in the sulfur species (left-hand side of Eq. (3.18)) is equivalent to the charge put into the system (right-hand side).

$$2*(\varepsilon_c L_{cat} + \varepsilon_s L_{sep})*(C_{S_8^{2-}} + C_{S_6^{2-}} + C_{S_4^{2-}} + C_{S_2^{2-}} + C_{S^{2-}}) + \frac{2*\varepsilon_{Li_2S} L_{cat}}{\tilde{V}_{Li_2S}} = 2*DOD/100*S_{bal} \quad (3.18)$$

All polysulfides in the liquid phase has a charge of 2. $Li_2S_{(s)}$ is the only species in the solid phase that has charge put into it and is accounted for in the last term on the left-hand side of Eq. (3.18). The charge put into the system can be defined by the average oxidation state of sulfur, as explained in assumption 3, multiplied by the total number of sulfur atoms.

Electroneutrality also needs to be conserved, where the sum of all positively charged species is the same as all negatively charged species.

$$C_{Li^+} = \frac{\varepsilon_{c,0} C_{A^-,ref}}{\varepsilon_c} + 2*(C_{S_8^{2-}} + C_{S_6^{2-}} + C_{S_4^{2-}} + C_{S_2^{2-}} + C_{S^{2-}}) \quad (3.19)$$

where $C_{A^-,ref}$ is the reference concentration of the anion in the salt when cathode porosity is $\varepsilon_{c,0}$ at 0% DOD. This first term on the right-hand side is basically $C_{A^-}$, written as above to account for it changing with DOD due to the changing porosity. The anion is not consumed at all, and number of moles is constant.

For the 9th equation in region 1, we have the additional solubility constraint for the solid $S_{8(s)}$,

$$C_{S_{8(l)}} = Ksp_{S8} \quad (3.20)$$

where Ksp represents the solubility product of a precipitate.

For the 9th equation in region 3, the solubility constraint for the solid $Li_2S_{(s)}$,

$$C_{Li^+}{}^2 C_{S^{2-}} = Ksp_{Li_2S} \quad (3.21)$$

### 3.2.4 Modifications to include $S_6^{2-}$ to $S_3^{\bullet-}$ dissociation chemistry

Part of our investigation includes addition of the reaction shown in Eq. (3.9), although if not specifically mentioned, the base case for all other scenarios described does not include this reaction.

*Modifications to the 1D full model*

For the 1D full model, we use the same governing equations described by Parke et al., which made modifications to include this chemical reaction.[47] The species balance for $S_6^{2-}$ is modified to,

$$\frac{\partial \varepsilon C_{S_6^{2-}}}{\partial t} = -\frac{\partial N_{S_6^{2-}}}{\partial x} + r_{S_6^{2-}} - \varepsilon k_{f,S3}\left(C_{S_6^{2-}} - \frac{C_{S_3^{\bullet-}}^2}{K_{S3}}\right) \tag{3.22}$$

where $\varepsilon$, $N_i$, $r_i$, and $C_i$, are generic porosity, flux of species *i*, production rate of species *i* from electrochemical reactions, and concentration of species *i*, all of which can refer to either in the cathode or separator.

A new species balance for $S_3^{\bullet-}$ is also needed.

$$\frac{\partial \varepsilon C_{S_3^{\bullet-}}}{\partial t} = -\frac{\partial N_{S_3^{\bullet-}}}{\partial x} + 2\varepsilon k_{f,S3}\left(C_{S_6^{2-}} - \frac{C_{S_3^{\bullet-}}^2}{K_{S3}}\right) \tag{3.23}$$

Similar flux and concentration boundary conditions, see

***Table 3.1***, for the $S_3^{\bullet-}$ species have to be added too.

*Modifications to the thermodynamic equilibrium model*

For the thermodynamic equilibrium model, we modify the sulfur mole balance (Eq. (3.17)), charge balance (Eq. (3.18)), and electroneutrality (Eq. (3.19)) equations by adding and accounting for $S_3^{\bullet-}$ terms.

Those three modified equations, respectively, are:

$$S_{bal} = (\varepsilon_c L_{cat} + \varepsilon_s L_{sep}) * (8C_{S_8^{2-}} + 6C_{S_6^{2-}} + 4C_{S_4^{2-}} + 2C_{S_2^{2-}} + C_{S^{2-}} + 3C_{S_3^{\bullet -}}) + \frac{8 * \varepsilon_{S_8} L_{cat}}{\tilde{V}_{S_8}} + \frac{\varepsilon_{Li_2S} L_{cat}}{\tilde{V}_{Li_2S}} \quad (3.24)$$

$$2 * (\varepsilon_c L_{cat} + \varepsilon_s L_{sep}) * (C_{S_8^{2-}} + C_{S_6^{2-}} + C_{S_4^{2-}} + C_{S_2^{2-}} + C_{S^{2-}} + \frac{C_{S_3^{\bullet -}}}{2}) + \frac{2 * \varepsilon_{Li_2S} L_{cat}}{\tilde{V}_{Li_2S}} = 2 * DOD / 100 * S_{bal} \quad (3.25)$$

$$C_{Li^+} = \frac{\varepsilon_{c,0} C_{A^-,ref}}{\varepsilon_c} + 2 * (C_{S_8^{2-}} + C_{S_6^{2-}} + C_{S_4^{2-}} + C_{S_2^{2-}} + C_{S^{2-}}) + C_{S_3^{\bullet -}} \quad (3.26)$$

We also add the definition of the reaction equilibrium constant, $K_{S3}$, defined in Eq. (3.10), as an additional equation since we have an additional unknown variable.

### 3.2.5 Computational methods

For the 1D model, we used orthogonal collocation with Legendre polynomials to discretize the partial differential equations in *x*, choosing 5 collocation points to ensure convergence. A robust initialization strategy was used to find consistent initial conditions for the system of differential algebraic equations. The set of equations was then solved in *Maple 2018* using the stiff solver based on semi-implicit Runge-Kutta called using the *dsolve* command in implicit mode.

For the thermodynamic equilibrium model, the system of algebraic equations was solved at intervals of 0.1-1% DOD, as needed. Since the solver is sensitive to initial guesses, we start with reasonable guesses given in Table 3.7 for 1% DOD in region 1. We solve for solutions at 1% DOD and use these solutions as initial guesses for the next step e.g., 2% DOD. We repeat for each incremental DOD until $\varepsilon_{S_8} < 10^{-3}$ or the solution fails to converge. We then start from 99% DOD in region 3, again with reasonable guesses given in Table 3.7, this time using the solution as initial guesses for the next decreasing DOD until $\varepsilon_{Li_2S} < 10^{-3}$ or the solution fails to converge. For the remaining DODs in between these two regions, we use the governing equations corresponding to region 2 to solve in the same sequential manner, starting from low to high DOD. All dependent variables were log-scaled prior to solving for stability purposes, since they vary by many orders of magnitude. This system of equations was solved using an in-house sparse Newton solver in *Maple*. We also provide the sets of equations and method to solve using Julia on github, where we use forward auto-differentiation and Newton method in the *nlsolve.jl* package. Solutions solved using both programs converge to each other.

### 3.2.6 Parameters and initial conditions

The applied current, $i_{app}$, used at a given C-rate, is based on theoretical capacity,

$$i_{app} = -\frac{\varepsilon_{c,S_8,inital} L_{cat}}{\tilde{V}_{S_8}} * \frac{16F}{3600} * \frac{C\_rate}{utilization\_ratio} \tag{3.27}$$

where the first term refers to the number of moles/m$^2$ of $S_{8(s)}$ in the cathode initially when fully charged, and the second term converts that to amount of charge/hour (16 electrons accepted from the full conversion of $S_8$ to $S^{2-}$). *utilization_ratio* is used to account for the sulfur utilization not being a 100% experimentally, i.e. cell's capacity is less than theoretical capacity. This is adjusted for simulated data to match experimental data at the same C-rate. A negative applied current represents discharge.

In Table 3.2, we report the geometric parameters of the cell, including cell-level metrics such as E/S ratio and sulfur loading, for feasible cell designs capable of producing high energy density LiS batteries.[26] Table 3.3 contains kinetic, and thermodynamic parameters concerning the electrochemical reactions. We use Eq. (3.15) and values from Kumaresan et al.[29] to obtain values of $i_{0,j}$. $i_{0,6}$ and $U_j^\theta$ are adjusted to match experimental data. Table 3.4 contains parameters for the ionic species such as diffusion coefficients and reference concentrations. Notably, we reduce the diffusion coefficients by a factor of two from work by Parke et al.[47] to observe the trend of C-rate-dependent discharge capacities. Reference concentrations reported here are no longer parameters of the model but used as initial conditions in this work. Table 3.5 contains cathode and separator parameters, and Table 3.6 contains precipitation related parameters. Note that we adjust the rate constant and solubility product associated with the $Li_2S$ precipitation which will be discussed later.

Table 3.7 contains initial guesses for the thermodynamic model at 1% and 99% DOD. Alternatively, a sufficiently good initial guess can be obtained through a C/20 discharge of the 1D dynamic model. In all cases, the temperature is assumed to be 298K.

***Table 3.2 Geometric parameters***

| Parameter | Value |
|---|---|
| Cathode thickness (µm) [a] | 100 |
| Separator thickness (µm) [a] | 20 |
| Sulfur volume fraction [a] | 0.24 |
| Carbon/binder volume fraction [a] | 0.16 |
| Cathode porosity [a] | 0.60 |
| Separator porosity [a] | 0.60 |
| Areal sulfur loading (mg/cm$^2$) [b] | 4.9 |
| E/S ratio (mL/g) [b] | 1.45 |
| Theoretical areal capacity (mAh/cm$^2$) [b] | 8.31 |

***Table 3.3 Properties of the electrochemical reactions.***

| Reaction *(j)* | $k_j\left(\frac{A}{m^2}\left[\frac{m^3}{mol}\right]^{\alpha p_{i,j}+(1-\alpha)q_{i,j}}\right)$ | $U_j^\theta$ (V) | $s_{a,j}$ | $s_{c,j}$ | $\alpha$ |
|---|---|---|---|---|---|
| **2** | 1.45 [c] | 2.42 [d] | -1/2 | 1/2 | 1/2 |
| **3** | 0.214 [c] | 2.39 [d] | -3/2 | 2 | 1/2 |
| **4** | 0.628 [c] | 2.25 [d] | -1 | 3/2 | 1/2 |
| **5** | 0.724 [c] | 2.06 [d] | -1/2 | 1 | 1/2 |
| **6** | 0.765 [d] | 1.8 [d] | -1/2 | 1 | 1/2 |

***Table 3.4 Transport properties and reference concentrations.***

| Species (*i*) | $z_i$ | $D_{0,i}$ (m$^2$/s) | $C_{i,ref}$ (mol/m$^3$) |
|---|---|---|---|
| $Li^+$ | +1 | 5 x $10^{-12}$ [e] | 1001 [f] |
| $S_{8(l)}$ | 0 | 5 x $10^{-11}$ [e] | 19.0 [f] |
| $S_8^{2-}$ | -2 | 3 x $10^{-11}$ [e] | 0.178 [f] |
| $S_6^{2-}$ | -2 | 3 x $10^{-11}$ [e] | 0.324 [f] |
| $S_4^{2-}$ | -2 | 5 x $10^{-12}$ [e] | 0.020 [f] |

| | | | |
|---|---|---|---|
| $S_2^{2-}$ | -2 | 5 x $10^{-12}$ [e] | 5.23 x $10^{-7}$ [f] |
| $S^{2-}$ | -2 | 5 x $10^{-12}$ [e] | 8.27x $10^{-10}$ [f] |
| $A^{-}$ | -1 | 3.5 x $10^{-10}$ [e] | 1000 [f] |
| $S_3^{\bullet -}$ | -1 | 5 x $10^{-12}$ [e] | 1.0 x $10^{-4}$ [a] |

***Table 3.5 Cathode and separator parameters.***

| Parameter | Cathode | Separator |
|---|---|---|
| $a_0$ (m$^2$/m$^3$) | 143292 [a] | - |
| $\varepsilon_{initial}$ | 0.6 [a] | 0.6 [a] |
| $\varepsilon_{S_{8(s)},initial}$ | 0.24 [a] | 1 x $10^{-12}$ [a] |
| $\varepsilon_{Li_2S_{(s)},initial}$ | 1 x $10^{-7}$ [a] | 1 x $10^{-7}$ [a] |
| $\sigma$ (S/m) | 60 [g] | - |
| $\xi$ | 1.5 | - |
| *brug* | 1.5 | 1.5 |

***Table 3.6 Parameters for the precipitation reactions.***

| Precipitate ($k$) | Rate Constant ($k_k$) | Solubility Product $(K_{sp,k})$ | Molar Volume $(V_k)$ (m$^3$/mol) |
|---|---|---|---|
| $S_{8(s)}$ | 1.0 s$^{-1}$ [f] | 19.0 mol m$^{-3}$ [f] | 1.239 x $10^{-4}$ [f] |
| $Li_2S_{(s)}$ | 5.0 x $10^{-5}$ m$^6$ mol$^2$ s$^{-1}$ [d] | 2.0 x $10^4$ mol$^3$ m$^{-9}$ [d] | 2.768 x $10^{-5}$ [f] |

[a] Input parameters to the model, taken from Ref [47]
[b] Calculated but not used in model
[c] Calculated using Eq. (3.15) using values from Ref [29]
[d] Adjusted
[e] Adjusted to be smaller by a factor of 2 from Ref [47]
[f] From Ref [29]
[g] From Ref [83]

***Table 3.7 Initial guesses for the thermodynamic equilibrium model.***

| Variable | 1% DOD | 99% DOD |
|---|---|---|
| $C_{Li^+}$ (mol/m$^3$) | 1240 | 1100 |
| $C_{S8_{(l)}}$ (mol/m$^3$) | 19.0 | $7.81 \times 10^{-12}$ |
| $C_{S_8^{2-}}$ (mol/m$^3$) | 40.9 | $2.59 \times 10^{-4}$ |
| $C_{S_6^{2-}}$ (mol/m$^3$) | 74.7 | 0.591 |
| $C_{S_4^{2-}}$ (mol/m$^3$) | 4.66 | 46.1 |
| $C_{S_2^{2-}}$ (mol/m$^3$) | $1.21 \times 10^{-4}$ | 1.49 |
| $C_{S^{2-}}$ (mol/m$^3$) | $1.91 \times 10^{-7}$ | 0.0832 |
| $\phi_1$ (V) | 2.38 | 2.17 |
| $\varepsilon_{S_8}$ | 0.149 | - |
| $\varepsilon_{Li_2S}$ | - | 0.286 |
| $C_{S_3^{\bullet -}}$ (mol/m$^3$) | $\sqrt{K_{S3}*1000}$ | |

## 3.3 Results and Discussion

### 3.3.1 Base-case 1D modelling and comparison to discharge data

Using base parameters in Table 3.2 to Table 3.6 and the full 1D model, we show agreement between simulated and experimental C/5 constant current discharge in Figure 3.1a. Experimental data is from the first discharge cycle of a proprietary, pre-commercial 19.5 Ah Li-S pouch cell. The C/5 discharge was performed using an Arbin high current battery cycler with cell temperature of 20°C. To account for some loss from the theoretical capacity, we found that assuming a utilization ratio of 0.952 gives a minimum root mean squared error between experimental and simulated data of 11mV. Using these parameters, we show how the discharge curve changes with C-rate in Figure 3.1b. Parameters were chosen such that there is a small reduction in discharge capacity with increasing C-rate, mainly due to diffusion limitations. Note that at lower C-rates, the

1D model is not able to solve at the end of discharge due to steep concentration gradients where the concentration variables approach zero and singularities occur. This numerical instability occurs due to diffusion limitations and can be resolved by using more stable techniques such as the tank model.[102]

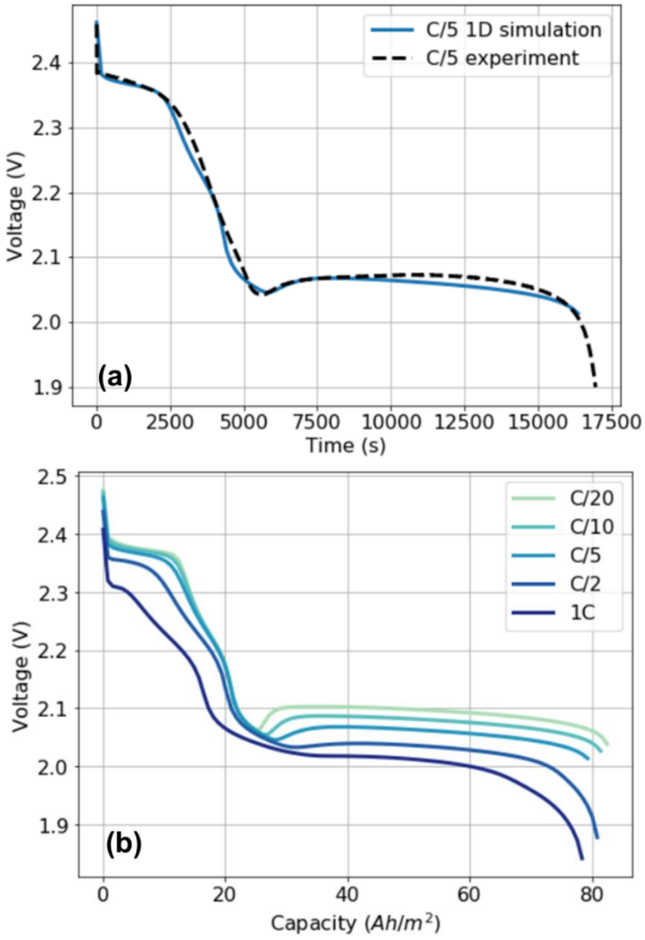

***Figure 3.1. (a) Voltage curves for C/5 discharge. Solid line is simulated data from a standard 1D full cell model. Dotted line is experimental data from a commercial cell. (b) Discharge voltage vs capacity curves at different C-rates; simulated using a standard 1D full cell model.***

The evolution of the solid sulfur phases in the lithium sulfur battery during a C/20 discharge can be described as having three regions as shown in Figure 3.2. In its fully charged state, the cell starts off containing mostly solid sulfur $S_8$. As the cell discharges, $S_8$ dissolves and reduces which corresponds to the first higher voltage plateau. In this first region, the only solid is $S_8$. In the second region, there is no solid sulfur species, only dissolved sulfur and polysulfides. The dissolved higher order polysulfides reduce to lower order polysulfides which corresponds to a drop in voltage as we move down the reaction cascade. Region three is defined by the presence of only the $Li_2S$ solid product. The voltage dip around 30% DOD in Figure 3.2 can be described by the presence of supersaturated $Li_2S$ and its nucleation overpotential. Once $Li_2S$ starts precipitating out, as observed by the increasing solid volume fraction (orange line in Figure 3.2), the voltage can be described by a voltage recovery and the following second plateau. Note that with increasing C-rates, region two, where there are no solids, disappears. At even higher C-rates, it is possible for both solid $S_8$ and $Li_2S$ to exist at the same time as studied by Ghaznavi and Chen.[101] The focus of this paper is the thermodynamic nature of LiS and hence we will look at low C-rate behavior.

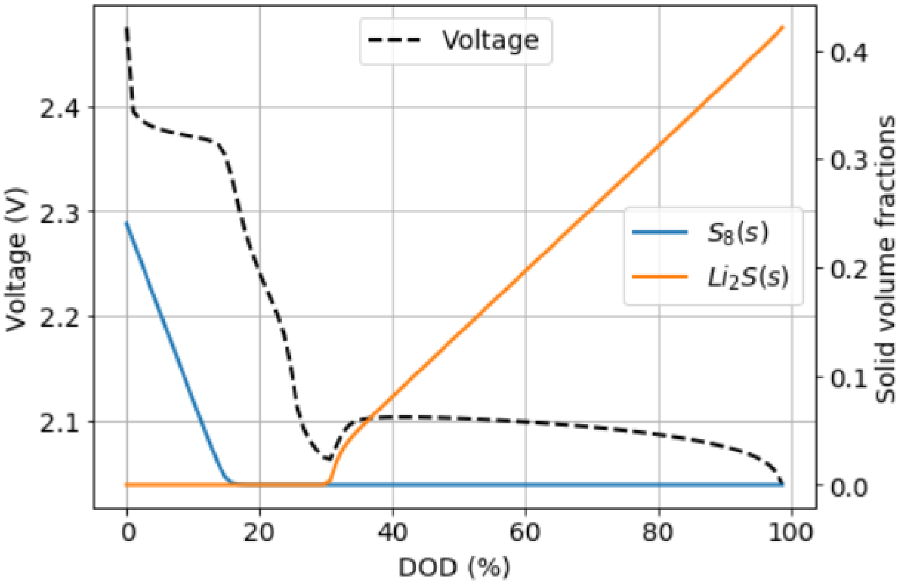

***Figure 3.2. Evolution of voltage and volume fractions of solids $S_8$ and $Li_2S$ during a C/20 discharge, simulated with a 1D full model. We can describe the discharge as having three regions: only $S_8(s)$ present, both solids present, and only $Li_2S(s)$ present.***

### 3.3.2 Thermodynamic behavior of LiS – comparing 1D full physics to 0D thermodynamic model

The thermodynamic behavior of an LiS cell can be obtained by simulating a GITT-like experiment using the 1D full model. We simulate a C/20 constant current discharge to various DODs and then set the current to zero, allowing the cell to relax full till the voltage has equilibrated. Examples of this relaxation simulation to various DODs can be visualized in Figure 3.3a. At low DODs (<20%

DOD), there is no voltage relaxation. At 30% DOD, we see the greatest voltage relaxation of ~75mV, with voltage relaxation decreasing to ~40mV at 90% DOD. At 26% DOD, we observe an interesting phenomenon where the voltage remains flat for five hours after the current has been turned off before relaxing to a higher voltage. This is probably due to the presence of $Li_2S$ solid with very slow precipitation kinetics. We repeated this relaxation simulation at every 2% DOD interval (+ in Figure 3.3b) across the entire discharge.

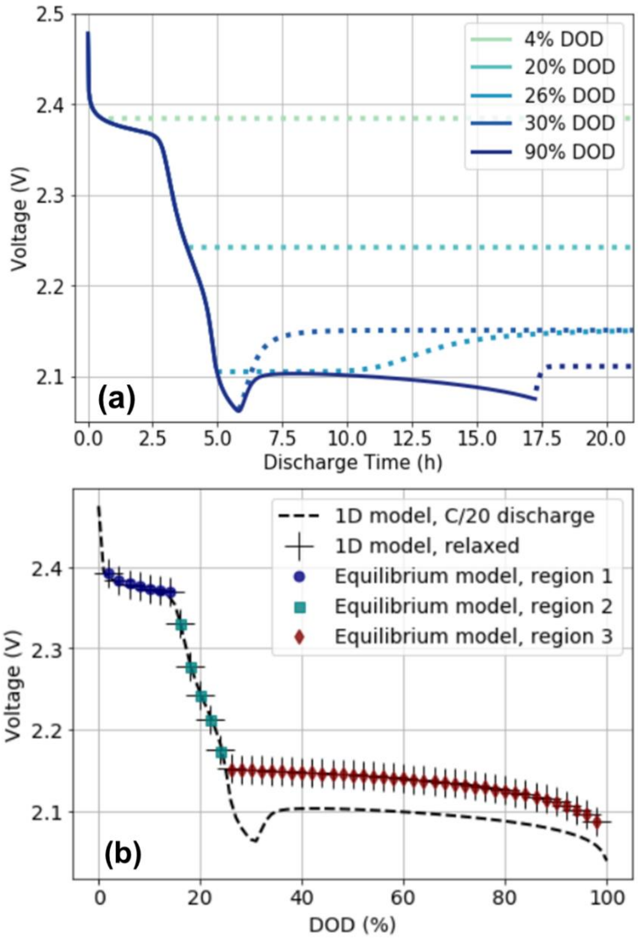

***Figure 3.3. (a) Simulated C/20 discharge to various DODs (solid line) and subsequent relaxation till voltage has equilibrated (dotted line). (b) Comparison of simulated C/20 discharge (dotted line) to relaxed voltages at each DOD. Relaxed voltages calculated using the 1D full model (black crosses) and using the thermodynamic equilibrium model in three regions (circle, square, diamond markers) are shown to converge.***

We also used a 0D thermodynamic model, solved in three separate regions, to obtain the same solution as the 1D full physics model (Figure 3.3b). Since both models converge to the same thermodynamic equilibrium voltage, we will use the 0D thermodynamic model to further analyze the thermodynamic behavior of the system. There is no noticeable voltage relaxation in the first two regions. For the third region, across the second voltage plateau, there is a noticeable 40-50mV difference between the thermodynamic equilibrium voltage and the slow C/20 discharge voltage. The magnitude of this voltage relaxation was chosen by adjusting the solubility product of $Li_2S(s)$, $Ksp_{Li2S}$. Experimental LiS literature show that there is a noticeable voltage relaxation in the second plateau ranging from 40-100mV (~75mV after a 20 hour relaxation following a C/10 current step on BASF pouch cells,[11] ~100mV following a C/20 GITT step on coin cells,[9] ~40mV after a 2h rest following a C/48 GITT step on Sion Power pouch cells[110]).

### 3.3.3 Effect of varying the solubility product, $Ksp_{Li2S}$

$Li_2S$ is known to be a very insoluble solid. However, review of the experimental literature shows no quantitative measurements of the solubility of $Li_2S$ in typical electrolytes. In the modeling literature, the value of $Ksp_{Li2S}$ is thus always explained as an assumed parameter to give the best fit for a discharge curve. Kumaresan et al. assumed a value of 3.0 x $10^{-5}$ $mol^3/m^9$,[29] while a selection of other authors with similar models have used values with orders of magnitude of $10^2$, $10^5$, and $10^7$ $mol^3/m^9$.[35,52,83] Ghaznavi and Chen found that the Kumaresan model (and its associated parameters) was unable to charge due to low saturation concentration.[50] By increasing the $Ksp_{Li2S}$ by seven orders of magnitude (from the assumed value of 9.95 x $10^{-4}$ $mol^3/m^9$), they were able to simulate charging at 0.02C.[51] This wide range of values for $Ksp_{Li2S}$ used demonstrates the insensitivity of a typical voltage discharge curve to $Ksp_{Li2S}$.

We illustrate this by decreasing $Ksp_{Li2S}$ by two orders of magnitude from the base value of 2.0 x $10^4$ $mol^3/m^9$ and observing no significant difference in the C/20 discharge curves in Figure 3.4a. All other parameters are kept constant. However, when the same two values of $Ksp_{Li2S}$ is used to simulate the thermodynamic behavior of the cell, there is a large shift in the second voltage plateau of ~70mV (Figure 3.4b). We vary $Ksp_{Li2S}$ over a range of $10^{-2}$ to $10^5$ and observe the corresponding change in equilibrium voltage at 30%, 60%, and 90% DOD. Since we can rewrite the Nernst equation expression for the reduction of $S_2^{2-}$ to $S^{2-}$ (reaction in Eq. (3.6)) by using the definition of the solubility product for $Li_2S$ (Eq. (3.21)),

$$\phi_1 = U_6^{\theta} - \frac{RT}{F}\left( -\frac{1}{2} ln\left[ \frac{C_{S_2^{2-}}}{1000} \right] + ln\left[ \frac{C_{S^{2-}}}{1000} \right] \right) \tag{3.28}$$

$$\phi_1 = U_6^{\theta} - \frac{RT}{F} \ln\left( \frac{Ksp_{Li_2S}}{C_{S_2^{2-}}{}^{\frac{1}{2}} C_{Li+}{}^{2} 1000^{\frac{1}{2}}} \right) \tag{3.29}$$

Figure 3.4c shows the approximately linear trend we expect of equilibrium voltage with $Ksp_{Li2S}$ on a log scale. The trend is only approximately linear as the concentrations of $Li^+$ and $S_2^{2-}$ do change with varying $Ksp_{Li2S}$ values. Over this same range of $Ksp_{Li2S}$ values, there is no change for the voltage discharge curve, thus emphasizing the usefulness of using GITT-like relaxation experiments to identify this important parameter, at least to within an order of magnitude range for modeling purposes. For example, Kumaresan et al.'s $Ksp_{Li2S}$ value of $10^{-5}$ $mol^3/m^9$ would result in an equilibrium voltage higher than ~2.35V in the second plateau (e.g. at 60% DOD) which is highly improbable and can easily be proven using a simple relaxation experiment. Achieving a baseline understanding of the thermodynamic behavior and parameters before building more complex physics models with many more kinetic and transport parameters will result in more accurate modeling.

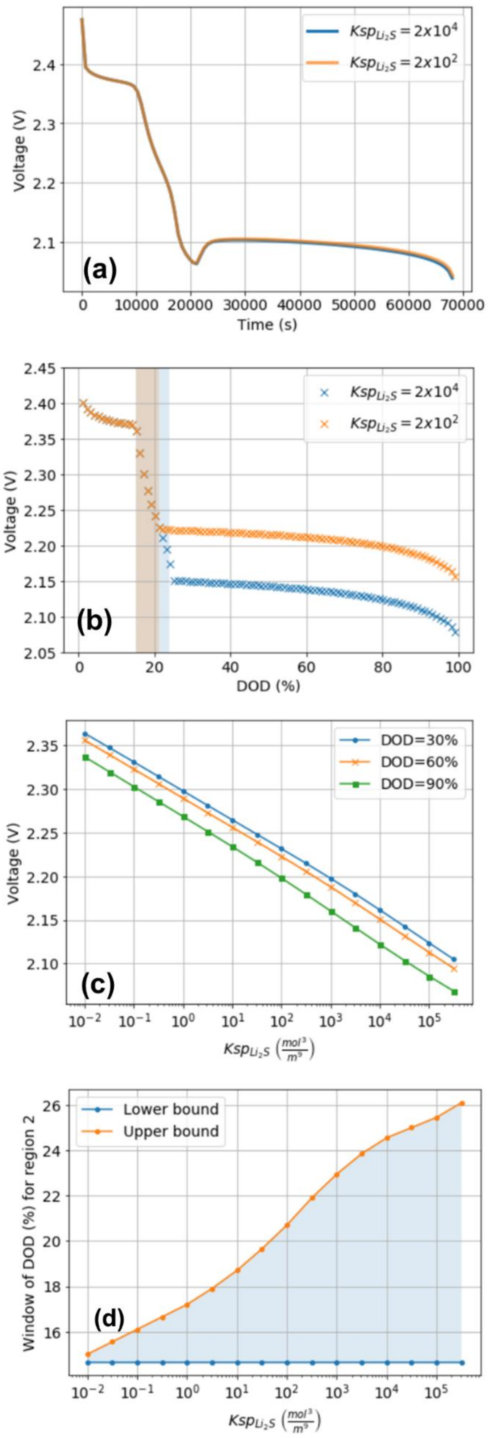

***Figure 3.4. Varying $Ksp_{Li_2S}$, from the base case value of 2x104 $mol^3/m^9$ to two orders of magnitude lower, has minimal effect on a (a) C/20 discharge with time, but significant effect on (b) relaxed voltages with DOD, especially in the second plateau. All other parameters are kept constant. (c) Relaxed voltages at various DODs, and (d) window of DOD for region 2, for different values of $Ksp_{Li_2S}$. Shaded areas in (b) and (d) represent region 2, where all sulfur species are soluble.***

From Figure 3.4b, notice that the lower bound of region 2 stays the same while the upper bound of region 2 increases as $Ksp_{Li2S}$ is increased. We show this trend for over a range of $Ksp_{Li2S}$ values in Figure 3.4d. This indicates that the $Ksp_{Li2S}$ is an important parameter for determining the window of DOD for region 2, the region where all sulfur species are soluble. The shaded areas in Figure 3.4b and d denotes the region where all sulfur species are soluble. Soluble sulfur species can be a problem for lithium sulfur cells as the dissolved polysulfides are able to diffuse to the anode side and are either reduced during charging or react with the strongly reducing lithium metal in the absence of a current, causing self-discharge. This phenomenon is known as shuttling and results in the loss of sulfur species when lower order polysulfides are reduced and precipitate out. They passivate the anode surface, and lead to increased cell resistance and loss in capacity of the cell over time. While there are several strategies such as structured cathodes[67] and separator coatings[111] to trap the polysulfides and retain them in the cathode, solvent engineering by using additives or selecting different combinations of solvents can help change the solubility of $Li_2S$ (and other insoluble polysulfide products). This can potentially narrow the window of DOD where polysulfides are soluble and reduce shuttling effects.

### 3.3.4 Effect of the $S_6^{2-}$ to $S_3^{\bullet-}$ dissociation chemical reaction and the reaction equilibrium constant, $K_{S3}$

Electrolyte engineering is also important for high energy LiS cells as polysulfides have different solubility and speciation in different solvents.[46] Low donor number solvents (e.g. tetrahydrofuran (THF)) favor dianions polysulfides such as $S_4^{2-}$ and $S_6^{2-}$ while high donor number solvents (e.g. dimethylacetamide (DMA)) favor free radicals such as $S_3^{\bullet-}$, which is identified by clear blue solutions.[112] Previous modeling work have included dissociation chemistry involving $S_3^{\bullet-}$ and $S_4^{\bullet-}$ [43,47] but reaction pathways that include a combination of chemical and electrochemical reactions, including dissociation and disproportionation chemistry and alternate pathways beyond the proposed reaction cascade is still up for debate.[39,40] A review by Wild et al. covers a wide spectrum of proposed reaction mechanisms that have been modeled or experimentally derived.[113]

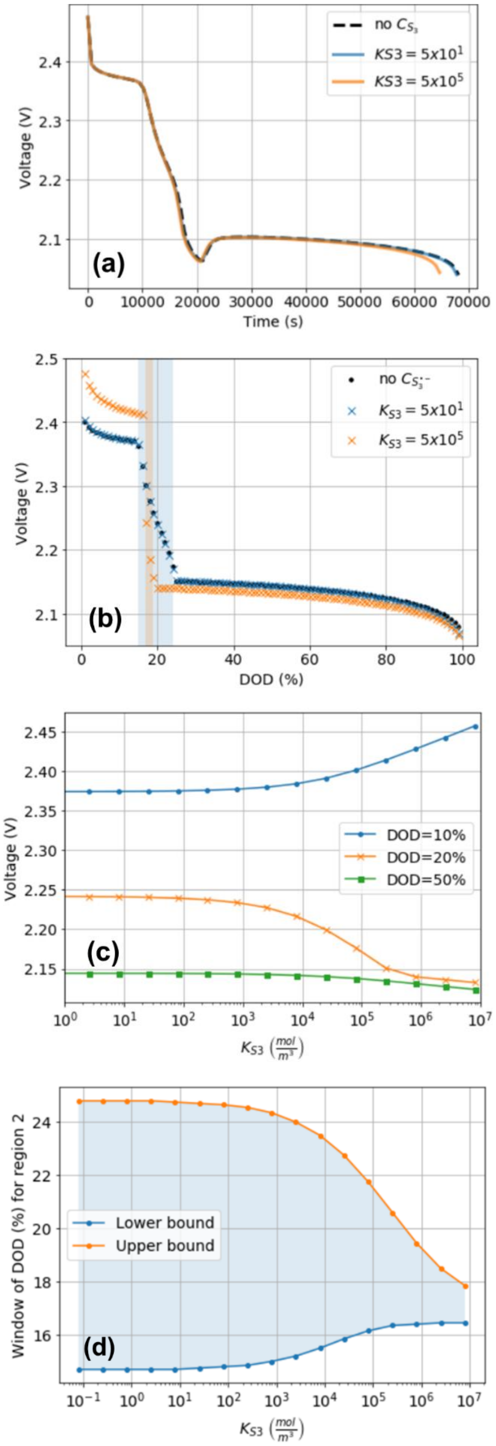

***Figure 3.5. Inclusion of the dissociation reaction, with*** $K_{S3}$ ***= 5x101*** $mol/m^3$ ***and*** $k_{f,S3}$ ***= 1x10-5 s-1, (blue line and markers) has minimal visible difference from the absence of the dissociation reaction (black line and markers) for (a) the C/20 discharge and (b) the thermodynamic equilibrium. Increasing the value of*** $K_{S3}$ ***by four orders of magnitude reduces the capacity for a (a) C/20 discharge by a small amount, while significantly shifting both plateaus for the (b)***

***relaxed voltages with DOD. All other parameters are kept constant. (c) Relaxed voltages at various DODs, and (d) window of DOD for region 2, for different values of $K_{S3}$. Shaded areas in (b) and (d) represent region 2, where all sulfur species are soluble.***

Here, we focus only on the addition of one homogeneous dissociation reaction that produces $S_3^{\bullet-}$, as written in Eq. (3.9), with the reaction equilibrium constant described by Eq. (3.10).

For the values of $K_{S3}$ = 5x10$^1$ $mol/m^3$ and $k_{f,S3}$ = 1x10$^{-5}$ s$^{-1}$, the simulated C/20 discharge curve is the same as that without the addition of this dissociation reaction (Figure 3.5a). Keeping the same value of $k_{f,S3}$, but increasing $K_{S3}$ by four orders of magnitude, the discharge curve in (Figure 3.5a is the same except for the very end of discharge where there is a small reduction in capacity at this higher value of $K_{S3}$. However, when we simulate the thermodynamic equilibrium voltage using the same two values of $K_{S3}$, there are noticeable differences shown in (Figure 3.5b. For $K_{S3}$ = 5x10$^5$ $mol/m^3$ compared to 5x10$^1$, the first voltage plateau is ~50mV higher, and the window of DOD for region 2 is smaller. For $K_{S3}$ = 5x10$^1$ $mol/m^3$, the thermodynamic voltage is the same as when the dissociation reaction was omitted.

Similarly, we can simulate the equilibrium voltage over a wide range of $K_{S3}$ = 1 to 10$^7$ $mol/m^3$ and track the equilibrium voltage at various DODs. (Figure 3.5c shows how the equilibrium voltages change over this range of $K_{S3}$ at 10%, 20%, and 50% DODs. Over this same range of $K_{S3}$ values, there is no change for the voltage discharge curve. For 10% DOD which is in region one (only $S_8$ solid), the equilibrium voltage increases with increasing $K_{S3}$ as production of $S_3^{\bullet-}$ is favored while concentration of $S_6^{2-}$ is reduced. The Nernst equations involving $S_6^{2-}$ are,

$$U_3 = U_3^{\theta} - \frac{RT}{F} ln\left( \frac{[S_6^{2-}]^2}{[S_8^{2-}]^{\frac{3}{2}}} \frac{1000^{3/2}}{1000^2} \right) \tag{3.30}$$

$$U_4 = U_4^\theta - \frac{RT}{F} ln\left( \frac{[S_4^{2-}]^{\frac{3}{2}}}{[S_6^{2-}]} \frac{1000}{1000^{3/2}} \right) \tag{3.31}$$

Since the first voltage plateau can be mostly attributed to reduction of higher order polysulfides reactions (Eq. (3.2) and (3.3)), according to Eq. (3.30), a reduction in $[S_6^{2-}]$ would correspond to an increase in equilibrium voltage $U_3$. On the other hand, the trend seen at the later DODs of 20% and 50% can be described in part by Eq. (3.31) where a reduction in $[S_6^{2-}]$ would correspond to a decrease in equilibrium voltage $U_4$. The effect of $K_{S3}$ on the equilibrium voltage of the second plateau is significantly smaller than the effect of $Ksp_{Li2S}$ described in the previous section. Also, note that at DOD=20%, there is a steep drop in equilibrium voltage as $K_{S3}$ increases, as DOD=20% initially starts out in region two (no solids) and later, with greater $K_{S3}$, is part of region three (only $Li_2S$ solid).

$K_{S3}$ also influences the window width of DOD for region two, the region containing only dissolved polysulfides. (Figure 3.5d shows that increasing the value of $K_{S3}$ increases the lower bound and decreases the upper bound, effectively narrowing the window of region two. Again, this highlights the importance of solvent engineering as it not only affects the solubility of polysulfides but also here, the speciation, which subsequently affects the window of solubility. A smaller window where polysulfides are soluble will help alleviate the shuttling effect that is a challenge for viable long-lasting commercial LiS cells.

### 3.3.5 Kinetics of the $S_6^{2-}$ to $S_3^{\bullet-}$ dissociation chemical reaction

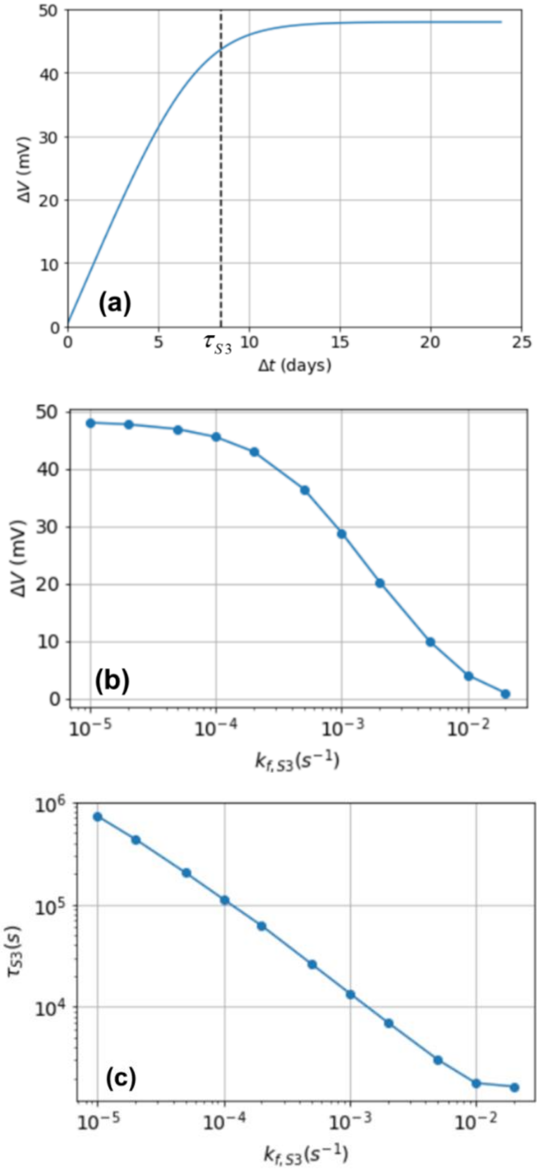

***Figure 3.6. (a) Transient voltage relaxation after C/20 discharge to 10% DOD for*** $K_{S3}$ ***= 5x105*** $mol/m^3$ ***and*** $k_{f,S3}$ ***= 1x10-5 s-1.*** $\Delta V$ ***and*** $\Delta t$ ***are the difference in voltage and time values from when the current is turned off. The knee point, representative of the characteristic time*** $\tau_{S3}$ ***, is 8.45 days. (b) Magnitude of voltage relaxation,*** $\Delta V$ ***, decreases as*** $k_{f,S3}$ ***increases at 10% DOD. (c) Proportional relationship between log(***$k_{f,S3}$***) and the measurable value log(***$\tau_{S3}$***) at 10% DOD.***

The rate constant of the $S_6^{2-}$ dissociation reaction, $k_{f,S3}$, is written as a forward rate constant and added to the 1D full model as Eq. (3.22) and (3.23). $k_{f,S3}$ = 1x10$^{-5}$ s$^{-1}$ was used in the above simulations. Beyond thermodynamics of the system, we can also look at the transient relaxation voltage to get kinetic information. Figure 3.6a shows the voltage relaxation, $\Delta V$, following a C/20 discharge to 10% DOD. This plot is scaled to start at zero for both the time and voltage axis, only showing the difference in value ($\Delta t$, $\Delta V$) from the moment the current is turned off. The relaxation voltage is almost 50mV over the time constant, $\tau_{S3}$, of 8.45 days. This value is found by taking the knee point calculated using the kneed python package based an algorithm that calculates the maxima of the difference curve.[114] $\tau_{S3}$ is large due to the slow forward reaction rate of the dissociation reaction chosen here. The relationships of $\Delta V$ and $\tau_{S3}$ as functions of $k_{f,S3}$ are plotted in Figure 3.6b and 6c respectively, for a given value of $K_{S3}$ = 5x10$^{1}$ $mol/m^3$ and at 10% DOD. As $k_{f,S3}$ increases, $S_6^{2-}$ dissociates quicker and the reaction reaches equilibrium faster, hence the voltage would be nearer to equilibrium the moment the current is turned off. Consequently, both the $\Delta V$ and $\tau_{S3}$ are smaller when $k_{f,S3}$ is larger. Also, there is a proportional relationship between log($k_{f,S3}$) and the measurable value log($\tau_{S3}$) as the time constant can be defined as $\tau_{S3} \sim \frac{1}{k_{f,S3}}$.

Lastly, we show the complexity of the LiS cell for this dissociation chemistry by demonstrating how the relaxation voltage can vary with both $k_{f,S3}$ and $K_{S3}$ at 10% DOD in Figure 3.7. Thermodynamic equilibrium voltages and relaxation transient experiments can give more information than and differ from a slow discharge curve at low reaction rates and high reaction equilibrium constants. Through this analysis, we show how a GITT-like relaxation experiment can give order of magnitude information regarding both thermodynamic and kinetic parameters of dissociation chemistry of an LiS cell. We only explored this particular $S_6^{2-}$ to $S_3^{\bullet -}$ dissociation chemistry here but similar effects are expected for $S_8^{2-}$ to $S_4^{\bullet -}$ or other dissociation chemistries, where effects may vary at different DODs depending on where in the reduction cascade the reaction occurs.

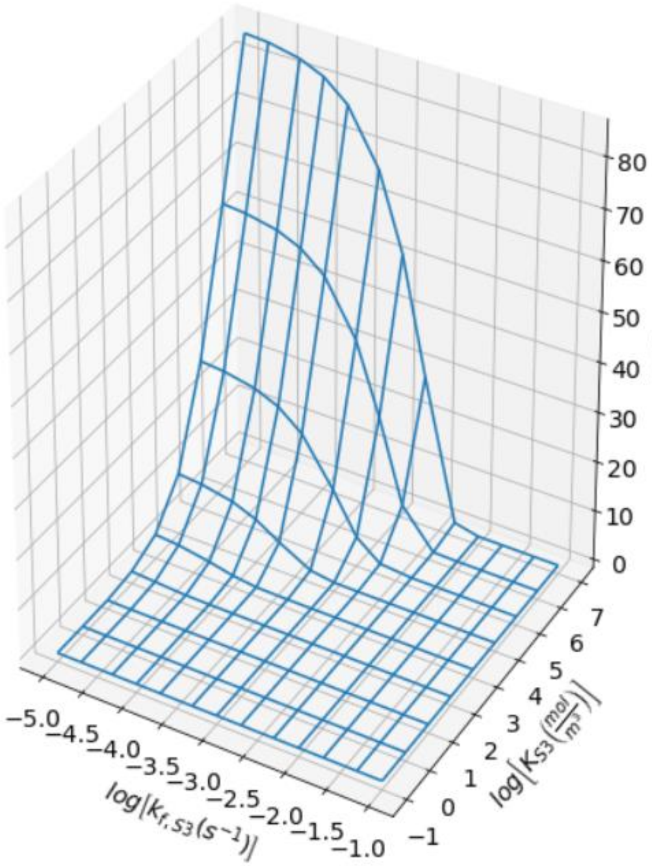

***Figure 3.7. 3D plot showing the variation in relaxation voltage, $\Delta V$, with $k_{f,S3}$ and $K_{S3}$, at 10% DOD.***

## 3.4 Conclusions

In this work, we show that using parameters from the modeling literature, with slight adjustments, we can fit the 1D full physics model to experimental pouch cell discharge data. However, discharge data does not give us all the information we need. Using reasonable parameters and through cell-level simulations, we show the significance of using GITT-like relaxation experiments to get extra information such as the thermodynamic equilibrium voltages and transient relaxation data. We also came up an alternate method to get the equilibrium voltages with a new model that only contains fundamental Nernstian and precipitation thermodynamic equations. We introduce the idea of three main regions to describe the thermodynamics of the LiS system over the entire SOC range – containing only $S_8$ solid, no solids, and only $Li_2S$ solid.

Using this concept, we explored the effects of varying the solubility product of $Li_2S$ and highlight the importance of the $Ksp_{Li2S}$ parameter, how the discharge curve can be insensitive to it, and how a relaxation experiment can provide order of magnitude information about this parameter. We also looked at the effects of adding $S_6^{2-}$ to $S_3^{\bullet-}$ dissociation chemistry to the models and how GITT-like relaxation experiments can extract information about the reaction equilibrium constant and rate constant that a standard discharge curve might not be able to.

The analysis in this paper demonstrates how a GITT-like relaxation experiment, a relatively simple electrochemical measurement technique, can give valuable information about thermodynamic and kinetic parameters that can be helpful for building more accurate models. Such parameters can defer greatly depending on the choice of solvent of the cell as different solvents can vary the speciation and solubility of polysulfides.[46] For cross-referencing purposes, thermodynamic solubility and reaction equilibrium parameters can also be obtained through quantum chemical calculations of solvation enthalpies and energetics of dissociation reactions.[115] It is also worth noting that varying the thermodynamic parameters, $Ksp_{Li2S}$ and $K_{S3}$, can change the window of DOD where all polysulfides are soluble. Narrowing this window through solvent engineering might alleviate the shuttling problem but there is also consideration to be made for the low electronic conductivity of the cell due to the insulating solids.

List of Symbols

| | |
|---|---|
| $a$ | *Specific surface area of cathode,* $m^2/m^3$ |
| $a_0$ | *Initial value of a,* $m^2/m^3$ |
| *brug* | *Bruggeman coefficient* |
| $C_{i,ref}$ | *Reference concentration of species i,* $mol/m^3$ |
| $C_i$ | *Concentration of species i,* $mol/m^3$ |
| $D_{0,i}$ | *Diffusion coefficient of species i in the bulk medium,* $m^2/s$ |
| $D_{eff,i}$ | *Effective diffusion coefficient of species i in the porous medium,* $m^2/s$ |
| $F$ | *Faraday constant, C/mol* |
| $i_{0,j}$ | *Exchange current density of reaction j,* $A/m^2$ |
| $i_{app}$ | *Applied current density,* $A/m^2$ |
| $i_j$ | *Current density from reaction j,* $A/m^2$ |
| $i_1$ | *Superficial current density in the solid phase,* $A/m^2$ |
| $i_2$ | *Superficial current density in the electrolyte phase,* $A/m^2$ |
| $k_{f,S3}$ | *Rate of the forward reaction for the dissociation chemistry,* $s^{-1}$ |
| $k_{b,S3}$ | *Rate of the backward reaction for the dissociation chemistry,* $m^3mol^{-1}s^{-1}$ |
| $k_j$ | *Rate constant of electrochemical reaction j,* $\left(\frac{A}{m^2}\left[\frac{m^3}{mol}\right]^{\alpha p_{i,j}+(1-\alpha)q_{i,j}}\right)$ |
| $k_k$ | *Rate constant of precipitate k, varying units, see* Table 3.6 |
| $Ksp_k$ | *Solubility product of precipitate k, varying units, see* Table 3.6 |
| $K_{S3}$ | *Equilibrium reaction rate for the dissociation chemistry,* $mol/m^3$ |
| $L_{cat}$ | *Thickness of the cathode, m* |
| $L_{sep}$ | *Thickness of the separator, m* |
| $N_i$ | *Superficial flux of species i, mol* $m^2$ $s^{-1}$ |
| $n_j$ | *Number of electrons transferred in electrochemical reaction j* |

| | |
|---|---|
| $q_{i,j}$ | $p_{i,j} = s_{i,j}$ for anodic or reduced species |
| $p_{i,j}$ | $q_{i,j} = -s_{i,j}$ for cathodic or oxidized species |
| $R$ | *Gas constant, J mol$^{-1}$ K$^{-1}$* |
| $r_i$ | *Production rate of species i from electrochemical reactions, mol m$^{3}$ s$^{-1}$* |
| $R'_k$ | *Rate of precipitation of solid species k, mol m$^{3}$ s$^{-1}$* |
| $R_i$ | *Production rate of species i due to precipitation reactions, mol m$^{3}$ s$^{-1}$* |
| $s_{a,j}$ | *Stoichiometric coefficient of anodic species in electrochemical j* |
| $s_{c,j}$ | *Stoichiometric coefficient of cathodic species in electrochemical j* |
| $s_{i,j}$ | *Stoichiometric coefficient of species i in electrochemical reaction j* |
| $S_{bal}$ | *Total number of moles of sulfur atoms per cross-sectional area, units mol/m$^{2}$* |
| $T$ | *Temperature, K* |
| $t$ | *Time, s* |
| $U_j^{\theta}$ | *Standard Open Circuit Potential (OCP) of electrochemical reaction j, V* |
| $U_j$ | *OCP of electrochemical reaction j, V* |
| $\tilde{V}_k$ | *Molar volume of the precipitate k, m$^{3}$/mol* |
| $z_i$ | *Charge number of species i* |

*Greek symbols*

| | |
|---|---|
| $\alpha$ | *Charge transfer coefficient* |
| $\gamma_{i,k}$ | *Number of ionic species i produced by the dissociation of precipitate k* |
| $\varepsilon_c$ | *Porosity of cathode* |
| $\varepsilon_s$ | *Porosity of separator* |
| $\varepsilon_k$ | *Volume fraction of precipitate k* |

|  |  |
|---|---|
| $\eta_j$ | *Overpotential for electrochemical reaction j* |
| $\xi$ | *Morphology parameter* |
| $\sigma$ | *Conductivity of solid phase of the cathode material, S/m* |
| $\sigma_{eff}$ | *Effective conductivity of solid phase of the porous cathode, S/m* |
| $\phi_1$ | *Potential in the solid phase, V* |
| $\phi_2$ | *Potential in the liquid phase, V* |

Subscripts

|  |  |
|---|---|
| *c* | In region of the cathode |
| *s* | In region of the separator |

# Chapter 4: EIS Modeling of Lithium Sulfur Batteries

## 4.1 Introduction

### *Motivation*

To accelerate development of lithium sulfur technology, EIS measurements can be used to characterize electrochemical processes occurring in the system by timescale and give insight on the evolution of mechanisms as the cell degrades.[21] The development of physics-based models that incorporate mechanisms and pathways can help us understand and accelerate design of the system. Applying such models to the frequency domain can give us detailed insight on proposed mechanisms and processes that are not available on the timescale of a charge/discharge. Comparing simulated EIS spectra to experimental measurements can be valuable in showing which features can and cannot be captured by the mechanisms in existing models and lead to the development of more comprehensive models.

### *Review of experimental lithium sulfur EIS measurements*

Experimentalists working on solutions to limit polysulfide shuttling, such as using coated separators[96] or electrolyte additives to protect the lithium anode,[116] typically use EIS to show improvement in cell performance by means of an impedance of smaller magnitude. More detailed impedance studies that aim to elucidate specific physical process from EIS spectra have also been carried out but there remains to be a solid consensus on which processes contribute to the features in an EIS spectra.

Deng et al. aimed to explain the two semicircle features of lithium sulfur cells with a combination of EIS measurements across SOCs and temperatures. They attributed the high frequency semicircle to interphase electronic contact between particles across the entire electrode, and the lower frequency semicircle to charge transfer. Using fitted ECMs, they showed the trend of increasing charge transfer resistance with cycling (and attributed this to insulated low order polysulfide products forming on the cathode surface), while the electrolyte resistance and interphase resistance did not increase significantly. However, they dismissed the contribution of the anode to the EIS completely.[97]

On the other hand, Walus et al. used symmetric cell experiments to decouple the electrodes' contributions to the overall full cell impedance. The lithium anode greatly dominated behavior in the middle frequency kinetic regime while the low frequency tail is generally dictated by insulating sulfur. This impedance at low frequency decreases during self-discharge as solid sulfur $S_8$ dissolves. The self-discharge behavior at longer timescales (>25h) is almost entirely attributed to an increase in thickness of the passivation layer on the lithium metal anode from electrolyte decomposition under storage.[99]

For purposes of our modeling, we will start by modeling the anode in a perfectly stationary protected state. The eventual goal is to see if experimental trends and features can be described by a simple model before adding more complicated physics to capture the physical processes hypothesized by the studies above.

### *Lithium sulfur physics-based impedance models*

There has not been a detailed analysis of the impedance of lithium sulfur batteries using physics-based models. Time domain physics-based models for lithium sulfur have been developed with mechanisms of the reaction cascade and precipitation reactions, allowing for a deeper understanding of internal states of the battery such as concentrations of various species and local overpotentials.[29] Such models are able to capture voltage curves well during discharge.

Fronczek and Bessler [100] have simulated EIS spectra based on similar mechanisms in the widely accepted one-dimensional model developed by Kumaresan et al..[29] They are the first to demonstrate the ability to do so with a physics-based modeling approach using a potential step in the time domain and performing FFT on the current relaxation to obtain the impedance. Their simulated spectra do not match experimental trends with SOC and no detailed explanation or exploration of the spectra has been done. Note that a potential step is one directional and we instead aim to perturb the system with a sinusoidal modulation. Our aim is also to leverage the ability of physics-based impedance models for lithium sulfur to explore the parameter space and time constants in a systematic manner.

*Chemistry*

The five electrochemical reactions being modeled are,

$$\frac{1}{2}S_{8(l)} + \mathrm{e}^- \rightleftharpoons \frac{1}{2}S_8^{2-} \tag{1}$$

$$\frac{3}{2}S_8^{2-} + \mathrm{e}^- \rightleftharpoons 2S_6^{2-} \tag{2}$$

$$S_6^{2-} + \mathrm{e}^- \rightleftharpoons \frac{3}{2}S_4^{2-} \tag{3}$$

$$\frac{1}{2}S_4^{2-} + \mathrm{e}^- \rightleftharpoons S_2^{2-} \tag{4}$$

$$\frac{1}{2}S_2^{2-} + \mathrm{e}^- \rightleftharpoons S^{2-} \tag{5}$$

The dissolution and precipitation reactions are:

$$S_{8(l)} \rightleftharpoons S_{8(s)} \tag{6}$$

$$2Li^+ + S^{2-} \rightleftharpoons Li_2S_{(s)} \tag{7}$$

## 4.2 Methods

This impedance simulated in this work is of a lithium sulfur cathode half-cell. Two models are used – a 1D model that contains thermodynamics, kinetics, and transport, and a 0D model that contains only thermodynamics and kinetics. The governing equations of these time domain models are adapted from others in the literature and are described below. In this work, as far as we know, we are the first to transform these two models into the frequency domain and solve for the impedance.

### 4.2.1 Governing equations for 1D detailed physics model (thermodynamics + kinetics + transport)

The 1D model is based on equations developed by Kumaresan et al.[29], with the same modifications made in Chapter 3, with a noteworthy deviation being that only the cathode half-cell is modeled here without the separator or anode; thus, the boundary conditions at the cathode/current collector interface ($x=L_{cat}$) remains the same but the boundary conditions at the separator/cathode interface (now x=0), are modified to:

- Flux of $Li^+$,

$$N_{Li^+} = -i_{app} / F \text{ at x=0} \tag{4.8}$$

  where $i_{app}$ is the applied current density with unit $A/m^2$ and is defined as negative during discharge. The anode, not modeled here, is assumed to be a perfectly protected Li foil supplying $Li^+$ ions that enter the cathode

- Flux for all other species are zero.

$$N_i = 0 \;\; for \;\; i = S_{8(l)}, S_8^{2-}, S_6^{2-}, S_4^{2-}, S_2^{2-}, S^{2-}, A^- \text{ at x=0} \tag{4.9}$$

- Solution phase potential is set as a reference to zero,

$$\phi_e = 0 \text{ at x=0} \tag{4.10}$$

- Solid phase current is zero,

$$i_s = 0 \text{ at x=0} \tag{4.11}$$

Also, a double layer capacitance charging term, $C_{dl}$, is added at the solid-electrolyte interface in the overall current balance equation. $Li_2S$ is the only solid product considered as there is still debate on the presence of precipitates.[33,35,36] **Table 4.1** contains all the governing equations, boundary conditions, and other expressions used.

***Table 4.1 Equations for 1D lithium sulfur cathode***

| Governing Equations | Boundary Conditions |
|---|---|
| Positive Electrode | |
| $\frac{\partial \varepsilon_c C_i}{\partial t} = -\frac{\partial N_i}{\partial x} + r_i - R_i$ | $N_{Li^+}\Big\vert_{x=0} = -\frac{i_{app}}{F},\ N_i\Big\vert_{x=0} = 0$ |
| $N_i = -D_{eff,i}\frac{\partial C_i}{\partial x} - z_i \frac{D_{eff,i}}{RT} F C_i \frac{\partial \phi_e}{\partial x}$ | $i_s\Big\vert_{x=0} = 0$ |
| $i_s + i_e = -i_{app}$ | $\phi_e\Big\vert_{x=0} = 0$ |
| $-\frac{\partial i_s}{\partial x} = a\sum_j i_j + aC_{dl}\frac{\partial(\phi_s - \phi_e)}{\partial t}$ | $0 = N_i\Big\vert_{x=L_{cat}}$ |
| $\frac{\partial \varepsilon_k}{\partial t} = \tilde{V}_k R'_k$ | $-i_{app} = i_s\Big\vert_{x=L_{cat}}$ |
| $\frac{\partial \varepsilon_c}{\partial t} = -\sum_k \tilde{V}_k R'_k$ | $0 = i_e\Big\vert_{x=L_{cat}}$ |
| Other Expressions | |
| $r_i = -a\sum_j \frac{s_{i,j} i_j}{n_j F}$ | $a = a_0\left(\frac{\varepsilon}{1-\varepsilon_{S_8,init} - efc}\right)^{\xi}$ |
| $i_s = -\sigma\frac{\partial \phi_1}{\partial x}$ | $i_e = F\sum_i z_i N_i$ |
| $\eta_j = \phi_s - \phi_e - U_j$ | $U_j = U_j^{\theta} - \frac{RT}{n_j F}\left(\sum_i s_{i,j} ln\left[\frac{C_i}{1000}\right]\right)$ |
| $D_{eff,i} = \varepsilon^{brug} D_{0,i}$ | $\sigma_{eff} = \sigma(1-\epsilon_c)^{brug}$ |
| $R_i = \sum_k \gamma_{i,k} R'_k$ | $R'_k = k_k \varepsilon_k\left(\prod_i C_i^{\gamma_{i,k}} - K_{sp,k}\right)$ |
| $i_j = k_j \prod_{i=red} C_i^{\alpha p_{i,j}} \prod_{i=ox} C_i^{(1-\alpha) q_{i,j}}\left[e^{\frac{(1-\alpha) n_j F}{RT}\eta_j} - e^{\frac{-\alpha n_j F}{RT}\eta_j}\right]$ | |

### 4.2.2 Governing equations for a 0D thermodynamics-kinetics model

The governing equations for the 0D model are adapted from equations of the full 1D model by eliminating spatial variation. We take the cathode to be a point, hence spatial dependence is eliminated, along with all fluxes. This is similar to Zhang et al.'s lumped model.[35] The equations are summarized in **Table 4.2** with some important details below:

- Mass balance of $Li^+$ ion includes flux from the Li foil, corresponding to applied current

$$\frac{\partial \varepsilon_c C_i}{\partial t} = -\frac{i_{app}}{F\,L_{cat}} + r_i - R_i \quad for \;\; i = Li^+ \tag{4.12}$$

- Sum of all faradaic currents, $i_j$, is equivalent to total applied current density

$$\frac{i_{app}}{L_{cat}} = a\sum_j i_j \tag{4.13}$$

- Solution potential $\phi_e$ is set as a reference to be zero

For both 0D and 1D models, we set the C-rate based on theoretical capacity of initial solid sulfur in the cathode, where each $S_8$ gives up 16 electrons when reduced to $S^{2-}$.

$$i_{app} = \frac{16 F L_{cat} \varepsilon_{S_{8,init}}}{3600 \tilde{V}_{S_8}} Crate \tag{4.14}$$

***Table 4.2 Equations for 0-D thermodynamics-kinetics lithium sulfur model***

| Governing Equations |
|---|
| Positive Electrode |
| $\frac{\partial \varepsilon_c C_i}{\partial t} = -\frac{i_{app}}{F\,L_{cat}} + r_i - R_i \quad for \;\; i = Li^+$ |
| $\frac{\partial \varepsilon_c C_i}{\partial t} = r_i - R_i \quad for \;\; i = S_{8(l)}, S_8^{2-}, S_6^{2-}, S_4^{2-}, S_2^{2-}, S^{2-}$ |
| $\phi_e = 0$ |
| $\frac{i_{app}}{L_{cat}} = a\sum_j i_j + aC_{dl}\frac{\partial(\phi_s - \phi_e)}{\partial t}$ |
| $\frac{\partial \varepsilon_k}{\partial t} = \tilde{V}_k R'_k$ |
| $\frac{\partial \varepsilon_c}{\partial t} = -\sum_k \tilde{V}_k R'_k$ |

### 4.2.3 Frequency domain impedance equations

For both the 1D and 0D time domain models described above, we transform the governing equations, boundary, and initial conditions to the frequency domain by writing all variables as the sum of a steady state DC component and a small perturbation term, similar to porous electrode impedance models of lithium-ion batteries.[5]

$$X(x,t;\omega,\Delta I) = X_0(x,t) + X_1(x;\omega,\Delta I) * \mathrm{Re}\{\exp(j\omega t)\} \tag{4.15}$$

We perform a Taylor expansion on all nonlinear expressions and gather all first order terms in the governing equations for linear impedance (higher order nonlinear quadratic terms are ignored as small). See Appendix II for an example. We then solve for all the real $X_1^{'}$ and imaginary $X_1^{''}$ first order terms.

The impedance equations also contain the mean steady-state variables, $X_0$, as constants that change with SOC. To simulate EIS spectra at different SOCs, the model takes the mean steady-state concentrations, potentials, and porosities as inputs. These values, as a function of SOC, are obtained using the thermodynamic equilibria model developed in Chapter 3. All parameters are the same as the base parameters used in Chapter 3.

### 4.2.4 Computational methods

For the 1D model, consistent with previous numerical methods applied,[19,117] we apply coordinate transformation in the region followed by orthogonal collocation with Legendre polynomials to discretize the partial differential equations in *x*, choosing 35 collocation points to ensure convergence (<1% relative difference with 30 points). However, for high frequencies for DODs at the ends (1% and 99% DODs), solutions are not well-converged and more collocation points need to be used. More work will be done to improve this. For both the 0D and 1D impedance models, the set of algebraic equations are then solved in *Maple 2018* using an in-house sparse Newton method solver with *Maple*'s *LinearAlgebra LinearSolve* command.

## 4.3 Results and Discussion

*Comparing 0D and 1D models*

A standard C/5 discharge is simulated using both time domain models and compared to experimental data. We can see in Figure 4.1 that both simulated discharge curves match experimental data well and there are very minor differences between the two simulated curves. This shows the limited impact of transport in these models at this C-rate. At higher C-rates, there is more of a difference between the 1D model with transport and the 0D model without transport, as shown in Figure 4.2.

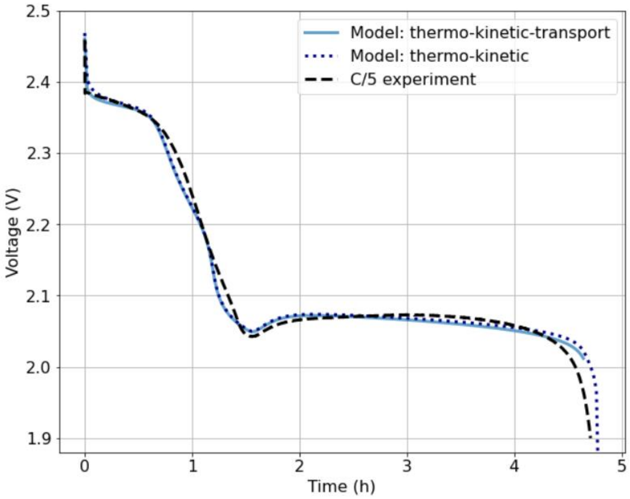

***Figure 4.1 Comparison of experimental data to models***

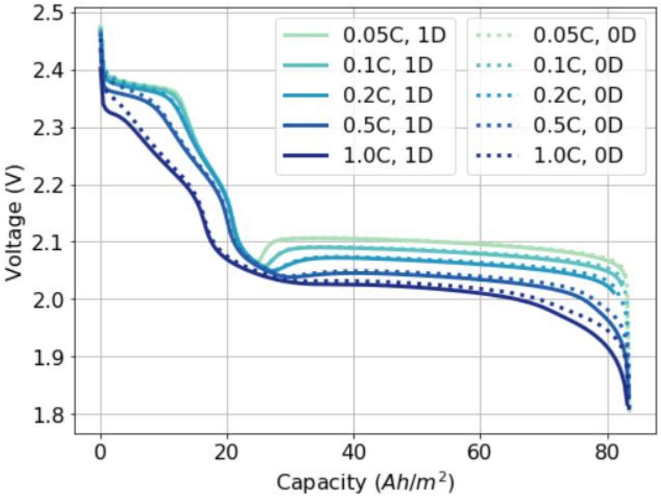

***Figure 4.2 C-rate study of discharge curves for 0D and 1D models***

Note that there is greater difference in these two models when we include the separator, as opposed to the cathode only shown here. This is because the 1D thermo-kinetic-transport model is able to simulate the diffusion limitations in the separator and shows a reduction in capacity with higher C-rates, which is a key trait seen experimentally. In this work, we will focus on the cathode half-cell only. Since transport is not a significant factor, we will start by looking at kinetics and thermodynamics that can be seen using EIS by using the 0D thermo-kinetic model.

### *Impedance simulations at high and low frequencies*

Figure 4.3 shows a Nyquist plot of an impedance simulation at 50% DOD. There are two semicircles, a large one at low frequencies and a much smaller one (zoomed in, left figure) at higher frequencies. Depending on the DOD, the high frequency semicircle can be 3-5 orders of magnitude smaller than that at low frequencies for our parameter set. This is indicative of charge transfer kinetics of at least two different timescales – one at a low rate, and the other at a high rate. This could be due to the multiple species and reactions. There is also a purely imaginary tail at low frequency that is reflective of chemical capacitance of the cathode.

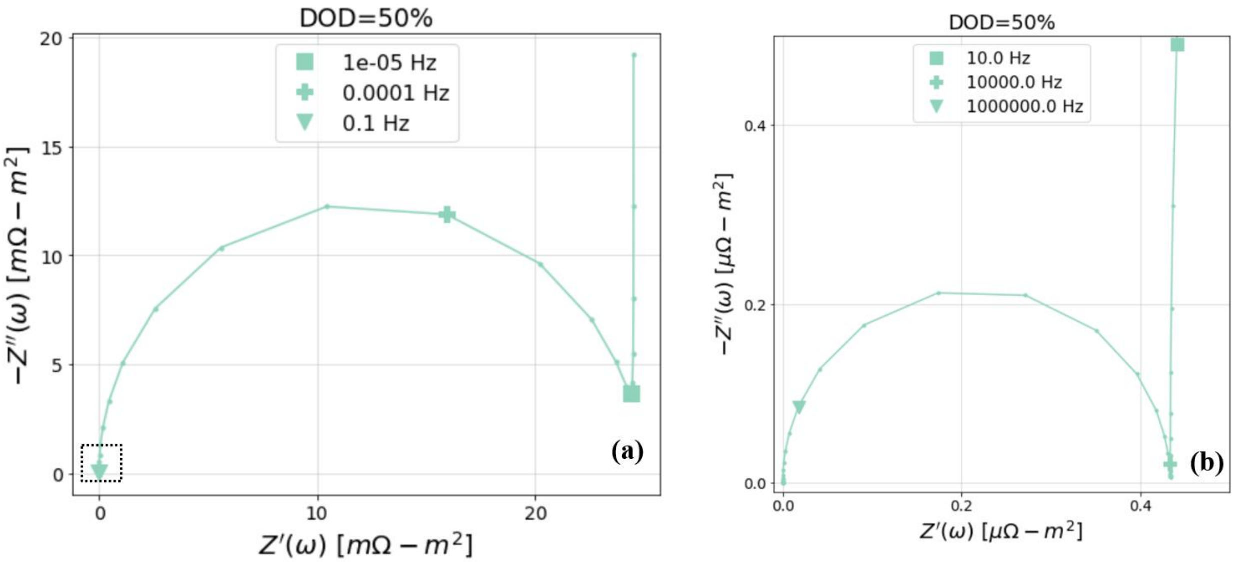

***Figure 4.3 Nyquist plot at (a) low and (b) high frequencies for DOD=50%, simulated with the 0D thermo-kinetic model. The boxed area in (a) is magnified and shown in (b). Note the difference in the units of the axes of (a) and (b).***

We can also elucidate the importance of each kinetic parameter matter by varying them. There are seven kinetic parameters – five electrochemical and two chemical precipitation reactions. We can explore which kinetic reactions govern the impedance at different frequencies and at different states of the cell.

At low frequencies, the Nyquist plots show a large semicircle of high impedance which are governed by different kinetics reactions based on the DOD of the cell. At 5% DOD, when there is significant amounts of $S_8(s)$ in the cathode, this large semicircle is only sensitive to two parameters, $k_{f,S8}$ and $i_{0,1}$, which correspond to Reactions (6) and (1). Both reactions are dependent on the concentration of $S_8(l)$. We show this in Figure 4.4a as deviations from the base case. In Figure 4.4b, at 50% DOD, where the cathode has significant amounts of $Li_2S(s)$ formed, the large semicircle is only sensitive to two different kinetic parameters, $k_{f,Li2S}$ and $i_{0,5}$, which correspond to Reactions (7) and (5). Both these reactions are dependent on the concentration of $S^{2-}$. Thus, the low frequency behavior can be said to be closely tied to the solid species present.

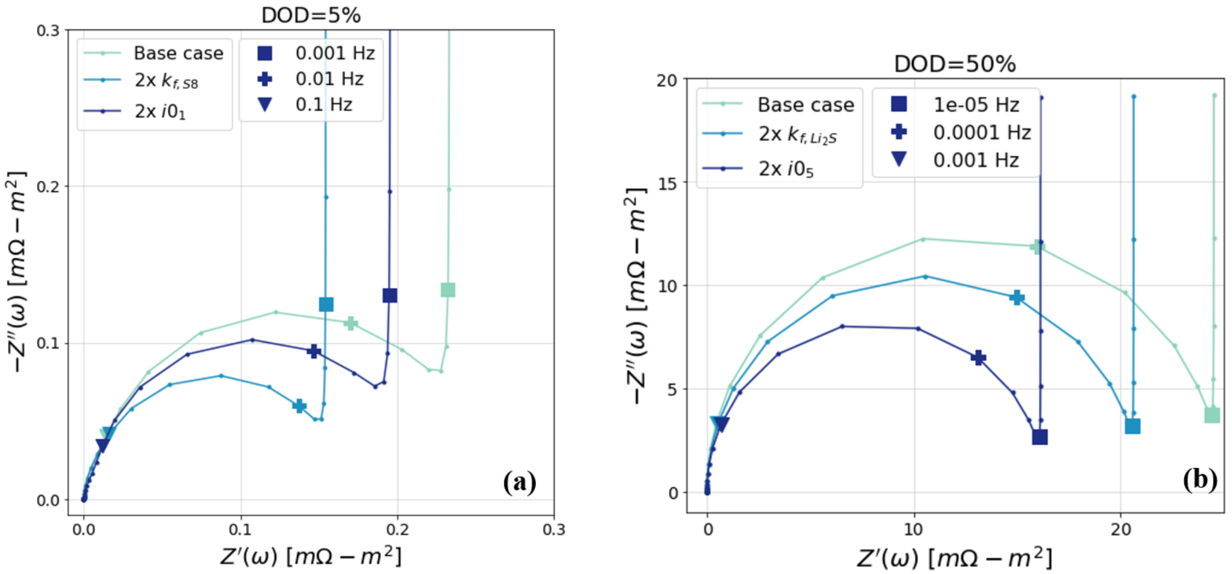

***Figure 4.4 Nyquist plots at low frequencies for (a) 5% DOD and (b) 50% DOD with varying kinetic parameters***

Processes occurring at lower frequencies are much slower with larger time constants, typically thermodynamic and diffusive processes. Since we are exploring the 0D model which does not contain transport processes, the processes occurring at low frequencies could probably be attributed to thermodynamic processes due to the changing concentrations which are modified through precipitation and electrochemical reactions. We found in Chapter 3 that the $Li_2S$ precipitation process for this parameter set is very slow, taking hours for the battery to relax fully. Thus, we believe have that the features at low frequencies can be described by a thermo-kinetic Warburg-like impedance that can be attributed to the perturbations in concentration. More detailed analysis of the structure of the governing equations and the contribution of the modulated concentrations to the voltage response will be carried out to investigate low frequency behavior.

At high frequencies, however, the impedance can be several orders of magnitude smaller and are influenced by different kinetic parameters. As shown in Figure 4.5, at 5% DOD, the semicircle is sensitive to $i_{0,2}$ and to a much smaller extent, $i_{0,3}$; while at 50% DOD semicircle is sensitive to $i_{0,3}$ and to a lesser extent, $i_{0,4}$.

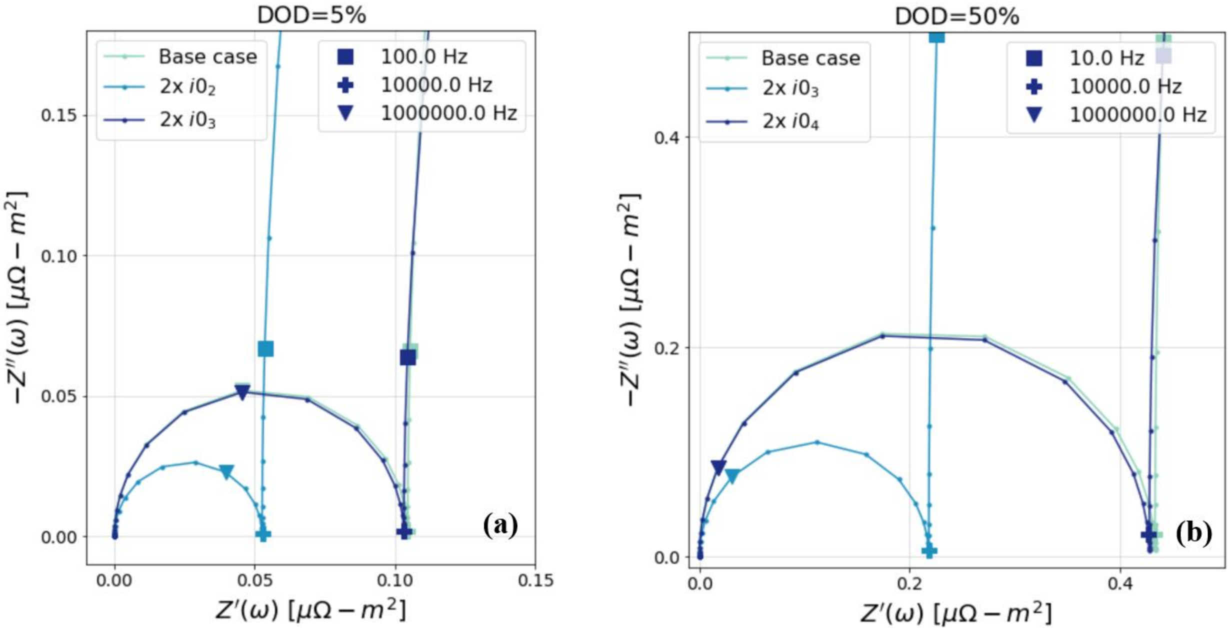

***Figure 4.5 Nyquist plots at high frequencies for (a) 5% DOD and (b) 50% DOD with varying kinetic parameters***

We can attempt to explain this high frequency behavior using the concept of charge transfer resistances. The width of the semicircle can be expressed as the charge transfer resistance for an electrochemical reaction. Since this is a 0D model of a porous electrode, we see a perfect semicircle. Also, as there are five electrochemical reactions that can occur at the pore wall interface, along with double layer capacitance charging, we can visualize an equivalent circuit model with five parallel resistances and one parallel capacitor. Each electrochemical reaction *j* will have the theoretical charge transfer resistance with units of $\Omega - m^2$,

$$R_{ct,j} = \frac{RT}{n_j F\, k_j \prod_{i=red} C_i^{\alpha p_{i,j}} \prod_{i=ox} C_i^{(1-\alpha) q_{i,j}}} \tag{4.16}$$

where *R* is the molar gas constant, *T* is temperature, $n_j$ is the number of electrons transferred in reaction *j*, *F* is Faraday's constant, $k_j$ is the rate constant of reaction *j* with varying units, $C_i$ is the concentration of species *i* in mol/m$^3$ at steady state at a particular DOD, $s_{i,j}$ is the stoichiometric coefficient of species *i* in reaction *j*, $p_{i,j} = s_{i,j}$ for anodic or reduced species, and $q_{i,j} = -s_{i,j}$ for cathodic or oxidized species, and $\alpha$ is the charge transfer coefficient.

To account for the interfacial surface area due to the porosity, the effective charge transfer resistance is,

$$R_{ct,eff,j} = \frac{R_{ct,j}}{aL_{cat}} \tag{4.17}$$

where $a$ is the specific area or surface area to volume ratio of the porous electrode in m$^{-1}$, and $L_{cat}$ is the length of the cathode in m.

$$a = a_0 \left( \frac{\varepsilon_c}{1 - \varepsilon_{c,init}} \right)^{\xi} \tag{4.18}$$

where $a_0$ is the initial specific area, $\varepsilon_c$ is the porosity of the cathode that is a function of DOD, $\varepsilon_{c,init}$ is the initial porosity, and $\xi$ is the tortuosity factor.

We can also calculate the total effective charge transfer resistance for the electrode as resistors in series,

$$\frac{1}{R_{ct,eff,total}} = \sum_j \frac{1}{R_{ct,eff,j}} \tag{4.19}$$

The reciprocal individual effective charge transfer resistances are plotted in Figure 4.6, with the total $\frac{1}{R_{ct,eff,total}}$ plotted in black. The reciprocal is equivalent to the conductance.

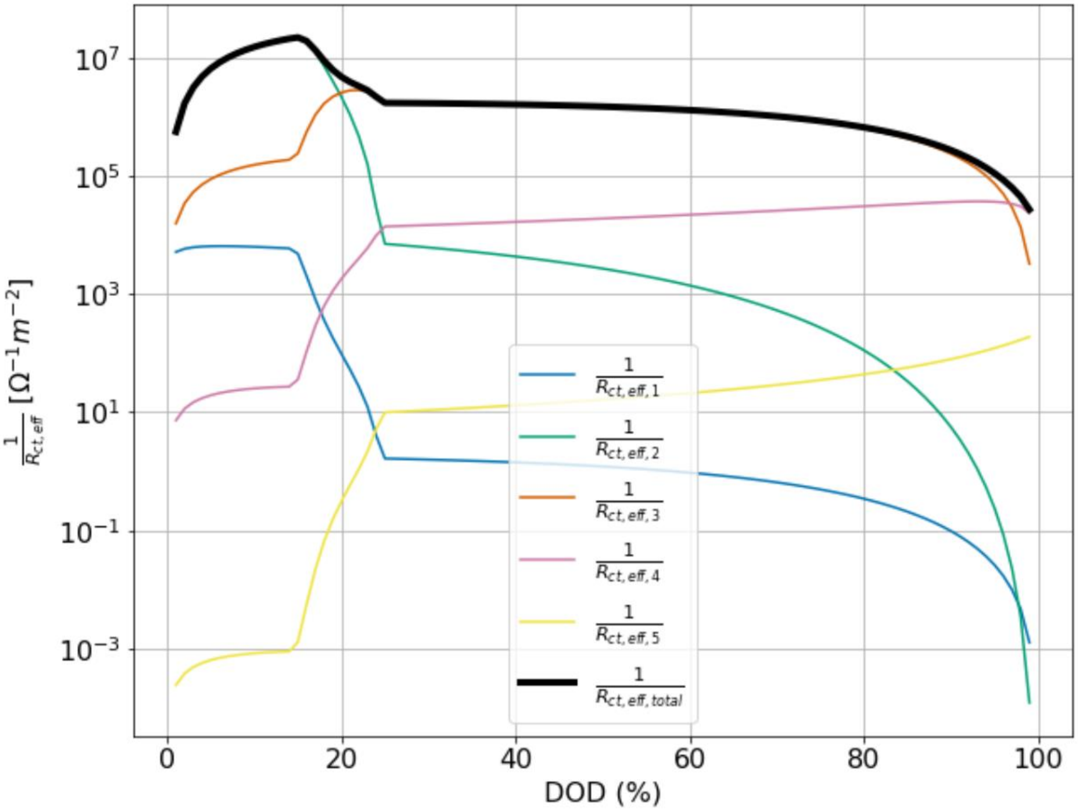

***Figure 4.6 Effective charge transfer resistances***

Only reactions with high conductance will allow current to pass through and hence contribute to the overall conductance. We see that for the majority of DODs, reaction 2 and 3 contribute to the total conductance, with some contribution from reaction 4 at the very end of DOD. Comparison of this calculated charge transfer resistance to the width of the modeled semicircles at the corresponding DODs show that the charge transfer resistances are of the same order of magnitudes, supporting this concept.

The frequency at the top of the charge transfer semicircle is typically referred to as the characteristic frequency for that process and can be calculated as,

$$f_{ct} = \frac{1}{R_{ct,eff} C_{dl}} \tag{4.20}$$

where $C_{dl}$ is the double layer capacitance with a value of 0.1 F/m$^2$.

However, the modeled characteristic frequencies are approximately an order of magnitude smaller than the calculated $f_{ct}$ for the DODs shown in Figure 4.8. More investigation needs to be done here.

The charge transfer resistances are sufficient to explain the behavior at very high frequencies. However, these resistances are many orders of magnitude smaller compared to the overall impedance spectra. Though measurable, these may not be significant to the overall performance of the battery. (Note, for this set of parameters, the discharge curve of a battery, are for the most part, insensitive to the exchange current densities.)

*Transport effects in the frequency domain*

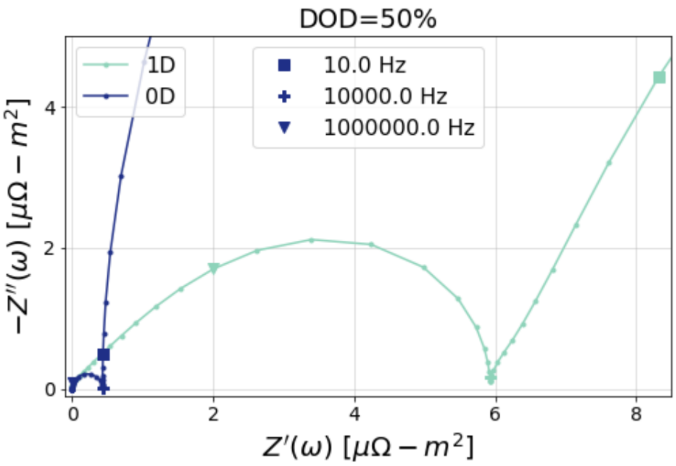

***Figure 4.7 Nyquist plot of impedance at 50% DOD comparing the 1D thermo-kinetic-transport model and the 0D thermo-kinetic model***

We use both 0D and 1D models to solve for the impedance of the lithium sulfur cathode at various DODs. In Figure 4.7, we show the difference between the Nyquist plots of the two models at 50% DOD at high frequencies (>10 Hz). Note that we shifted the 1D model’s impedance to the left, along the real axis, to begin at the origin for easier comparison with the 0D model’s impedance.

Since the 0D model has no spatial variation, electronic and ionic conductivities are not modeled and there is no ohmic resistance. However, the 1D model includes the transport of ions through the electrolyte and electrons through the solid. This is reflected by a non-zero ohmic resistance, which can be measured by the left intercept of the semicircle with the horizontal real axis.

The 0D model also shows a perfect semicircle at high frequencies while the 1D model shows an asymmetric teardrop shaped semicircle which can be attributed to the porous electrode being modeled, with non-uniform current distribution through the thickness of the electrode. This also contributes to the difference in width of the semicircles, with the 1D model having a much larger charge transfer resistance.

Impedance models can be very useful to tease out the phenomena occurring at different timescales, and we show here that building models of varying complexity allows for us to understand the spectra better. This is in comparison to simulating standard discharge curves, where there is little difference in the addition of transport phenomena when comparing the results of 0D and 1D models in Figure 4.1 and Figure 4.2, for the set of parameters used here.

### *Comparing impedance at different DODs*

We also simulated the impedance at different DODs using the 0D model. Figure 4.8 shows the Nyquist plots for DODs=1, 17, 50, and 99% DOD at varying levels of magnifications based on different frequency ranges. This does not correspond very well to what is seen in the experimental impedance literature for lithium sulfur cells in terms of the large differences in the size of the impedance at different SOCs. Experimental literature show that the impedance at different SOCs only differ by about one order of magnitude (see Ref 99), with the overall impedance decreasing and then increasing with DOD. More effort towards understanding the changes in the impedance, and correspondingly, the change in parameters with DOD can be explored.

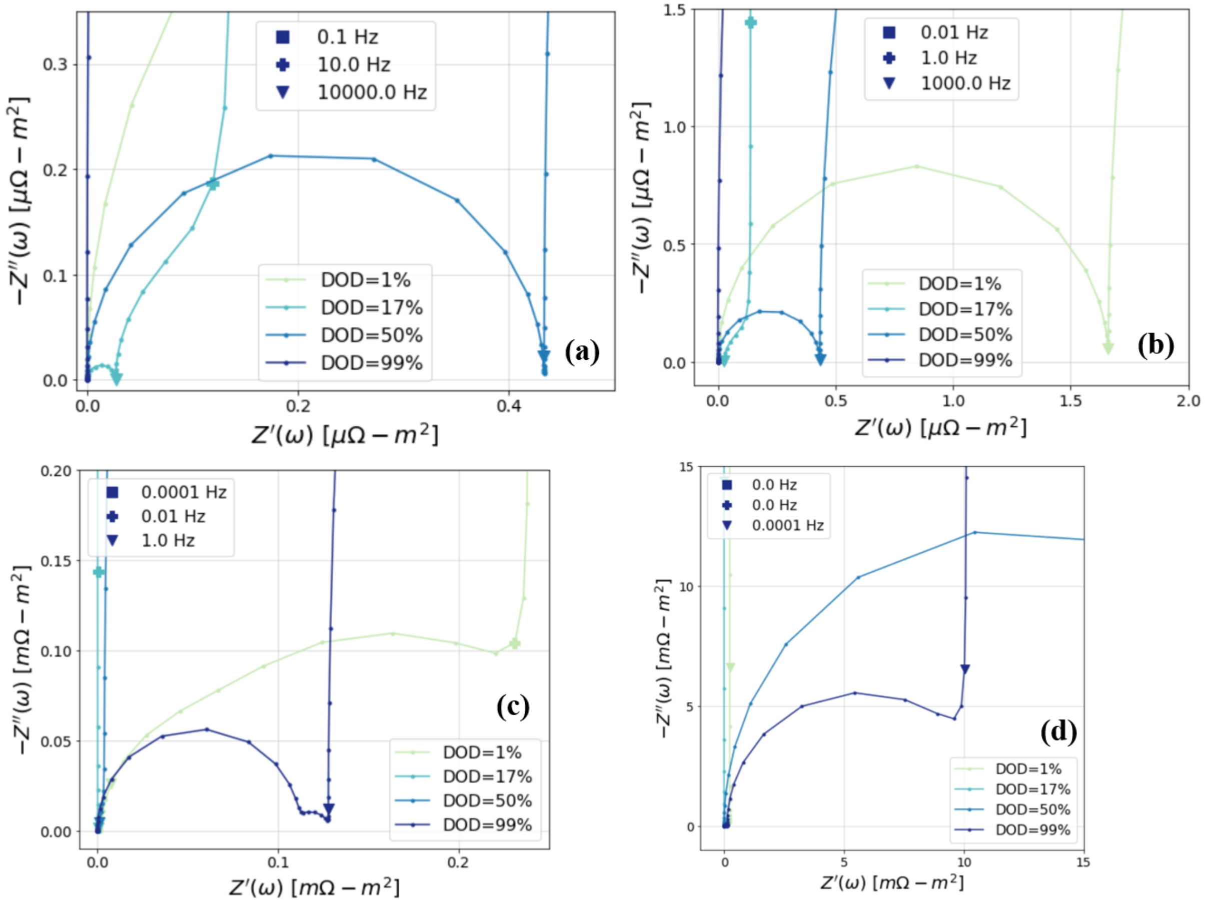

***Figure 4.8 Nyquist plots at DODs=1, 17, 50, 99%. (a)-(d) Varying levels of magnification from high to low frequencies. Note the difference in units of the axes for the different figures.***

## 4.4 Conclusion

In this chapter, we show the ability to model impedance of the lithium sulfur cathode using standard governing equations used in the literature. We solve for the impedance using both a 0D model with thermodynamics and kinetics processes and a 1D model with additional transport processes; we then explore how those differences show up in features of the impedance spectra. At high frequencies, the semicircles can be connected to the charge transfer resistances of the various electrochemical reactions. At middle to low frequencies, the thermodynamics of precipitation reactions alter the speciation, and we will attempt to analyze the corresponding features in future work.

# Chapter 5: Dynamic Electrochemical Impedance Spectroscopy of Lithium-ion Batteries – Revealing Underlying Physics through Efficient Joint Time-Frequency Modeling

*Note: this chapter was published as an article*

Teo, L.; Subramanian, V. R.; Schwartz, D. T. Dynamic Electrochemical Impedance Spectroscopy of Lithium-Ion Batteries: Revealing Underlying Physics through Efficient Joint Time-Frequency Modeling. *J. Electrochem. Soc.* **2021**, *168* (1), 010526. https://doi.org/10.1149/1945-7111/abda04.[118]

## Abstract

The value and interpretation of dynamic electrochemical impedance spectroscopy (DEIS) during the charging and discharging of lithium-ion batteries is examined using the Doyle-Fuller-Newman pseudo-two-dimensional (P2D) lithium-ion battery model with parameters for a lithium-cobalt-oxide/graphite cell. Two computational approaches are explored to balance accuracy, speed, and interpretability: (i) A brute force time domain calculation of the full nonlinear equation set subject to direct current (DC) plus superimposed sinusoidal modulation of frequency $\omega_1$, followed by post-processing with short-time Fourier transforms to track the dynamic impedance signal at the modulation frequency during charge and discharge; (ii) A fast-computing time-separated method that solves the C-rate dependent P2D equations for the DC charge/discharge transients occurring on the slow time-scales, $t_b$ ~O(3600s/C), followed by solutions to linearized frequency domain equations derived for direct computation of the dynamic impedance signal. The time-separated method is rigorously correct in the limit $1/(t_b\omega_1) \rightarrow 0$. Key physics that drives differences between stationary and dynamic EIS signals is easily explored with the time-separated method. C-rate dependent studies show that DEIS signals are selectively sensitive to interfacial processes in ways that may be promising for real-time diagnostics and control of the negative electrode at high states-of-charge (SOC) and the positive electrode at low SOCs.

## 5.1 Introduction

A powerful and commonly used laboratory analytical tool for battery diagnostics is electrochemical impedance spectroscopy (EIS). EIS is particularly insightful because its signal at different frequencies can be ascribed to separate electrochemical processes based on their characteristic time constants,[119] and its small amplitude input modulation (needed to ensure a linear response) generally makes the method non-destructive.[120] A fundamental condition for EIS is that the system exhibits stationarity, *i.e.*, the cell must be operating at a steady periodic state. For a closed system like a sealed battery, stationarity requires the cell to be relaxed to an equilibrated state, with no applied DC current, before the AC current of an EIS measurement is applied. Transient impedance-like signals can be measured in sealed cells being discharged or charged – a technique sometimes called dynamic EIS (DEIS), *in situ* EIS, or fast Fourier transform-EIS (FFT-EIS) – though interpretation of these signals can be difficult.

Previous work on impedance-like measurements of non-stationary electrochemical systems started in the electroanalytical chemistry field to probe rapidly changing electrode surfaces or reaction mechanisms at electrode interfaces.[121] Many variations of this DEIS technique have been developed with two main methods. The first is coined AC voltammetry or FFT-EIS where either single[122] or multi-frequency[123,124] perturbations are applied during cyclic voltammetry, or in some cases a staircase potential scan instead of a linear scan.[125] The second method is continuous frequency by frequency sweeps as a function of time for a non-stationary system.[126] Bandarenka gives a detailed review of the different variations of DEIS techniques and progress in the field in terms of optimizing for noise, measurement time reduction, and measurement over a wider frequency range.[121]

While most DEIS measurements in the electroanalytical field have been potentiodynamic measurements, the technique also has been adopted to battery systems in a galvanodynamic manner. A few DEIS studies on lead acid and lithium-ion battery systems have been carried out by using a continuous frequency sweep with a DC current. This method assumes that the state-of-charge (SOC) of the cell does not deviate either by operating within a small SOC range (1% [127] or 5% SOC [128]), keeping measurement time short (i.e., measurements frequencies greater than 1 Hz[129] or 10 Hz[130]), or assuming that the battery's state is a continuous space such that EIS spectra can be interpolated as a function of time while charging/discharging.[131,132] Huang et al. observed the appearance of inductive behavior in DEIS spectra at lower frequencies and proposed that this was due to the stationarity condition being violated.[133] In a different approach, Huang et al. conducted DEIS by using single frequency perturbations with a DC current bias over an entire charge or discharge and repeating this over many frequencies. They were then able to reconstruct entire EIS-like dynamic spectra at different times of charge/discharge which correspond to different SOCs of the battery.[134]

Huang et al. showed that the dynamic impedance-like signal of a commercial lithium-ion cell is smaller during charging than during discharging, and attributed it to the dynamic charge transfer resistance of the positive electrode being smaller during charging than discharging.[134] Itagaki et al. used DEIS signals in a three-electrode cell to investigate charge transfer mechanisms for intercalation and deintercalation of lithium, concluding that charge transfer resistance of the deintercalation reaction increases when the cell is under load.[132] In separate works, Itagaki et al. also explored the solid electrolyte interface (SEI) formation on graphite and $LiCoO_2$ electrodes using DEIS.[135,136]

Almost all efforts to analyze and interpret DEIS experiments with lithium-ion batteries have adapted equivalent circuit models.[127,137] Though relatively easy to implement, equivalent circuit models lack an ability to confidently relate the dynamic change seen in a DEIS experiment to the battery's detailed physical and chemical processes. Physics-based models have been much less explored for DEIS. Huang et al. used a time domain porous electrode model to simulate a battery undergoing DEIS. They processed the signal using a Gaussian impulse window function and performed an analytical Fourier transform to estimate the dynamic impedance.[138] However, their effort revealed the challenge of time domain modeling, namely, a mismatch between analytical and time domain numerical models of stationary EIS (SEIS), which they ascribe to numerical error in the time domain model. Time domain models simulate the same output signals that are obtained experimentally from a battery, and therefore require subsequent joint time-frequency analysis (JTFA) of the signal, but they are computationally expensive.

Sensing is an essential part of sophisticated battery management techniques used to enhance performance during discharging and charging of batteries.[139] Measuring and using impedance-like DEIS signals as part of a dynamic control scheme that, for example, manages interfacial processes during charging, requires an understanding of how the dynamic and stationary EIS signals are related to one another. In this paper, we will take two approaches, first using time domain computations akin to the previous work done by Huang et al.,[138] using the Doyle-Fuller-Newman (DFN) pseudo-two-dimensional (P2D) porous electrode model,[140,141] followed by signal processing and transformation to the frequency domain. Here we term this “brute force” JTFA calculations. We will then explore a computationally efficient, physics-illuminating, approximate method to simulate DEIS that uses a separation of timescales to show the origins and quantitative impacts of physicochemical processes that are active in DEIS measurements but not in classical SEIS spectra.

## 5.2 Methods and Their Rationale

*Brute force DEIS calculations: Time domain P2D solutions with JTFA*

The lithium-ion battery DFN P2D model used here is based on porous electrode theory and involves the solution and solid phases – electrolyte in pores and spherical particles that make up the electrode material matrix – to be treated as superimposed continua by volume-averaging.[142] Diffusion of lithium-ions in both phases are considered, along with Ohm’s law for the potentials, and Butler-Volmer kinetics for the pore wall flux. This electrochemical model is widely used in the literature due to its inclusion of key physical processes and ability to provide understanding of batteries on a continuum level.

Governing equations, boundary conditions, other expressions, and parameters used for this study can be found in ***Table 5.4***,

***Table 5.5***, and ***Table 5.6***. The cell being modeled has physicochemical properties associated with graphite for the negative electrode and $LiCoO_2$ for the positive electrode.[143] For the purposes of this time domain simulation of DEIS, the equations usually used for DC simulations have been modified to include the non-faradaic double layer capacitance as a component of the currents at the solid-solution interfaces. This makes the time domain brute force calculations consistent with Meyers-Doyle-Newman's frequency domain impedance model which is used (in modified form) later on.[144,145] The variables that are solved are potentials and concentrations in the solid and solution phases for the anode, separator, and cathode.

***Table 5.1 List of Variables***

| Symbol | Variable | Units |
|---|---|---|
| $c$ | Electrolyte concentration | mol/m$^3$ |
| $c^s$ | Solid phase concentration | mol/m$^3$ |
| $\Phi$ | Liquid phase potential | V |
| $\Phi^s$ | Solid phase potential | V |
| $j_f$ | Faradaic pore wall flux | mol/(m$^2$ s) |
| $i0$ | Exchange current density | A/m$^2$ |
| $U$ | Open circuit potential | V |
| $\eta$ | Overpotential | V |
| $\kappa$ | Ionic conductivity | S/m |
| $a$ | Specific surface area of electrode | m$^2$/m$^3$ |

***Table 5.2 List of Subscripts***

| | |
|---|---|
| $eff$ | Effective, as for diffusivity or conductivity |
| $n$ | Related to the negative electrode—the anode |
| $p$ | Related to the positive electrode—the cathode |
| $s$ | Related to the separator |
| $surf$ | Surface, as for solid phase concentration |
| 0 | Zero order mean term |
| 1 | First harmonic |

***Table 5.3 List of Superscripts***

| | |
|---|---|
| $s$ | Related to solid phase |
| $'$ | Related to real part |
| $''$ | Related to imaginary part |

*Table 5.4 List of Parameters*

| Symbol | Parameter | Positive Electrode | Separator | Negative Electrode | Units |
|---|---|---|---|---|---|
| $\alpha_a$ | Anodic charge transfer coefficient | 0.5 | | 0.5 | |
| $\alpha_c$ | Cathodic charge transfer coefficient | 0.5 | | 0.5 | |
| $\sigma_i$ | Solid phase conductivity | 100 | | 100 | S/m |
| $\varepsilon_{f,i}$ | Filler fraction | 0.025 | | 0.0326 | |
| $\varepsilon_i$ | Porosity | 0.385 | 0.724 | 0.485 | |
| Brugg | Bruggeman Coefficient | 4 | | | |
| $C_{dl,i}$ | Double layer capacitance | 0.1 [a] | | 0.7 [b] | F/m$^2$ |
| $D$ | Electrolyte diffusivity | $7.5\times10^{-10}$ | | | m$^2$/s |
| $D_i^s$ | Solid phase diffusivity | $1.0\times10^{-14}$ | | $3.9\times10^{-14}$ | m$^2$/s |
| $k_i$ | Reaction rate constant | $2.334\times10^{-11}$ | | $5.031\times10^{-11}$ | mol/(s m$^2$)/(mol/m$^3$)$^{1+\alpha a,i}$ |
| $c_{i,\max}^s$ | Maximum solid phase concentration | 51554 | | 30555 | mol/m$^3$ |
| $\theta_{i,100}$ | Fraction of solid phase lithiation at 100% SOC | 0.49551 | | 0.85512 | |
| $\theta_{i,0}$ | Fraction of solid phase lithiation at 0% SOC | 0.94719 | | 0.00819 | |
| $c_0$ | Initial electrolyte concentration | 1000 | | | mol/m$^3$ |
| $R_i$ | Particle radius | $2.0\times10^{-6}$ | | $2.0\times10^{-6}$ | m |
| $l_i$ | Region thickness | $80\times10^{-6}$ | $25\times10^{-6}$ | $88\times10^{-6}$ | m |
| $t_+$ | Transference number | 0.363 | | | |
| $F$ | Faraday's constant | 96487 | | | C/mol |
| $R$ | Gas constant | 8.314 | | | J/(mol K) |
| $T$ | Temperature | 298.15 | | | K |
| $I$ | Current density (1C) | 29 | | | A/m$^2$ |
| $I_{app}$ | Current density for impedance | 1 | | | A/m$^2$ |

---

[a] See Ref [146]

[b] adjusted

***Table 5.5 Governing Equations for Time Domain P2D Model***

| **Governing Equations** | **Boundary Conditions** |
|---|---|
| Negative Electrode | |
| $\varepsilon_n \frac{\partial c_n}{\partial t} = \frac{\partial}{\partial x}\left[ D_{\text{eff,n}} \frac{\partial c_n}{\partial x} \right] + a_n \left(1 - t_+\right) j_{f,n} + \frac{a_n\, C_{dl,n}\, (1-t_+)}{F} \frac{\partial\left(\Phi_n^s - \Phi_n\right)}{\partial t}$ | At x=0<br>$\frac{\partial c_n}{\partial x}$=0<br>At x=l$_n$<br>$-D_{\text{eff,n}} \frac{\partial c_n}{\partial x} = -D_{\text{eff,s}} \frac{\partial c_s}{\partial x}$ |
| $-\sigma_{\text{eff,n}} \left( \frac{\partial \Phi_n^s}{\partial x} \right) - \kappa_{\text{eff,n}} \left( \frac{\partial \Phi_n}{\partial x} \right) + \frac{2\kappa_{\text{eff,n}} RT \left(1 - t_+\right)}{F} \left( \frac{\partial \ln c_n}{\partial x} \right) = I$ | At x=0<br>$\Phi_n$=0<br>At x=l$_n$<br>$-\kappa_{\text{eff,n}} \frac{\partial \Phi_n}{\partial x} = -\kappa_{\text{eff,s}} \frac{\partial \Phi_s}{\partial x}$ |
| $\frac{\partial}{\partial x}\left[ \sigma_{\text{eff,n}} \frac{\partial}{\partial x} \Phi_n^s \right] = a_n F j_{f,n} + a_n C_{dl,n} \frac{\partial\left(\Phi_n^s - \Phi_n\right)}{\partial t}$ | At x=0<br>$\frac{\partial \Phi_n^s}{\partial x} = -\frac{I}{\sigma_{eff,n}}$<br>At x=l$_n$<br>$\frac{\partial \Phi_n^s}{\partial x}$=0 |
| $\frac{\partial c_n^s}{\partial t} = \frac{1}{r^2} \frac{\partial}{\partial r}\left[ r^2 D_n^s \frac{\partial c_n^s}{\partial r} \right]$ | At r=0<br>$\frac{\partial c_n^s}{\partial r} = 0$<br>At r=R$_n$<br>$-D_n^s \frac{\partial c_n^s}{\partial r} = j_{f,n}$ |
| Separator | |
| $\varepsilon_s \frac{\partial c_s}{\partial t} = \frac{\partial}{\partial x}\left[ D_{\text{eff,s}} \frac{\partial c_s}{\partial x} \right]$ | At x=l$_n$<br>$c_n = c_s$<br>At x=l$_n$+l$_s$<br>$c_s = c_p$ |
| $-\kappa_{\text{eff,s}} \left( \frac{\partial \Phi_s}{\partial x} \right) + \frac{2\kappa_{\text{eff,s}} RT \left(1 - t_+\right)}{F} \left( \frac{\partial \ln c_S}{\partial x} \right) = I$ | At x=l$_n$<br>$\Phi_n = \Phi_s$<br>At x=l$_n$+l$_s$ |

| | |
|---|---|
| | $\Phi_s = \Phi_p$ |
| Positive Electrode | |
| $\varepsilon_p \frac{\partial c_p}{\partial t} = \frac{\partial}{\partial x}\left[ D_{\text{eff,p}} \frac{\partial c_p}{\partial x} \right] + a_p \left(1 - t_+\right) j_{f,p} + \frac{a_p\, C_{dl,p}\, (1-t_+)}{F} \frac{\partial \left(\Phi_p^s - \Phi_p\right)}{\partial t}$ | <u>At x=l<sub>n</sub>+l<sub>s</sub></u><br>$-D_{\text{eff,s}} \frac{\partial c_s}{\partial x} = -D_{\text{eff,p}} \frac{\partial c_p}{\partial x}$<br><u>At x=l<sub>n</sub>+l<sub>s</sub>+l<sub>p</sub></u><br>$\frac{\partial c_p}{\partial x} = 0$ |
| $-\sigma_{\text{eff,p}} \left( \frac{\partial \Phi_p^s}{\partial x} \right) - \kappa_{\text{eff,p}} \left( \frac{\partial \Phi_p}{\partial x} \right) + \frac{2\kappa_{\text{eff,p}} RT \left(1 - t_+\right)}{F} \left( \frac{\partial \ln c_p}{\partial x} \right) = I$ | <u>At x=l<sub>n</sub>+l<sub>s</sub></u><br>$-\kappa_{\text{eff,s}} \frac{\partial \Phi_s}{\partial x} = -\kappa_{\text{eff,p}} \frac{\partial \Phi_p}{\partial x}$<br><u>At x=l<sub>n</sub>+l<sub>s</sub>+l<sub>p</sub></u><br>$\frac{\partial \Phi_p}{\partial x} = 0$ |
| $\frac{\partial}{\partial x}\left[ \sigma_{\text{eff,p}} \frac{\partial}{\partial x} \Phi_p^s \right] = a_p F j_{f,p} + a_p C_{dl,p} \frac{\partial \left(\Phi_p^s - \Phi_p\right)}{\partial t}$ | <u>At x=l<sub>n</sub>+l<sub>s</sub></u><br>$\frac{\partial \Phi_p^s}{\partial x} = 0$<br><u>At x=l<sub>n</sub>+l<sub>s</sub>+l<sub>p</sub></u><br>$\frac{\partial \Phi_p^s}{\partial x} = -\frac{I}{\sigma_{eff,p}}$ |
| $\frac{\partial c_p^s}{\partial t} = \frac{1}{r^2} \frac{\partial}{\partial r}\left[ r^2 D_p^s \frac{\partial c_p^s}{\partial r} \right]$ | <u>At r=0</u><br>$\frac{\partial c_p^s}{\partial r} = 0$<br><u>At r=R<sub>p</sub></u><br>$-D_p^s \frac{\partial c_p^s}{\partial r} = j_{f,p}$ |

## *Table 5.6 Additional Equations - General*

$$\kappa_{eff,i} = \varepsilon_i^{Brugg} \left[ 4.1253*10^{-2} + 5.007*10^{-4} * c_i - 4.7212*10^{-7} * c_i^{\,2} + 1.5094*10^{-10} * c_i^{\,3} - 1.6018*10^{-14} * c_i^{\,4} \right],\ i = n, s, p$$

$$\sigma_{eff,i} = \sigma_i (1 - \varepsilon_i - \varepsilon_{f,i}),\ \ i = n, p$$

$$D_{eff,i} = D \varepsilon_i^{Brugg},\ \ i = n, s, p$$

$$a_i = \frac{3}{R_i}(1 - \varepsilon_i - \varepsilon_{f,i}),\ \ i = n, p$$

$$j_{f,i} = k_i (c_{i,max}^s - c_{i,surf}^s)^{\alpha_{a,i}} (c_i)^{\alpha_{a,i}} (c_{i,surf}^s)^{\alpha_{c,i}} \left[ \exp\left( \frac{\alpha_{a,i} F}{RT} \eta_i \right) - \exp\left( \frac{-\alpha_{c,i} F}{RT} \eta_i \right) \right],\ \ i = n, p$$

$$\eta_i = \Phi_i^s - \Phi_i - U_i\,,\ \ i = n, p$$

$$U_n = 0.7222 + 0.1387\theta_n + 0.029\theta_n^{0.5} - \frac{0.0172}{\theta_n} + \frac{0.0019}{\theta_n^{1.5}} + 0.2808 exp(0.90 - 15\theta_n) - 0.7984 * exp(0.4465\theta_n - 0.4108)$$

$$U_p = \frac{-4.656 + 88.669\theta_p^{\ 2} - 401.119\theta_p^{\ 4} + 342.909\theta_p^{\ 6} - 462.471\theta_p^{\ 8} + 433.434 * \theta_p^{\ 10}}{-1 + 18.933\theta_p^{\ 2} - 79.532\theta_p^{\ 4} + 37.311\theta_p^{\ 6} - 73.083\theta_p^{\ 8} + 95.96\theta_p^{\ 10}}$$

$$\theta_i = c_{i,surf}^s \ / \ c_{i,max}^s$$

Using this time domain model, the battery was simulated with a modulated input current $I(t) = I_0 + \Delta I\cos(2\pi\omega_1 t)$, where $I_0$ is the mean applied DC charge or discharge current, $\Delta I$ is the AC amplitude, and $\omega_1$ is the oscillation frequency in Hz. In the limit of small modulation amplitudes, the instantaneous voltage response, $V(t;\omega_1, \Delta I)$, is the sum of the dynamic DC voltage response with a superimposed AC oscillating component. We note here the introduction of notation X(a,b;c,d) to indicate X as a dependent variable, a, b as the independent variables, and c, d are parameters of the solution method (we do not include the vector of physicochemical parameters, as they are fixed here to represent one battery chemistry). The battery was also simulated with a constant DC discharge or charge ($\Delta I = 0$) to obtain the pure dynamic DC voltage signal without any oscillatory component. Thus, in the brute force time domain method for DEIS computations, we calculate the oscillating discharge/charge curves at each frequency and C-rate of interest, and the comparable pure DC curve at the same C-rate, and by subtraction, get the oscillating signal used in the JTFA. All the simulations presented here used a sampling rate of 8 points per oscillation cycle, providing a JTFA Nyquist frequency four times the oscillation frequency $\omega_1$.

To simplify discussion of the JTFA method, we used straightforward short-time Fourier transforms (STFT) with a moving rectangular window *n* oscillations wide (here, $n=4$) that was centered at the battery discharge (or charge time) we denote, $t_b$. Thus, the STFT produces a local (short time) measure of the spectral components acquired over the window $\Delta t_{EIS} = n/\omega_1$. The STFT was used on the oscillating time domain current and voltage signals to provide complex Fourier spectra in the frequency domain. In the small amplitude linear limit used here, evaluating the ratio of the complex voltage $\tilde{V}(\omega; t_b, \Delta I)$ and current $\tilde{I}(\omega; t_b, \Delta I)$ spectra at the excitation frequency $\omega = \omega_1$ gives the complex impedance, $\tilde{Z}(\omega_1; t_b)$ at the particular charge/discharge time $t_b$.

### *Time-separated analysis of DEIS*

The discussion of STFT illustrates there are two key timescales in DEIS, one associated with the slow dynamics of battery charge/discharge, we labeled this $t_b$, and a local timescale associated with measuring the spectrum, $\Delta t_{EIS}$. The characteristic "slow" DC charge/discharge dynamics for a battery scales as $\sim O(3600s/C)$, where C is the C-rate, and the characteristic "fast" AC dynamic scales as $\sim O(1/\omega_1)$. Thus, there is a rigorous separation of timescales for the DC and AC responses in the limit $\frac{C}{3600s*\omega_1} \rightarrow 0$. In this limit, the fast AC measurement occurs instantaneously as a perturbation to the slow DC condition in the battery at time $t_b$; there is no time for the slow DC values to change during measurement. Thus, when the timescales are widely separated in magnitude, one can formulate a computationally efficient analytic-numeric DEIS method that separately computes the slow dynamic DC behavior for any time $t_b$, and uses those DC results in the computation of the dynamic AC response at varying modulation frequencies to determine the DEIS spectrum.

To formulate the time-separated DEIS model, we rely heavily on the notation *X(a,b;c,d)* to clarify the hierarchical nature of the solutions that arise from the analytical mathematical formulation. In the time-separated DEIS formulation, all the dependent variables are represented as the sum of a mean term and a small amplitude, linear term:

$$X(x,r,t_b,t';\omega_1,\Delta I) = \overline{X_0}(x,r,t_b) + X_1(x,r;\omega_1,t_b) * \Delta I * Re\{exp(j2\pi\omega_1 t')\} \tag{5.1}$$

where the key feature is that any time $t = t_b + t'$ is the sum of the charge/discharge time and a fast local perturbation time t', with the problem solution involving only a single timescale as independent variable. Thus, $\overline{X_0}(x,r,t_b)$ is the pure DC charge/discharge response of the system, without oscillation, at time $t_b$. The complex AC response term $\tilde{X}_1(x,r;\omega_1,t_b)$ can be written as $\tilde{X}_1 = \tilde{X}_1' - j\tilde{X}_1''$, where the independent spatial variables are $x$ and $r$, whereas $\omega_1$ and $t_b$, are parameters of the solution, meaning, they are specified and their values modify the solution. Finally, we introduce $t'$ in the circular function, as the local timescale associated with the short-time AC measurement. The difference between the analytical form of Eq. (5.1) for time-separated DEIS and the analytical form used by Doyle et al.[145] and Meyers et al.[144] to compute SEIS solutions from the same P2D model can be illustrative to consider. Using our nomenclature, the SEIS formulation used by Doyle and Meyers was:

$$X(x,r,t';\omega_1,\Delta I)=\overline{X}_0+X_1(x,r;\omega_1)*\Delta I*Re\left\{exp(j2\pi\omega_1 t')\right\} \tag{5.2}$$

where the mean dependent variables $\overline{X_0}$ for a stationary battery system are all constants with no spatial variations (i.e., fully relaxed DC states), and all of the time dependence resides solely in the local AC oscillating term. In contrast, Eq. (5.1) embeds the dynamic processes (e.g., internal gradients) from the slow charge or discharge history up to time $t_b$ in both the DC mean (as an independent variable) and the DEIS response (as a parameter of the AC solution). The SEIS formulation in Eq. (5.2) is independent of the time-dependent pathway the battery took to achieve any particular relaxed SOC whereas the DEIS formulation (Eq. (5.1)) embeds the pathway to a particular SOC at time $t_b$. This subtle difference is what makes our DEIS computations sensitive to the battery operation (e.g., charge or discharge history), as is observed experimentally. Nonetheless, it remains computationally efficient, because we can use methods of solution that are separately optimized for real-time computation of the DC charge/discharge[147] and the impedance response.[146]

To determine the governing equations to be solved, the functional form Eq. (5.1) is inserted into the P2D governing equations, boundary, and initial conditions. Terms are segregated into equations for the time-dependent DC variables $\overline{X_0}(x,r,t_b)$ and the real and imaginary oscillating components of $\tilde{X}_1(x,r;\omega_1,t_b)$, with nonlinear quadratic terms (arising from AC fluctuations multiplying each other) being ignored as small. The governing equations for the dynamic DC dependent variables $\overline{X_0}(x,r,t_b)$ end up being identical to the brute force model with $\Delta I=0$ (a classic P2D solution). Thus, the DC charge or discharge need only be computed once for each C-rate of interest, for the given set of physicochemical properties being studied.

The governing equations and boundary conditions for the complex AC dependent variables $\tilde{X}_1(x,r;\omega_1,t_b)$ share many of the same terms as the SEIS governing equations developed for the P2D model by Doyle et al.,[145] though the existence of concentration and potential gradients in the dynamic DC solution at a given time $t_b$ results in additional terms to the DEIS equations solved here. An example of the derivation of one equation is provided in the Appendix. The governing equations and boundary conditions in ***Table 5.7*** and ***Table 5.8*** are, to the best of our knowledge, a unique formulation of DEIS that clearly illuminates the differences in physics considered between SEIS and DEIS measurements.

The real and imaginary AC variables $\widetilde{X}'(x,r;\omega_1,t_b)$ and $\widetilde{X''}(x,r;\omega_1,t_b)$ can be solved at each frequency $\omega_1$ and charge/discharge time $t_b$, using the independently computed DC mean variables $\overline{X_0}(x,r,t_b)$. Thus, the governing equations are solved hierarchically, first the DC solution is solved for all times of interest, and then the AC variables are computed (using the DC results for the $t_b$ of interest). For both the DC time domain and AC frequency domain models, the equations are numerically solved by performing coordinate transformations for each anode/separator/cathode/solid-particle region, and then discretizing using orthogonal collocation. This basic method is detailed in previous work.[146,147] For converged results, even at extremely high frequencies, the number of collocation points used in each region is 10 and 8 for collocation in the x and r spatial dimensions respectively. Note that for simulating discharge curves for most chemistries (up to 5C rates), one would typically need less than 5,2,5,3 collocation points in the anode/separator/cathode/solid-particle.

***Table 5.7 Time-separated Frequency Domain Governing Equations***

| **Governing Equations** | **Boundary Conditions** |
|---|---|
| Negative Electrode | |
| $-\varepsilon_n \, \omega \, c''_{n,1} = \frac{\partial}{\partial x}\left[D_{eff,n}\frac{\partial c'_{n,1}}{\partial x}\right] + a_n \, (1-t_+) \, j'_{f,n,1} - \frac{a_n \, C_{dl,n} \, (1-t_+)}{F}\omega[\Phi^{s''}_{n,1} - \Phi''_{n,1}]$<br>$\varepsilon_n \, \omega \, c'_{n,1} = \frac{\partial}{\partial x}\left[D_{eff,n}\frac{\partial c''_{n,1}}{\partial x}\right] + a_n \, (1-t_+) \, j''_{f,n,1} + \frac{a_n \, C_{dl,n} \, (1-t_+)}{F}\omega[\Phi^{s'}_{n,1} - \Phi'_{n,1}]$ | At x=0<br>$\frac{\partial c'_{n,1}}{\partial x} = 0$<br>$\frac{\partial c''_{n,1}}{\partial x} = 0$<br>At x=$l_n$<br>$-D_{eff,n}\frac{\partial c'_{n,1}}{\partial x} = -D_{eff,s}\frac{\partial c'_{s,1}}{\partial x}$<br>$-D_{eff,n}\frac{\partial c''_{n,1}}{\partial x} = -D_{eff,s}\frac{\partial c''_{s,1}}{\partial x}$ |

| | |
|---|---|
| $\frac{\partial}{\partial x}\left[\sigma_{eff,n}\frac{\partial \Phi^{s'}_{n,1}}{\partial x}\right]+\frac{\partial}{\partial x}\left[\overline{\kappa_{eff,n,0}}\frac{\partial \Phi^{'}_{n,1}}{\partial x}+\left.\frac{\partial \kappa_{eff,n}}{\partial c_n}\right\vert_{c_n=\overline{c_{n,0}}} c^{'}_{n,1}\frac{\partial \overline{\Phi_{n,0}}}{\partial x}\right]$<br>$=\frac{\partial}{\partial x}\left[\frac{2\,\overline{\kappa_{eff,n,0}}\,RT\,(1-t_+)}{F}\left\{\frac{1}{\overline{c_{n,0}}}\frac{\partial c^{'}_{n,1}}{\partial x}-\frac{c^{'}_{n,1}}{\overline{c_{n,0}}^{2}}\frac{\partial \overline{c_{n,0}}}{\partial x}\right\}+\frac{2RT(1-t_+)}{F}\left.\frac{\partial \kappa_{eff,n}}{\partial c_n}\right\vert_{c_n=\overline{c_{n,0}}}\frac{c^{'}_{n,1}}{\overline{c_{n,0}}}\frac{\partial \overline{c_{n,0}}}{\partial x}\right]$<br>$\frac{\partial}{\partial x}\left[\sigma_{eff,n}\frac{\partial \Phi^{s''}_{n,1}}{\partial x}\right]+\frac{\partial}{\partial x}\left[\overline{\kappa_{eff,n,0}}\frac{\partial \Phi^{''}_{n,1}}{\partial x}+\left.\frac{\partial \kappa_{eff,n}}{\partial c_n}\right\vert_{c_n=\overline{c_{n,0}}} c^{''}_{n,1}\frac{\partial \overline{\Phi_{n,0}}}{\partial x}\right]$<br>$=\frac{\partial}{\partial x}\left[\frac{2\,\overline{\kappa_{eff,n,0}}\,RT\,(1-t_+)}{F}\left\{\frac{1}{\overline{c_{n,0}}}\frac{\partial c^{''}_{n,1}}{\partial x}-\frac{c^{''}_{n,1}}{\overline{c_{n,0}}^{2}}\frac{\partial \overline{c_{n,0}}}{\partial x}\right\}+\frac{2RT(1-t_+)}{F}\left.\frac{\partial \kappa_{eff,n}}{\partial c_n}\right\vert_{c_n=\overline{c_{n,0}}}\frac{c^{''}_{n,1}}{\overline{c_{n,0}}}\frac{\partial \overline{c_{n,0}}}{\partial x}\right]$ | At x=0<br>$\frac{\partial \Phi^{'}_{n,1}}{\partial x}=0$<br>$\frac{\partial \Phi^{''}_{n,1}}{\partial x}=0$<br>At x=$l_n$<br>$\overline{\kappa_{eff,n,0}}\frac{\partial \Phi^{'}_{n,1}}{\partial x}+\left.\frac{\partial \kappa_{eff,n}}{\partial c_n}\right\vert_{c_n=\overline{c_{n,0}}} c^{'}_{n,1}\frac{\partial \overline{\Phi_{n,0}}}{\partial x}$<br>$=\overline{\kappa_{eff,s,0}}\frac{\partial \Phi^{'}_{s,1}}{\partial x}+\left.\frac{\partial \kappa_{eff,s}}{\partial c_s}\right\vert_{c_s=\overline{c_{s,0}}} c^{'}_{s,1}\frac{\partial \overline{\Phi_{s,0}}}{\partial x}$<br>$\overline{\kappa_{eff,n,0}}\frac{\partial \Phi^{''}_{n,1}}{\partial x}+\left.\frac{\partial \kappa_{eff,n}}{\partial c_n}\right\vert_{c_n=\overline{c_{n,0}}} c^{''}_{n,1}\frac{\partial \overline{\Phi_{n,0}}}{\partial x}$<br>$=\overline{\kappa_{eff,s,0}}\frac{\partial \Phi^{''}_{s,1}}{\partial x}+\left.\frac{\partial \kappa_{eff,s}}{\partial c_s}\right\vert_{c_s=\overline{c_{s,0}}} c^{''}_{s,1}\frac{\partial \overline{\Phi_{s,0}}}{\partial x}$ |
| $\frac{\partial}{\partial x}\left[\sigma_{eff,n}\frac{\partial \Phi^{s'}_{n,1}}{\partial x}\right]=a_n\,F\,j^{'}_{f,n,1}-a_n\,C_{dl,n}\omega[\Phi^{s''}_{n,1}-\Phi^{''}_{n,1}]$<br>$\frac{\partial}{\partial x}\left[\sigma_{eff,n}\frac{\partial \Phi^{s''}_{n,1}}{\partial x}\right]=a_n\,F\,j^{''}_{f,n,1}+a_n\,C_{dl,n}\omega[\Phi^{s'}_{n,1}-\Phi^{'}_{n,1}]$ | At x=0<br>$\frac{\partial \Phi^{s'}_{n,1}}{\partial x}=-\frac{I_{app}}{\sigma_{eff,n}}$<br>$\frac{\partial \Phi^{s''}_{n,1}}{\partial x}=0$<br>At x=$l_n$<br>$\frac{\partial \Phi^{s'}_{n,1}}{\partial x}=0$<br>$\frac{\partial \Phi^{s''}_{n,1}}{\partial x}=0$ |
| $-\omega\,c^{s''}_{n,1}=\frac{1}{r^2}\frac{\partial}{\partial r}\left[r^2 D^s_n\frac{\partial c^{s'}_{n,1}}{\partial r}\right]$<br>$\omega\,c^{s'}_{n,1}=\frac{1}{r^2}\frac{\partial}{\partial r}\left[r^2 D^s_n\frac{\partial c^{s''}_{n,1}}{\partial r}\right]$ | At r=0<br>$\frac{\partial c^{s'}_{n,1}}{\partial r}=0$<br>$\frac{\partial c^{s''}_{n,1}}{\partial r}=0$<br>At r=$R_n$<br>$-D^s_n\frac{\partial c^{s'}_{n,1}}{\partial r}=j^{'}_{f,n,1}$<br>$-D^s_n\frac{\partial c^{s''}_{n,1}}{\partial r}=j^{''}_{f,n,1}$ |
| Separator | |
| $-\varepsilon_s\,\omega\,c^{''}_{s,1}=\frac{\partial}{\partial x}\left[D_{eff,s}\frac{\partial c^{'}_{s,1}}{\partial x}\right]$<br>$\varepsilon_s\,\omega\,c^{'}_{s,1}=\frac{\partial}{\partial x}\left[D_{eff,s}\frac{\partial c^{''}_{s,1}}{\partial x}\right]$ | At x=$l_n$<br>$c^{'}_{n,1}=c^{'}_{s,1}$<br>$c^{''}_{n,1}=c^{''}_{s,1}$<br>At x=$l_n$+$l_s$ |

| | |
|---|---|
| | $c'_{s,1}=c'_{p,1}$<br>$c''_{s,1}=c''_{p,1}$ |
| $\frac{d}{dx}\left[\overline{\kappa}_{eff,s,0}\frac{d\Phi'_{s,1}}{dx}+\left.\frac{d\kappa_{eff,s}}{dc_s}\right\vert_{c_s=\overline{c}_{s,0}}c'_{s,1}\frac{d\overline{\Phi}_{s,0}}{dx}\right]$<br>$=\frac{d}{dx}\left[\frac{2\,\overline{\kappa}_{eff,s,0}\,R\,T\,(1-t_+)}{F}\left\{\frac{1}{\overline{c}_{s,0}}\frac{dc'_{s,1}}{dx}-\frac{c'_{s,1}}{\overline{c}_{s,0}^{2}}\frac{d\overline{c}_{s,0}}{dx}\right\}+\frac{2RT(1-t_+)}{F}\left.\frac{d\kappa_{eff,s}}{dc_s}\right\vert_{c_s=\overline{c}_{s,0}}\frac{c'_{s,1}}{\overline{c}_{s,0}}\frac{d\overline{c}_{s,0}}{dx}\right]$<br>$\frac{d}{dx}\left[\overline{\kappa}_{eff,s,0}\frac{d\Phi''_{s,1}}{dx}+\left.\frac{d\kappa_{eff,s}}{dc_s}\right\vert_{c_s=\overline{c}_{s,0}}c''_{s,1}\frac{d\overline{\Phi}_{s,0}}{dx}\right]$<br>$=\frac{d}{dx}\left[\frac{2\,\overline{\kappa}_{eff,s,0}\,R\,T\,(1-t_+)}{F}\left\{\frac{1}{\overline{c}_{s,0}}\frac{dc''_{s,1}}{dx}-\frac{c''_{s,1}}{\overline{c}_{s,0}^{2}}\frac{d\overline{c}_{s,0}}{dx}\right\}+\frac{2RT(1-t_+)}{F}\left.\frac{d\kappa_{eff,s}}{dc_s}\right\vert_{c_s=\overline{c}_{s,0}}\frac{c''_{s,1}}{\overline{c}_{s,0}}\frac{d\overline{c}_{s,0}}{dx}\right]$ | At x=$l_n$<br>$\Phi'_{n,1}=\Phi'_{s,1}$<br>$\Phi''_{n,1}=\Phi''_{s,1}$<br>At x=$l_n+l_s$<br>$\Phi'_{s,1}=\Phi'_{p,1}$<br>$\Phi''_{s,1}=\Phi''_{p,1}$ |
| Positive Electrode | |
| $-\varepsilon_p\,\omega\,c''_{p,1}=\frac{\partial}{\partial x}\left[D_{eff,p}\frac{\partial c'_{p,1}}{\partial x}\right]+a_p\,(1-t_+)\,j'_{f,p,1}-\frac{a_p\,C_{dl,p}\,(1-t_+)}{F}\omega[\Phi^{s''}_{p,1}-\Phi''_{p,1}]$<br>$\varepsilon_p\,\omega\,c'_{p,1}=\frac{\partial}{\partial x}\left[D_{eff,p}\frac{\partial c''_{p,1}}{\partial x}\right]+a_p\,(1-t_+)\,j''_{f,p,1}+\frac{a_p\,C_{dl,p}\,(1-t_+)}{F}\omega[\Phi^{s'}_{p,1}-\Phi'_{p,1}]$ | At x=$l_n+l_s$<br>$-D_{eff,s}\frac{\partial c'_{s,1}}{\partial x}=-D_{eff,p}\frac{\partial c'_{p,1}}{\partial x}$<br>$-D_{eff,s}\frac{\partial c''_{s,1}}{\partial x}=-D_{eff,p}\frac{\partial c''_{p,1}}{\partial x}$<br>At x=$l_n+l_s+l_p$<br>$\frac{\partial c'_{p,1}}{\partial x}=0$<br>$\frac{\partial c''_{p,1}}{\partial x}=0$ |
| $\frac{\partial}{\partial x}\left[\sigma_{eff,p}\frac{\partial\Phi^{s'}_{p,1}}{\partial x}\right]+\frac{\partial}{\partial x}\left[\overline{\kappa}_{eff,p,0}\frac{\partial\Phi'_{p,1}}{\partial x}+\left.\frac{\partial\kappa_{eff,p}}{\partial c_p}\right\vert_{c_p=\overline{c}_{p,0}}c'_{p,1}\frac{\partial\overline{\Phi}_{p,0}}{\partial x}\right]$<br>$=\frac{\partial}{\partial x}\left[\frac{2\,\overline{\kappa}_{eff,p,0}\,R\,T\,(1-t_+)}{F}\left\{\frac{1}{\overline{c}_{p,0}}\frac{\partial c'_{p,1}}{\partial x}-\frac{c'_{p,1}}{\overline{c}_{p,0}^{2}}\frac{\partial\overline{c}_{p,0}}{\partial x}\right\}+\frac{2RT(1-t_+)}{F}\left.\frac{\partial\kappa_{eff,p}}{\partial c_p}\right\vert_{c_p=\overline{c}_{p,0}}\frac{c'_{p,1}}{\overline{c}_{p,0}}\frac{\partial\overline{c}_{p,0}}{\partial x}\right]$<br>$\frac{\partial}{\partial x}\left[\sigma_{eff,p}\frac{\partial\Phi^{s''}_{p,1}}{\partial x}\right]+\frac{\partial}{\partial x}\left[\overline{\kappa}_{eff,p,0}\frac{\partial\Phi''_{p,1}}{\partial x}+\left.\frac{\partial\kappa_{eff,p}}{\partial c_p}\right\vert_{c_p=\overline{c}_{p,0}}c''_{p,1}\frac{\partial\overline{\Phi}_{p,0}}{\partial x}\right]$<br>$=\frac{\partial}{\partial x}\left[\frac{2\,\overline{\kappa}_{eff,p,0}\,R\,T\,(1-t_+)}{F}\left\{\frac{1}{\overline{c}_{p,0}}\frac{\partial c''_{p,1}}{\partial x}-\frac{c''_{p,1}}{\overline{c}_{p,0}^{2}}\frac{\partial\overline{c}_{p,0}}{\partial x}\right\}+\frac{2RT(1-t_+)}{F}\left.\frac{\partial\kappa_{eff,p}}{\partial c_p}\right\vert_{c_p=\overline{c}_{p,0}}\frac{c''_{p,1}}{\overline{c}_{p,0}}\frac{\partial\overline{c}_{p,0}}{\partial x}\right]$ | At x=$l_n+l_s$<br>$\overline{\kappa}_{eff,s,0}\frac{\partial\Phi'_{s,1}}{\partial x}+\left.\frac{\partial\kappa_{eff,s}}{\partial c_s}\right\vert_{c_s=\overline{c}_{s,0}}c'_{s,1}\frac{\partial\overline{\Phi}_{s,0}}{\partial x}$<br>$=\overline{\kappa}_{eff,p,0}\frac{\partial\Phi'_{p,1}}{\partial x}+\left.\frac{\partial\kappa_{eff,p}}{\partial c_p}\right\vert_{c_p=\overline{c}_{p,0}}c'_{p,1}\frac{\partial\overline{\Phi}_{p,0}}{\partial x}$<br>$\overline{\kappa}_{eff,s,0}\frac{\partial\Phi''_{s,1}}{\partial x}+\left.\frac{\partial\kappa_{eff,s}}{\partial c_s}\right\vert_{c_s=\overline{c}_{s,0}}c''_{s,1}\frac{\partial\overline{\Phi}_{s,0}}{\partial x}$<br>$=\overline{\kappa}_{eff,p,0}\frac{\partial\Phi''_{p,1}}{\partial x}+\left.\frac{\partial\kappa_{eff,p}}{\partial c_p}\right\vert_{c_p=\overline{c}_{p,0}}c''_{p,1}\frac{\partial\overline{\Phi}_{p,0}}{\partial x}$<br>At x=$l_n+l_s+l_p$<br>$\frac{\partial\Phi'_{p,1}}{\partial x}=0$<br>$\frac{\partial\Phi''_{p,1}}{\partial x}=0$ |
| $\frac{\partial}{\partial x}\left[\sigma_{eff,p}\frac{\partial\Phi^{s'}_{p,1}}{\partial x}\right]=a_p\,F\,j'_{f,p,1}-a_p\,C_{dl,p}\omega[\Phi^{s''}_{p,1}-\Phi''_{p,1}]$ | At x=$l_n+l_s$ |

| | |
|---|---|
| $\frac{\partial}{\partial x}\left[\sigma_{eff,p}\frac{\partial \Phi^{s''}_{p,1}}{\partial x}\right]=a_p\ F\ j^{''}_{f,p,1}+a_p\ C_{dl,p}\omega[\Phi^{s'}_{p,1}-\Phi^{'}_{p,1}]$ | $\frac{\partial \Phi^{s'}_{p,1}}{\partial x}=0$<br>$\frac{\partial \Phi^{s''}_{p,1}}{\partial x}=0$<br>At x=$l_n$+$l_s$+$l_p$<br>$\frac{\partial \Phi^{s'}_{p,1}}{\partial x}=-\frac{I_{app}}{\sigma_{eff,p}}$<br>$\frac{\partial \Phi^{s''}_{p,1}}{\partial x}=0$ |
| $-\omega\, c^{s''}_{p,1}=\frac{1}{r^2}\frac{\partial}{\partial r}\left[r^2 D^s_p\frac{\partial c^{s'}_{p,1}}{\partial r}\right]$<br>$\omega\, c^{s'}_{p,1}=\frac{1}{r^2}\frac{\partial}{\partial r}\left[r^2 D^s_p\frac{\partial c^{s''}_{p,1}}{\partial r}\right]$ | At r=0<br>$\frac{\partial c^{s'}_{p,1}}{\partial r}=0$<br>$\frac{\partial c^{s''}_{p,1}}{\partial r}=0$<br>At r=$R_p$<br>$-D^s_p\frac{\partial c^{s'}_{p,1}}{\partial r}=j^{'}_{f,p,1}$<br>$-D^s_p\frac{\partial c^{s''}_{p,1}}{\partial r}=j^{''}_{f,p,1}$ |

***Table 5.8 Additional Equations – Modified Frequency Domain Specific***

All subscripts *i* refer to *n* or *p*.

$$\overline{\kappa_{eff,i,0}}=\kappa_{eff,i}\Big|_{c_i=\overline{c_{i,0}}}$$

$$j^{'}_{f,i,1}=\frac{i0^{'}_{i,1}}{F}\left[\exp\left(\frac{\alpha_{a,i}F}{RT}\overline{\eta_{i,0}}\right)-\exp\left(\frac{-\alpha_{c,i}F}{RT}\overline{\eta_{i,0}}\right)\right]+\frac{\overline{i0_{i,0}}}{F}\left[\frac{\alpha_{a,i}F}{RT}\exp\left(\frac{\alpha_{a,i}F}{RT}\overline{\eta_{i,0}}\right)\eta^{'}_{i,1}+\frac{\alpha_{c,i}F}{RT}\exp\left(\frac{-\alpha_{c,i}F}{RT}\overline{\eta_{i,0}}\right)\eta^{'}_{i,1}\right]$$

$$j^{''}_{f,i,1}=\frac{i0^{''}_{i,1}}{F}\left[\exp\left(\frac{\alpha_{a,i}F}{RT}\overline{\eta_{i,0}}\right)-\exp\left(\frac{-\alpha_{c,i}F}{RT}\overline{\eta_{i,0}}\right)\right]+\frac{\overline{i0_{i,0}}}{F}\left[\frac{\alpha_{a,i}F}{RT}\exp\left(\frac{\alpha_{a,i}F}{RT}\overline{\eta_{i,0}}\right)\eta^{''}_{i,1}+\frac{\alpha_{c,i}F}{RT}\exp\left(\frac{-\alpha_{c,i}F}{RT}\overline{\eta_{i,0}}\right)\eta^{''}_{i,1}\right]$$

$$\overline{\eta_{i,0}}=\overline{\Phi^s_{i,0}}-\overline{\Phi_{i,0}}-U_i$$

$$\eta^{'}_{i,1}=\Phi^{s'}_{i,1}-\Phi^{'}_{i,1}-\frac{dU_i}{dc^s_{i,surf}}\Bigg|_{c^s_{i,surf}=\overline{c^s_{i,surf,0}}}c^{s'}_{i,surf,1}$$

$$\eta^{''}_{i,1}=\Phi^{s''}_{i,1}-\Phi^{''}_{i,1}-\frac{dU_i}{dc^s_{i,surf}}\Bigg|_{c^s_{i,surf}=\overline{c^s_{i,surf,0}}}c^{s''}_{i,surf,1}$$

$$\overline{i0_{i,0}}=Fk_i(c^s_{i,max}-\overline{c^s_{i,surf,0}})^{\alpha_{a,i}}(\overline{c_{i,0}})^{\alpha_{a,i}}(\overline{c^s_{i,surf,0}})^{\alpha_{c,i}}$$

$$i0_{i,1}^{'} = \left.\frac{\partial i0_i}{\partial c_i}\right|_{c_i = \overline{c_{i,0}},\, c_{i,surf}^s = \overline{c_{i,surf,0}^s}} c_{i,1}^{'} + \left.\frac{\partial i0_i}{\partial c_{i,surf}^s}\right|_{c_i = \overline{c_{i,0}},\, c_{i,surf}^s = \overline{c_{i,surf,0}^s}} c_{i,surf,1}^{s'}$$

$$i0_{i,1}^{''} = \left.\frac{\partial i0_i}{\partial c_i}\right|_{c_i = \overline{c_{i,0}},\, c_{i,surf}^s = \overline{c_{i,surf,0}^s}} c_{i,1}^{''} + \left.\frac{\partial i0_i}{\partial c_{i,surf}^s}\right|_{c_i = \overline{c_{i,0}},\, c_{i,surf}^s = \overline{c_{i,surf,0}^s}} c_{i,surf,1}^{s''}$$

### *Computation details*

For the brute force approach, the time domain equations were defined and solved in *Maple* with its inbuilt call to a compiled environment (C). For each simulation, the inputs are battery parameters and a perturbation current, and the output is the voltage response. Signal processing on the output voltage response was then carried out using python with the STFT performed using scipy's fftpack to obtain the impedance. For the time-separated approach, both the time domain DC model and modified frequency domain DEIS model are solved hierarchically in *Maple*. The local computing resource for all of the battery simulation work reported here was *Maple 14* classic worksheet environment operating on an Intel® Core™ i7-7700K CPU @ 4.20GHz with 64 GB RAM. It is expected that all the simulations would be at least an order of magnitude faster in a C environment.

Throughout the paper, SEIS and DEIS spectra are compared at the same SOCs. We use a practical reference for defining SOC, akin to how an experimentalist would report it, where the 0% and 100% reference states are determined (numerically) based on a C/20 discharge with voltage cut-offs. In particular, 100% SOC is the total moles/m$^2$ of intercalated lithium in the negative electrode at a cell voltage of 4.2V, and 0% SOC is the total moles/m$^2$ of intercalated lithium at a cell voltage of 2.5V while undergoing a C/20 discharge. Because dynamic experiments can have appreciable spatial variations of transported species, the total moles of intercalated lithium are determined by integrating across the particle radii and thickness of the negative electrode solid phase. Subsequently, under any charge or discharge conditions, the cited SOC is from the spatially integrated total moles per unit area of intercalated lithium, relative to the reference values. SOC values reported for SEIS measurements have the same total intercalated lithium as their DEIS counterpart, but with an equilibrated spatially uniform distribution of lithium across the cell.

## 5.3 Results and Discussion

*Simulations using the brute force method*

***Figure 5.1*** shows a voltage-time discharge curve simulated using the brute force method, with the large circle marker referencing the battery discharge time point $t_b$ for the voltage and current density shown in the inset. The lower inset in ***Figure 5.1*** shows 4 cycles of the input current density with a mean DC value of $I_0 = 29$ A/m$^2$, corresponding to a 1C discharge rate, and four cycles of the oscillating AC current density with amplitude $\Delta I = 0.58$ A/m$^2$ and frequency $\omega_1 = 1$ Hz. The time window is centered at $t_b = 366$s with a local timescale width of $\Delta t_{EIS} = 4$s. The upper inset is the voltage output over the same time period, which has a modulation amplitude of about ±2 mV around the DC voltage background of roughly 3.870 V; voltage modulations of this size fall in a range that is generally considered linear response for EIS measurements. Even though the local measurement timescale is only 4 seconds, one can see the nonstationarity of the voltage underlying the oscillating voltage component.

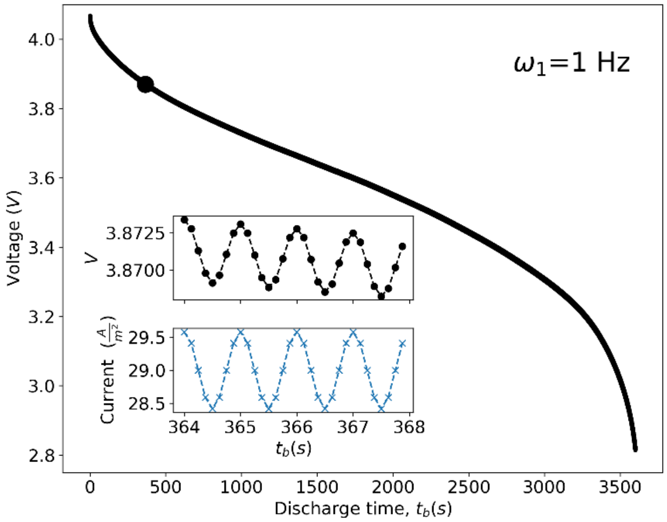

***Figure 5.1 Simulated voltage response for 1C discharge using the brute force time domain method. Large circle marker corresponds to time shown in insets. Insets show window centered at $t_b = 366$s with total local timescale width of $\Delta t_{EIS} = 4$s, for the voltage response and input current density with perturbations at $\omega_1 = 1$ Hz.***

***Figure 5.2*** (a)-(c) are detailed plots showing 4 cycles of the current density and voltage signals near the start, middle, and end of a 1C discharge ($t_b$ = 366s, 1828s, and 3291s respectively), corresponding to 90%, 50%, and 10% SOC, respectively. The pure DC baseline voltage associated with a mean DC current density of $I_0$ = 29 A/m$^2$ (without perturbations, $\Delta I=0$) is plotted as the black line running through the oscillating voltages. Note that the baseline is approximately linear over 4 cycles for a 1 Hz signal, with the DC baseline voltage gradients being greater at the start and end of discharge than in the middle, as the discharge curve in ***Figure 5.1*** shows globally.

***Figure 5.2*** (d)-(i) are the frequency domain voltage spectra associated with the FFT of each 4 second data window (black line). The real voltage spectra show the expected signal at the oscillation frequency of 1 Hz, as well as the (off-scale) mean DC voltage at zero frequency. The order of magnitude smaller imaginary voltage spectra at 1 Hz sit on top of a spectral background that scales as $\sim O(\omega^{-1})$, effectively the FFT of background from the linearly sloping time domain baseline. Baseline subtraction is simple here because we have the computed DC signal (solid lines) as well as the AC+DC signal over the entire windowed period, allowing quantitative baseline subtraction in either the time or frequency domain. The result of time domain baseline subtraction, followed by FFT, is presented in ***Figure 5.2*** (d)-(i) as the red filled circles, where the real and imaginary voltage spectra now have negligible background. Quantitative baseline subtraction like this can be much more difficult in DEIS experiments, where the underlying nonstationary DC voltage must be estimated rather than computed.[123,124]

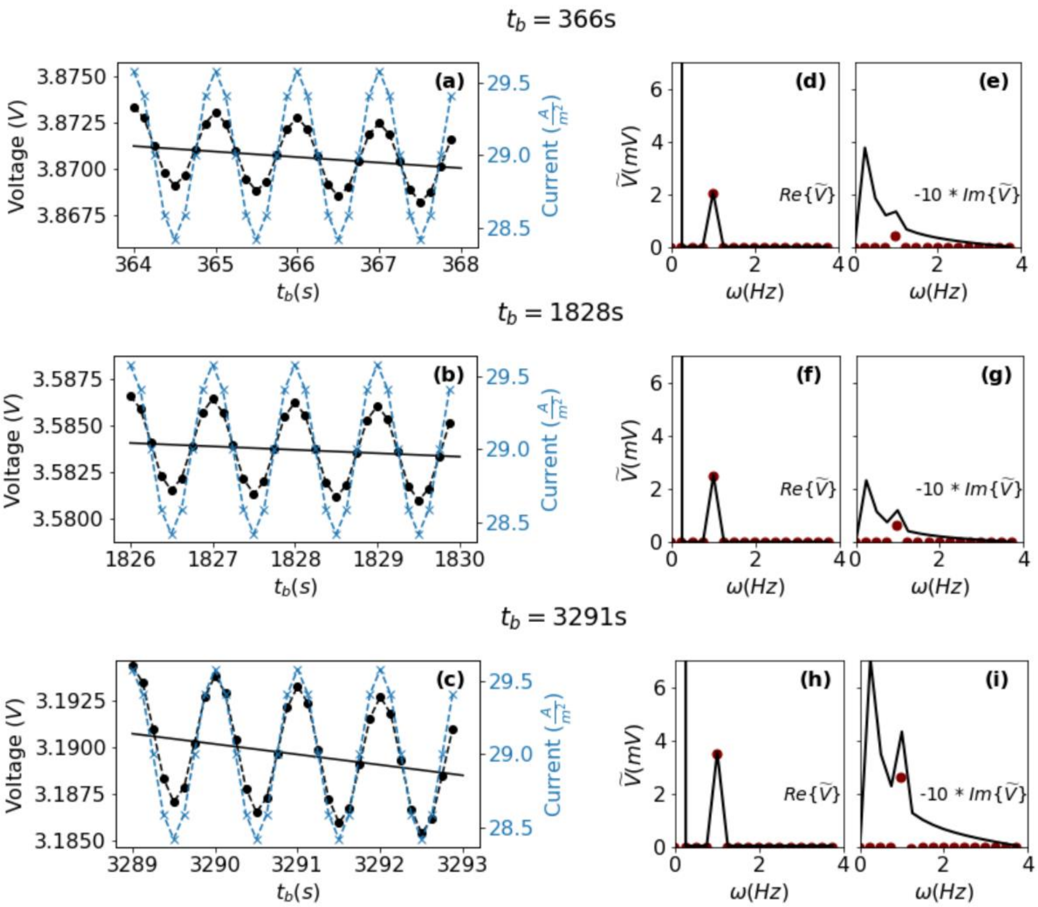

***Figure 5.2 (a)-(c) Time domain data at different 1C discharge times for 1 Hz perturbations. The black line is the underlying nonstationary DC voltage response. (d)-(i) Frequency domain data at the corresponding times of discharge, showing real (d, f, h) and imaginary (e, g, i) components. Lines in (d)-(i) represent FFT of corresponding time domain voltage response. Circles in (d)-(i) represent FFT of corresponding time domain voltage response that has baseline DC voltage subtracted. Note the change in magnitude of units from V to mV in time to frequency domain, and the -10x multiplication of imaginary spectra.***

The baseline subtracted voltage spectra and current spectra for every discharge time of interest is used to compute the impedance at the particular frequency under study. For example, the voltage spectrum at 1 Hz and $t_b$= 366s produces a complex voltage of $V_1(\omega = 1Hz; t_b = 366s)$ = (2.05 – 0.05j) mV, and $I_1(\omega = 1Hz; t_b = 366s)$ = (0.58 + 0.00j) A/m$^2$. The complex ratio of $V_1$ to $I_1$ gives

$Z_1(\omega = 1\,Hz; t_b = 366s) = (3.54 - 0.08j)\,m\Omega - m^2$. The real and imaginary components of this impedance value at $t_b$ = 366s are plotted as red square markers in ***Figure 5.3*** (a) and (b). This process is repeated for every second of the simulated battery's discharge using a 1 Hz diagnostic signal as shown in ***Figure 5.3*** (a) and (b). To find the DEIS at a different frequency, we repeat this brute force time domain calculation using the next frequency of interest. As modulation frequency increases, the number of time points that must be computed increases proportionately in order to keep the Nyquist frequency fixed at 4 times larger than the input AC component.

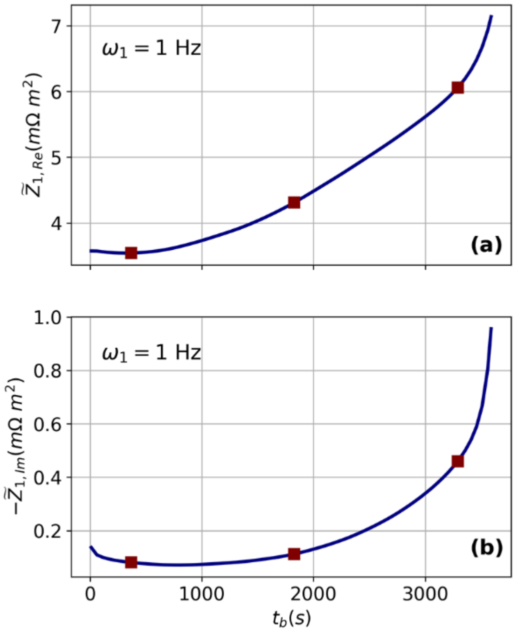

***Figure 5.3 Real (a) and imaginary (b) dynamic impedance response for 1C discharge at 1 Hz. Red square markers correspond to tb = 366s, 1828s, and 3291s calculated from data shown in previous figure.***

### *Simulations using the time-separated method*

Using the time-separated method, we can simulate the dynamic impedance at all frequencies and at any point in time as the battery is charging or discharging. ***Figure 5.4*** shows the DEIS for $\omega_1$ =

10 kHz to 3.98 mHz, with 10 points per frequency decade, at the same three times of a 1C discharge $t_b$ = 366s, 1828s, and 3291s. This corresponds to 90%, 50%, and 10% SOCs respectively.

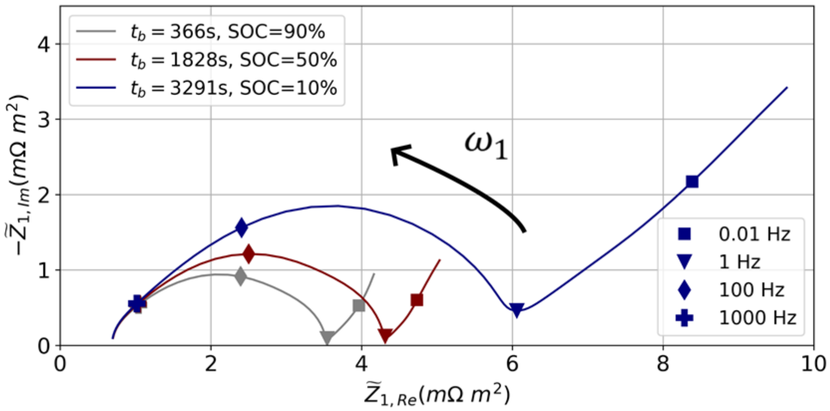

***Figure 5.4 Nyquist plots of DEIS spectra at three different 1C discharge times, corresponding to 90%, 50%, and 10% states-of-charge. These spectra were simulated using the time-separated method.***

These DEIS simulations leverage the fact that processes are happening on two different timescales. The time domain model is first used to simulate the overall system dynamics, in this case, the DC discharge of the battery, which is on the longer $t_b$ timescale of $10^3$ – $10^5$ s. The frequency domain model is used to simulate the impedance values on the shorter t' timescale of $10^{-3}$ – $10^3$ s. When the two timescales are orders of magnitudes apart, we can assume that the system is pseudo-stationary and the time separated method is likely to be accurate. In contrast, as the AC and DC timescales begin to converge (at high C-rates and low frequencies), one must be more cautious using this method.

*Computation time*

For comparison of both methods, we report the time to compute the DEIS signal for an entire charge or discharge curve. The brute force method requires solving the governing equations and sampling at many time steps (8 points per oscillation cycle) to accurately simulate a sinusoidal perturbation and perform JTFA, thus the number of points (and hence, computation time) increases with frequency. Frequencies above 10 Hz become increasingly impractical for the brute force method without additional computing resources. The time-separated method is more computationally efficient and takes ~25 seconds to simulate a 1C DC charge curve, sampling $t_b$ every second and storing the solutions needed to compute the subsequent DEIS spectra. These DC solutions are used in the frequency domain equations which take ~24 milliseconds to compute a single frequency, with little dependence on the frequency being analyzed.

Here we compare the computational times of the two approaches using an example. A 1 Hz DEIS signal is sensitive to the effective charge transfer resistance of the cell and may be useful for understanding charging processes (as is discussed in more detail later). The brute force approach to compute the JTFA at 1 Hz for an entire charging curve, with 1 second temporal resolution, would take 1.2 hours. This computation is longer than the actual real time experiment. In contrast, the time-separated method would take 0.03 hours to compute. This is 3% of the time taken to run the 1C experiment and would therefore be a suitable diagnostic signal for model-based real time control.

Simulations were carried out using direct simulation with Maple's numeric dsolve command with a MinGW compiler. We can expect an order of magnitude faster computation if the same equations are solved in a direct C environment with Sundials and optimized solvers in time. We also expect a leaner memory footprint of at least 1-2 orders of magnitude. The hardware requirements might determine the accuracy of the method that can be implemented for a particular frequency. In our earlier work, we reported accuracy and convergence analysis where higher frequencies require higher number of collocation points for convergence.[146] For a lower number of collocation points, the memory requirement is minimal. The objective of this paper is to build on and use a convenient version of our past reformulated models and codes for discharge curves and impedance models to perform DEIS. There is a lot of scope of improvement in CPU time. Replacing Legendre polynomials with Chebyshev polynomials will require a greater number of terms and equations, but FFT can be directly applied for Chebyshev collocation, thus enabling extremely fast simulation for discharge curves provided boundary symmetry is maintained in the coefficient matrix. In addition, adaptive spectral methods (using and modifying polynomial order in cathode/anode/separator/time and with frequency) can yield much faster results.

### *Comparison of the two methods*

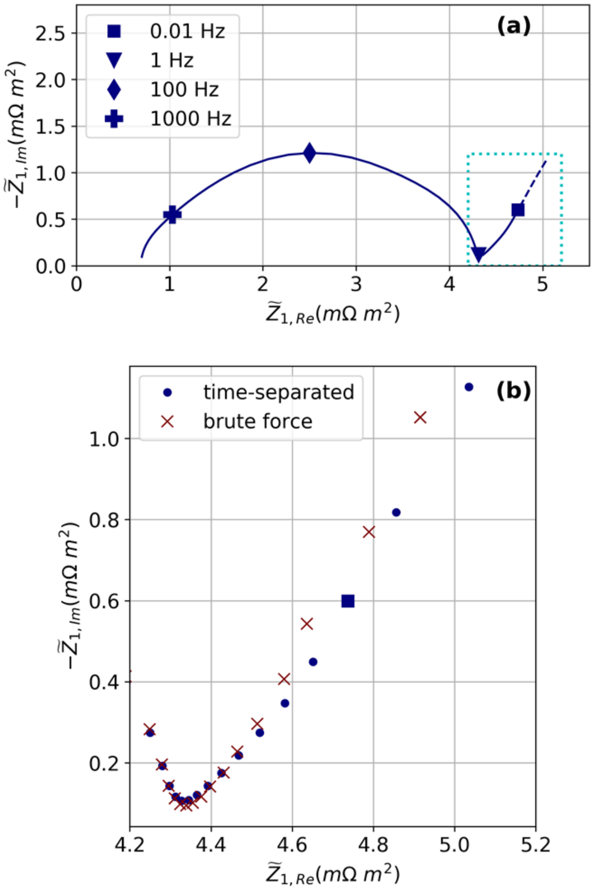

***Figure 5.5 Evaluating frequencies where the time-separated method and brute force methods converge. (a) DEIS spectrum during 1C discharge at $t_b$=1828s, SOC=50%, simulated using the time-separated method. Light blue dotted box is shown in (b) with dynamic impedances computed using both the time-separated method (blue circles and square) and brute force method (red crosses). At frequencies equal to, and above the 0.1 Hz point denoted by the square symbol, the two methods have a relative difference less than 2% and are considered converged. Regions with better than 2% convergence are denoted by solid curves in subsequent time-separated DEIS spectrum, whereas regions of lower confidence are presented as dashed curves, as illustrated in part (a).***

We compare DEIS spectra simulated using the brute force method and the time-separated method to identify the critical frequencies above which the time-separated method is accurate.

***Figure 5.5***(a) shows the entire DEIS spectrum simulated by the time-separated method for 1C discharge, at $t_b$=1828s and SOC=50%. The area in the blue dotted box is examined more carefully in ***Figure 5.5***(b) and compared to impedance simulated using the brute force method. We observe that as frequency decreases, the impedance values calculated using the two different methods increasingly diverge. We explore the reasons for this divergence in detail in the Supplementary Material. To quantify the quality of agreement at each frequency, we define the relative difference between the brute force (subscript a) and time-separated DEIS values (subscript b) as the difference in the magnitude divided by the mean magnitude,

$$\frac{2\sqrt{[Z_a^{'}-Z_b^{'}]^2+[Z_a^{''}-Z_b^{''}]^2}}{\sqrt{[Z_a^{'}]^2+[Z_a^{''}]^2}+\sqrt{[Z_b^{'}]^2+[Z_b^{''}]^2}}*100 \tag{5.3}$$

at any given frequency. Converged results are defined here as a 2% or less relative difference; we denote all converged frequencies with a solid line in time-separated DEIS spectra. In contrast, the frequencies with greater than 2% divergence in methods are shown with a dashed line, as in ***Figure 5.5***(a). The square symbols in ***Figure 5.5***(a) and (b), represent the lowest frequency that is converged, or the critical frequency, where the difference in the impedance of the two methods is within 2%. Of course, we can efficiently compute time-separated spectra at frequencies below this critical frequency, but violation of the underlying time-separated assumptions impacts the quality of the solution. For this figure with a 1C discharge, the lowest converged frequency is at $\omega_1$= 0.01 Hz.

### *Comparing DEIS and SEIS for charging and discharging cells*

Using the time-separated method, we compute the DEIS spectra at 0.5C and 1C for both charging in ***Figure 5.6***(a) and discharging in ***Figure 5.6***(b), and compare these to the SEIS spectrum at the same SOC of 10%. Despite quantitative differences in the spectra, which we discuss below, the DEIS and SEIS spectra share many basic qualitative features. At high frequencies, above 1000 Hz, all curves converge to nearly identical ohmic limiting behavior. At intermediate frequencies, between roughly 1 Hz and the high frequency ohmic limit, a flattened impedance arc is seen for the interfacial processes (charge transfer and capacitive currents) in the porous electrodes. As frequencies go below 1 Hz, all spectra show a low frequency thermo-diffusion Warburg-like impedance region.

Deviations between the SEIS and DEIS spectra, and the frequency regime where the deviations occur, provide insights into the cell gradients caused by passing current. For example, the two DEIS spectra in ***Figure 5.6***(a) began their charging cycles as relaxed cells with uniform composition at 0% SOC. The 10% SOC condition is achieved after roughly 6 minutes of charging at 1C or 12 minutes at 0.5C. At this SOC, intercalated lithium gradients are beginning to form within solid particles and through the depth of both porous electrodes, and lithium-ion gradients are beginning to form in the electrolyte. ***Figure 5.6***(a) shows that most of the difference between the SEIS and DEIS spectra occur within the interfacial charge transfer region (between 1 Hz and 1000 Hz). The high frequency ohmic limit (above 1000 Hz) is largely unchanged, and the Warburg-like low frequency region is displaced, but not much changed between DEIS and SEIS. The fact that the impedance in the interfacial region is lower for DEIS than SEIS, and primarily centered on frequencies dominated by interfacial processes, suggests that kinetics in one or both electrodes are improved by the intercalated lithium gradients.

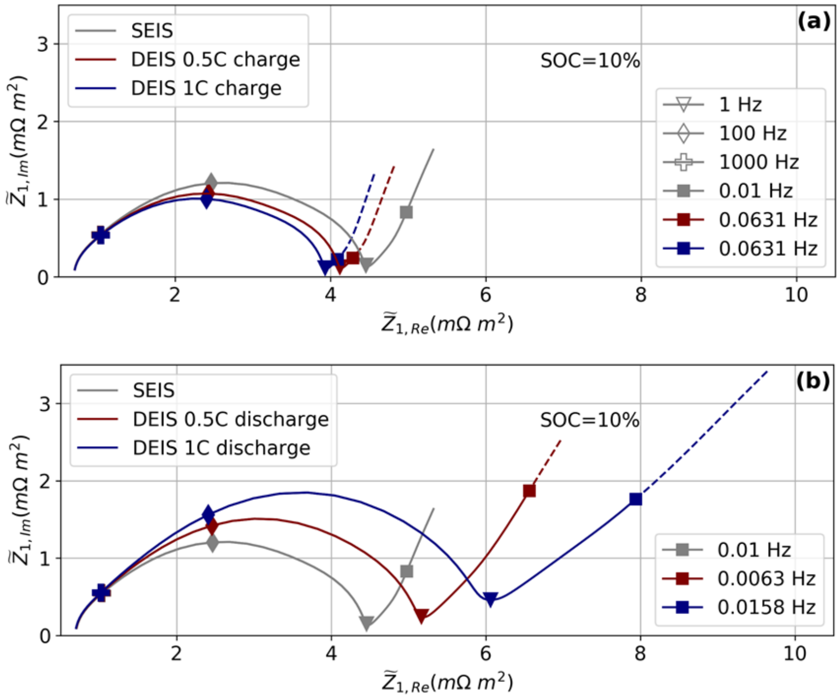

***Figure 5.6 Comparison of DEIS to SEIS at SOC=10% during 0.5C and 1C (a) charge and (b) discharge. Marker shape in the legend show common frequencies for the respective marker shapes in SEIS and DEIS. Converged frequencies for DEIS are separately labeled.***

***Figure 5.6***(b) compares DEIS and SEIS for the same 10% SOC overall as in ***Figure 5.6***(a), but the DEIS spectra were achieved by discharging the cell for about 54 minutes (at 1C rate) or roughly double that (at 0.5C rate) from an initially relaxed 100% SOC condition. Significant growth in the DEIS interfacial arc between 1 Hz and 1000 Hz is seen compared to SEIS. The larger DEIS interfacial arc width implies that accumulated lithium intercalation gradients in the solid state and in the electrolyte significantly degrade the charge transfer kinetics in one or both electrodes at this SOC during discharge. This is opposite to the improved kinetics seen at the same SOC for a charging cell. The Warburg-like low frequency regions below 1 Hz now also shows subtle differences between the SEIS, 0.5C DEIS and 1C DEIS spectra. In particular, the nearly constant phase angle of the Warburg-like region gets smaller with increasing DC current.

The DEIS curves shown in ***Figure 5.6***(b) have been under a constant DC discharge for more than 50 minutes (1 C curve) or nearly 2 hours (0.5C), enabling substantial gradients to be established throughout the cell. Thus, it is not surprising to see a bigger deviation between DEIS and SEIS for the discharge case than the short-time charge in ***Figure 5.6***(a). As noted, the influence of this non-equilibrium state is reflected in the width of the interfacial region, found by subtracting the high frequency ohmic intercept from the extrapolated real axis intercept near the 1 Hz marker. In particular, the relaxed SEIS spectrum interfacial processes arc width is around 4 mΩ-m$^2$, and that can be compared to a nearly 6 mΩ-m$^2$ width in the 1C DEIS discharge spectrum. The 0.5C discharge falls between the SEIS and 1C DEIS spectra. We explore the physicochemical origins of dynamical effects on the DEIS spectra more thoroughly below, emphasizing the changes we see interfacial charge transfer processes under dynamic operation, rather than the thermo-diffusion Warburg-like processes.

We also note that ohmic resistance is determined by length of the electrodes and separator, ionic, and electronic conductivities. Both ionic and electronic conductivities are a function of concentration of lithium-ions in their respective phases (though in this work, only ionic conductivity is modeled as a function of concentration). Under high-rate conditions, where there can be appreciable gradients in both solid and electrolyte concentrations across the cell sandwich, nonlinearity in conductivity coefficients can drive deviations from stationary behavior that show up at high frequencies.

*Comparing SEIS and DEIS for charging and discharging across SOCs*

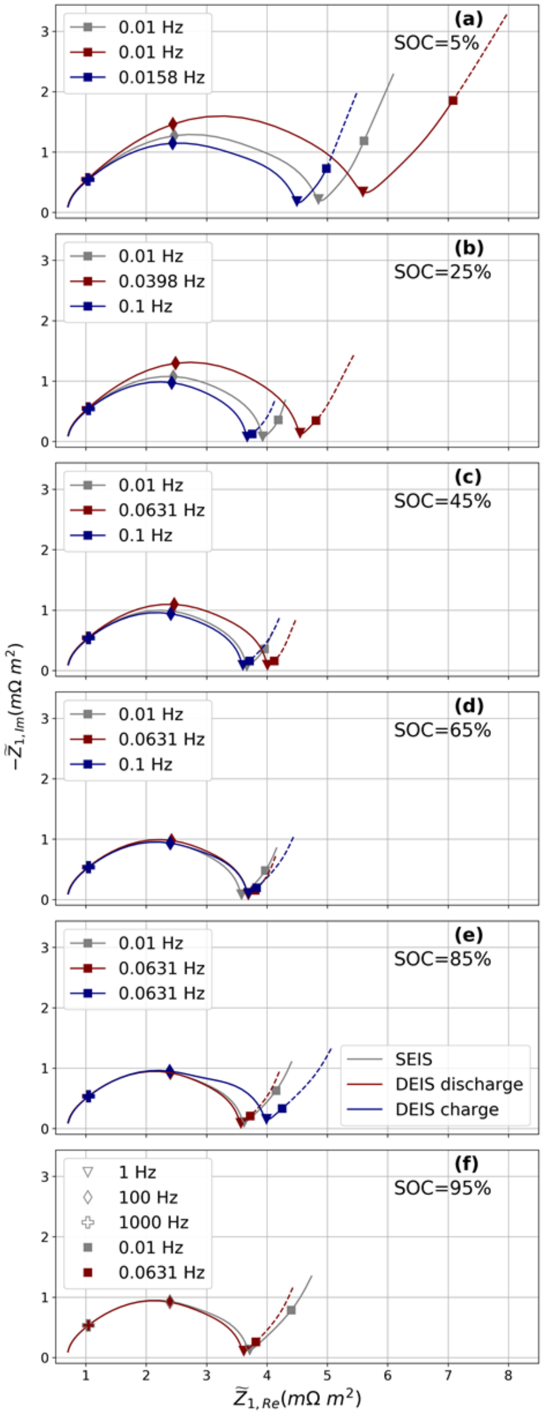

***Figure 5.7 Sequence of DEIS spectra at the same set of SOCs of: (a) 5%, (b) 25%, (c) 45%, (d) 65%, (e) 85% (f) 95% for 0.5C charging (blue curves and symbols) and 0.5C discharging (red curves and symbols) compared to SEIS at the same relaxed SOCs (gray curves and symbols).***

A series of DEIS spectra for charging and discharging at 0.5C are compared to SEIS spectra for various SOCs in ***Figure 5.7***(a)-(f). As the relaxed 0% SOC cell is charged at 0.5C, the 5% SOC DEIS spectrum (a) shows low impedances compared to SEIS at frequencies below 1000 Hz. As charging continues, the SEIS (gray) and DEIS spectra (blue) are seen to cross between 45%<SOC<65%, at which point the charging DEIS impedances are greater than SEIS impedances, c.f. ***Figure 5.7***(c) and (d). At 85% SOC the impedance has grown appreciably below 100 Hz in the DEIS spectrum, ***Figure 5.7***(e). Because the 0.5C charging reaches the specified 4.2V cut-off voltage prior to achieving 95% SOC, there is no charging DEIS spectrum in ***Figure 5.7***(f).

The 0.5C discharge spectra in ***Figure 5.7***(a)-(f) all started from a relaxed 100% charged cell. One can see at the very beginning of discharge, the 95% SOC DEIS spectrum (***Figure 5.7***(f), red curve) is close to the SEIS spectrum, though with a little lower impedance at frequencies below 100 Hz. As discharge continues the DEIS spectrum grows toward (***Figure 5.7***(e), red curve) and eventually exceeds the SEIS spectrum at 65% SOC (***Figure 5.7***(d), red curve). The discharge DEIS spectra continue to grow beyond the SEIS values as we continue down to 5% discharge in ***Figure 5.7***(f), red curve, where the impedance is significantly large at all frequencies outside of the high frequency limit.

It is common in experimental and modeling research on SEIS and DEIS spectra like those in ***Figure 5.7*** to be fit to equivalent circuit models to extract parameters.[132,134] Rather than convolute our results with a fit to an equivalent circuit model, we focus on the most notable changes as a function of SOC and dynamics, namely, the width of the interfacial processes arc, a spectral feature normally attributed to the overall charge transfer resistance of the cell. To estimate this effective charge transfer resistance (effective $R_{ct}$) from Nyquist plots like ***Figure 5.6*** and ***Figure 5.7*** we extrapolate the 5 impedance points at the high and low frequency ends of the interfacial processes arc until they intercept the real impedance axis, and subtract the values. The effective $R_{ct}$ for SEIS and DEIS spectra, while charging and discharging, are plotted as a function of SOC in ***Figure 5.8***.

It is challenging to interpret ***Figure 5.8*** based on a simple analytical form of the charge transfer resistance, because deviations between DEIS and SEIS effective charge transfer resistances are driven by the spatial distribution of intercalated lithium within any given solid particle and throughout the thickness of each porous electrode. The functional form of effective $R_{ct,i} = \frac{RT}{a_i l_i i0_i F}$ is derived from linearizing Butler-Volmer kinetics, and accounting for effective area of a porous electrode with the additional terms of $a_i$, specific surface area to volume ratio, and $l_i$, electrode length. In reality, $l_i$ is smaller for porous electrodes that are partially utilized to account for non-uniform reaction rates. The utilization ratio, introduced by Newman and Tobias,[148] is, at the lowest, 11% for the parameters used here. The reaction zones move through the electrode and varies with SOC. This non-uniform access to current gives a non-uniform exchange current density, $i0_i$. For steep gradients in electrode utilization, the two computational methods presented here does account for built-in gradients, but using a simple analytical $R_{ct}$ to interpret is challenging. Also, $i0_i$ is a function of concentration (defined in ***Table 5.8***), and lithium concentration varies spatially across the electrodes during a DEIS measurement. The $R_{ct}$ expression above has to be modified to include spatially varying concentrations. There is no easy analytical interpretation to relate $i0_i(x;t_b)$ to an overall $R_{ct,i}$ value and it is difficult to confidently rationalize how the interplay of stationary and dynamic processes in both electrodes add up to the complex, non-monotonic, and crossing behaviors seen in ***Figure 5.8***. Further analysis is beyond the scope of this work.

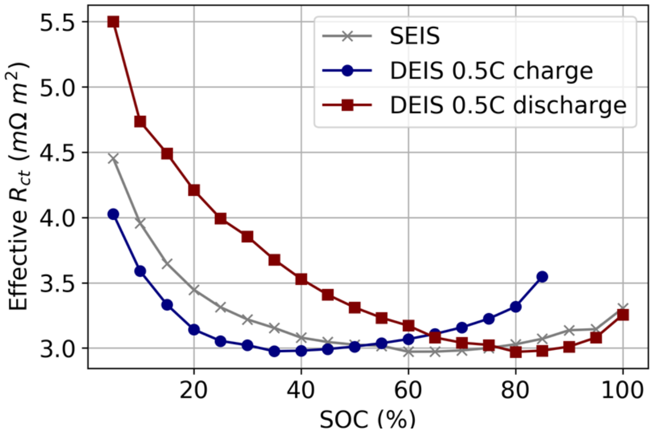

***Figure 5.8 Effective charge transfer resistance, $R_{ct}$, of the whole cell as a function of SOC during a 0.5C DEIS charge and discharge is compared to the relaxed SEIS values at each SOC.***

Nonetheless, it is worth digging into the origins of the behaviors seen in ***Figure 5.8***, because complexity in DEIS effective charge transfer resistance is a distinctive feature of experimental DEIS research. For example, experimental work done by Itagaki et al. with a three electrode $LiCoO_2$-graphite cell showed monotonically decreasing $R_{ct,i}$ with SOC for both electrodes.[132] The value of $R_{ct,p}$ was always greater during charging than discharging, whereas $R_{ct,n}$ was greater during discharging than charging. On the contrary, Huang et al. concluded that the overall effective dynamic $R_{ct}$ of the nickel-cobalt-manganese 18650 commercial cell being tested was smaller during charging than discharging mainly because the dynamic $R_{ct,p}$ was smaller.[134] Our physics-based time-separated approach can be used to shed insight on the contributions to effective charge transfer resistance during dynamic operation.

### *Explore physics more completely when several processes may be dominant*

Exploring the physics that drives differences between SEIS and DEIS spectra is quite straight forward for our time-separated DEIS method, since all of the physical processes that differentiate a DEIS spectrum from a SEIS spectrum appear as separate explicit terms in the governing equations and boundary conditions. That means we can selectively and explicitly choose to include or exclude physics in order to explore the main effects that differentiate SEIS from DEIS

***Figure 5.9***(a) shows the standard SEIS spectrum (i) for 5% SOC and the full-physics time-separated DEIS discharge spectrum (ii) for the same SOC. Between these spectra in ***Figure 5.9***(a) lie two additional partial-physics DEIS curves. The partial physics DEIS spectrum (iii) only includes terms driven by spatial variation in the solid phase surface concentration of intercalated lithium in the negative electrode, $c^s_{n,surf} = c^s_{n,surf}(x;t_b)$. All the other DEIS terms are eliminated. Because spectrum (iii) lies near SEIS curve (i), most of the variance between SEIS and DEIS under these conditions is not due to negative electrode spatial variations in intercalated lithium. The same partial-physics analysis is carried out by only considering DEIS terms driven by spatial variation in the positive electrode intercalated surface concentrations, $c^s_{p,surf} = c^s_{p,surf}(x;t_b)$. The generated spectrum labeled (iv) in ***Figure 5.9***(a) now lies near the DEIS spectrum (ii). Physics associated with positive electrode lithiation non-uniformities capture most of the variance in a DEIS discharge spectrum at low SOC.

***Figure 5.9***(b) represents the identical analysis to ***Figure 5.9***(a) but for the 0.5C charging case at 5% SOC. Again, the DEIS spectrum differs from SEIS mainly due to physics associated with solid phase surface concentration of the positive electrode, namely, most of the variance in ***Figure 5.9***(b) between spectra (i) and (ii) is captured in the partial physics spectrum (iv) not (iii).

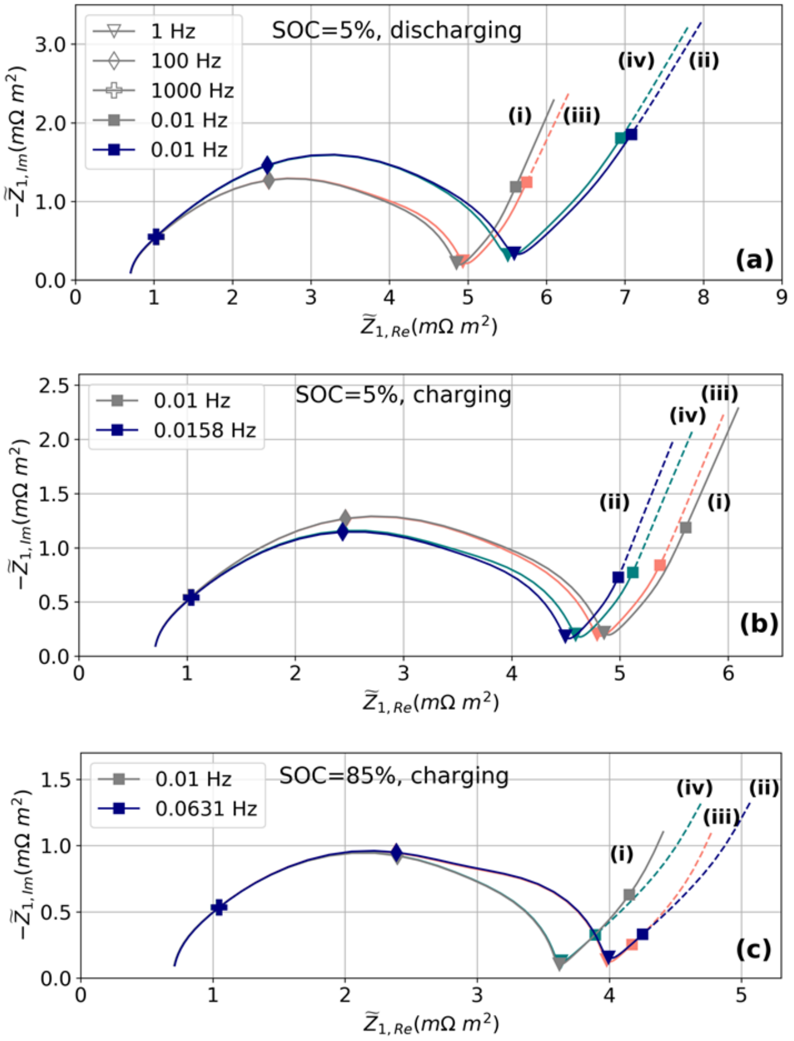

***Figure 5.9 Selectively exploring the influence of spatial variation in intercalated lithium surface concentrations on differences between SEIS (gray lines, i) and DEIS spectra (blue lines, ii) under the conditions: (a) 5% SOC during 0.5 C discharge, (b) 5% SOC during 0.5 C charge, and (c) 85% SOC during 0.5 C charge. The extra spectra (iii) and (iv) fall between the SEIS and DEIS responses because they selectively include dynamic terms solely solely associated with the negative electrode (iii) or positive electrode (iv) intercalated lithium surface concentration gradients.***

***Figure 5.9***(c) considers the driving physics at a high SOC of 85%, where we see the deviation between a charging DEIS spectrum (ii) and SEIS spectrum (i) is largely attributable to terms driven by the negative electrode intercalated surface concentration gradients instead of the positive electrode gradients seen at low SOC. Specifically, ***Figure 5.9***(c) shows that spectrum (iii) lies almost entirely on top of the full physics DEIS spectrum (ii).

The time-separated method allows one to easily attribute the dynamic deviations between SEIS and DEIS spectra to specific physical processes occurring in the cell. Interestingly, for the parameters we used here, the SEIS spectra did not strongly separate charge transfer processes on the anode and cathode by $R_{ct,i}C_{dl,i}$ time constants. Nonetheless, the deviations between DEIS and SEIS did separate by electrode, with one electrode or the other being primarily responsible for differences at each end of the charge or discharge curve (positive electrode at low SOC, negative electrode at high SOC). The selective sensitivity of DEIS to one electrode or the other at each extreme of SOC may be a useful feature of the method. For example, in fast charging, being sensitive to the negative electrode at high SOC is important for avoiding metal plating at the end of charge. Because DEIS deviations from SEIS are sensitive to the negative electrode surface lithiation at end of charge, a 1 Hz dynamic signal in a properly calibrated fast charging system might be useful as a sensitive endpoint indicator for deciding cut-off voltages using model predictive control. Likewise, having dynamic sensitivity to surface lithiation on the positive electrode with a 1 Hz modulated signal during discharge may avoid overdischarge degradation of the cobalt oxide positive electrode, though it is harder to imagine how to perform a 1 Hz modulation during discharge than it is during charging.

## 5.4 Conclusions and Future Work

We have demonstrated a computationally efficient approach to simulating the dynamic impedance of a cell using the P2D model by separating the timescale of the slow DC charge/discharge of a battery from the fast local timescale of an impedance measurement. This method allows for investigation into specific physicochemical processes that drive the difference between dynamic and stationary behavior of the battery.

Dynamic EIS can be used as a diagnostic tool and shares many similarities to a proper stationary EIS measurement, but also has information in the signal deviations from stationarity. Because it can happen while charging a battery, and is especially sensitive to negative electrode interfacial charge transfer processes as the cell approaches the end of charge, it may be valuable as a state-of-charge indicator for diagnostics and control. We believe this warrants further exploration.

General methods that we use here for time-separation is extendable to any time domain model. The method used here can easily be applied to models that contain more detailed physics to describe experimental observations more completely. For example, we can modify the diffusion modeled here to describe stage-behavior for chemistries like lithium iron phosphate[149] and graphite[150], or add physics to describe the solid-electrolyte interphase. The analysis presented in this work for comparing validity of methods, and investigating frequencies to emphasize certain physical phenomena that are particularly sensitive to dynamic processes, will also apply for more detailed models. This holds true for the time to frequency conversion approach. The underlying spectral and collocation method in x with analytical solution in r is valid for the P2D model. However, for phase change materials, if the underlying model is given by phase field models, the order of accuracy is typically limited to 1 and no significant gain can be guaranteed by the use of spectral methods. Convective problems might require grids. For challenges in simulation, please refer to our recent perspective article.[151]

Having a computationally efficient framework enables analysis into what frequencies are relevant and important to track in relation to the state and health of the battery. Compared to SEIS, where each measurement requires relaxation of the cell, DEIS can be done continuously while the battery is in operation. To keep pace with real-time experimental measurements, the time-separated approach presented in this paper can be accelerated with sophisticated algorithms, parallel and possibly cloud computing to enable real-time simulation. Additionally, experimentalists that use DEIS can use simulation results as a guide to exploring limiting phenomena that dictate the dynamic impedance response, especially for different parameters such as thicker electrodes. Combining charge/discharge voltage-time measurements with EIS and DEIS measurements may also aid in improving parameter identifiability for physics-based models.

# Chapter 6: Conclusions and Outlook

*Summary*

Modeling electroanalytical measurements of lithium sulfur and lithium-ion batteries can provide a more in-depth understanding of specific physical phenomena occurring internally and help improve both model development and cell design. In this dissertation, we discuss the challenges in developing detailed and accurate lithium sulfur continuum models. We then narrow in on using GITT and EIS models to improve the current understanding of thermodynamic and kinetic parameters in a realistic high energy density cell. We also develop a novel method to compute the DEIS for lithium-ion cells, with the ability to separate out dynamic driving forces from the overall response, a feature that standard models with standard solving methods are unable to do. We believe that a combining these physics-based models with experimental electroanalytical techniques can provide battery engineers and researchers with a more diverse range of tools for parameter identification of models and advanced battery diagnostics.

*Future work*

The lithium sulfur work here qualitatively compared simulations to experimental trends and observations from the literature and showed how the battery performance would change by modifying the parameters theoretically. Future work would include using the GITT and EIS models developed to quantitatively model engineered systems. For example, the inclusion of an additive or a different solvent can change the kinetics of polysulfide precipitation. GITT and EIS measurements can be made, and the corresponding models can be fit to the experimental data to give us information on how the rate constants have changed.

Additionally, with the development of the lithium sulfur EIS model in this work, there remains a lot of exploration in the frequency domain for proposed mechanisms and processes that are not available on the timescale of a charge/discharge. Comparing simulated EIS spectra to experimental measurements can be valuable in showing which features can and cannot be captured by the mechanisms in existing models and lead to the development of more comprehensive models. Lithium sulfur is also a very complicated system with physical processes occurring over a wide range of timescales, and hence a diagnostic tool like DEIS might be worth exploring.

Finally, as lithium-ion technology becomes more prevalent, there arises a need to control batteries better to maximize and optimize usage, and in some cases, for second use scenarios. Advanced diagnostics like DEIS can be used as a signal for model predictive control to determine cut-off voltages if we want to probe electrode sensitivity to lithium plating during charging for example. Lithium plating and other degradation phenomena can be explored by including the corresponding physical expressions into the model. Recent experimental work have been developed using DEIS to detect the onset of lithium plating,[152] and the model developed in this work can be used to understand, detect, and predict such phenomena.

# Bibliography

(1) Manthiram, A.; Fu, Y.; Su, Y.-S. Challenges and Prospects of Lithium–Sulfur Batteries. *Acc. Chem. Res.* **2013**, *46* (5), 1125–1134. https://doi.org/10.1021/ar300179v.

(2) Chung, S.-H.; Manthiram, A. Current Status and Future Prospects of Metal–Sulfur Batteries. *Advanced Materials* **2019**, *31* (27), 1901125. https://doi.org/10.1002/adma.201901125.

(3) Cleaver, T.; Kovacik, P.; Marinescu, M.; Zhang, T.; Offer, G. Perspective—Commercializing Lithium Sulfur Batteries: Are We Doing the Right Research? *J. Electrochem. Soc.* **2018**, *165* (1), A6029–A6033. https://doi.org/10.1149/2.0071801jes.

(4) Meyers, J. P.; Doyle, M.; Darling, R. M.; Newman, J. The Impedance Response of a Porous Electrode Composed of Intercalation Particles. *J. Electrochem. Soc.* **2000**, *147* (8), 2930. https://doi.org/10.1149/1.1393627.

(5) Doyle, M.; Meyers, J. P.; Newman, J. Computer Simulations of the Impedance Response of Lithium Rechargeable Batteries. *J. Electrochem. Soc.* **2000**, *147* (1), 99. https://doi.org/10.1149/1.1393162.

(6) Ramadesigan, V.; Northrop, P. W. C.; De, S.; Santhanagopalan, S.; Braatz, R. D.; Subramanian, V. R. Modeling and Simulation of Lithium-Ion Batteries from a Systems Engineering Perspective. *J. Electrochem. Soc.* **2012**, *159* (3), R31–R45. https://doi.org/10.1149/2.018203jes.

(7) Dibden, J. W.; Meddings, N.; Owen, J. R.; Garcia-Araez, N. Quantitative Galvanostatic Intermittent Titration Technique for the Analysis of a Model System with Applications in Lithium−Sulfur Batteries. *ChemElectroChem* **2018**, *5* (3), 445–454. https://doi.org/10.1002/celc.201701004.

(8) Kim, J.-J.; Kim, H. S.; Ahn, J.; Lee, K. J.; Yoo, W. C.; Sung, Y.-E. Activation of Micropore-Confined Sulfur within Hierarchical Porous Carbon for Lithium-Sulfur Batteries. *Journal of Power Sources* **2016**, *306*, 617–622. https://doi.org/10.1016/j.jpowsour.2015.12.093.

(9) Košir, U.; Kralj Cigić, I.; Markelj, J.; Drvarič Talian, S.; Dominko, R. Polysulfide Species in Various Electrolytes of Li-S Batteries – a Chromatographic Investigation. *Electrochimica Acta* **2020**, *363*, 137227. https://doi.org/10.1016/j.electacta.2020.137227.

(10) Zhao, Y.; Zhang, J.; Guo, J. Cathode–Electrolyte Interfacial Processes in Lithium‖Sulfur Batteries under Lean Electrolyte Conditions. *ACS Appl. Mater. Interfaces* **2021**, *13* (27), 31749–31755. https://doi.org/10.1021/acsami.1c08615.

(11) Busche, M. R.; Adelhelm, P.; Sommer, H.; Schneider, H.; Leitner, K.; Janek, J. Systematical Electrochemical Study on the Parasitic Shuttle-Effect in Lithium-Sulfur-Cells at Different Temperatures and Different Rates. *Journal of Power Sources* **2014**, *259*, 289–299. https://doi.org/10.1016/j.jpowsour.2014.02.075.

(12) Yu, P.; Popov, B. N.; Ritter, J. A.; White, R. E. Determination of the Lithium Ion Diffusion Coefficient in Graphite. *J. Electrochem. Soc.* **1999**, *146* (1), 8–14. https://doi.org/10.1149/1.1391556.

(13) Tröltzsch, U.; Kanoun, O.; Tränkler, H.-R. Characterizing Aging Effects of Lithium Ion Batteries by Impedance Spectroscopy. *Electrochimica Acta* **2006**, *51* (8–9), 1664–1672. https://doi.org/10.1016/j.electacta.2005.02.148.

(14) Barsoukov, E.; Kim, J. H.; Kim, J. H.; Yoon, C. O.; Lee, H. Effect of Low-Temperature Conditions on Passive Layer Growth on Li Intercalation Materials: In Situ Impedance Study. *J. Electrochem. Soc.* **1998**, *145* (8), 2711–2717. https://doi.org/10.1149/1.1838703.

(15) Huang, J.; Li, Z.; Zhang, J. Dynamic Electrochemical Impedance Spectroscopy Reconstructed from Continuous Impedance Measurement of Single Frequency during Charging/Discharging. *Journal of Power Sources* **2015**, *273*, 1098–1102. https://doi.org/10.1016/j.jpowsour.2014.07.067.

(16) Itagaki, M.; Honda, K.; Hoshi, Y.; Shitanda, I. In-Situ EIS to Determine Impedance Spectra of Lithium-Ion Rechargeable Batteries during Charge and Discharge Cycle. *Journal of Electroanalytical Chemistry* **2015**, *737*, 78–84. https://doi.org/10.1016/j.jelechem.2014.06.004.

(17) Itagaki, M.; Kobari, N.; Yotsuda, S.; Watanabe, K.; Kinoshita, S.; Ue, M. In Situ Electrochemical Impedance Spectroscopy to Investigate Negative Electrode of Lithium-Ion Rechargeable Batteries. *Journal of Power Sources* **2004**, *135* (1–2), 255–261. https://doi.org/10.1016/j.jpowsour.2004.04.004.

(18) Itagaki, M.; Kobari, N.; Yotsuda, S.; Watanabe, K.; Kinoshita, S.; Ue, M. LiCoO2 Electrode/Electrolyte Interface of Li-Ion Rechargeable Batteries Investigated by in Situ Electrochemical Impedance Spectroscopy. *Journal of Power Sources* **2005**, *148*, 78–84. https://doi.org/10.1016/j.jpowsour.2005.02.007.

(19) Northrop, P. W. C.; Ramadesigan, V.; De, S.; Subramanian, V. R. Coordinate Transformation, Orthogonal Collocation, Model Reformulation and Simulation of Electrochemical-Thermal Behavior of Lithium-Ion Battery Stacks. *J. Electrochem. Soc.* **2011**, *158* (12), A1461. https://doi.org/10.1149/2.058112jes.

(20) Lawder, M. T. Extending Explicit and Linearly Implicit ODE Solvers for Index-1 DAEs. *Computers and Chemical Engineering* **2015**, 10.

(21) Risse, S.; Cañas, N. A.; Wagner, N.; Härk, E.; Ballauff, M.; Friedrich, K. A. Correlation of Capacity Fading Processes and Electrochemical Impedance Spectra in Lithium/Sulfur Cells. *Journal of Power Sources* **2016**, *323*, 107–114. https://doi.org/10.1016/j.jpowsour.2016.05.032.

(22) Parke, C. D.; Teo, L.; Schwartz, D. T.; Subramanian, V. R. Progress on Continuum Modeling of Lithium–Sulfur Batteries. *Sustainable Energy Fuels* **2021**, *5*, 5946–5966. https://doi.org/10.1039/D1SE01090E.

(23) Liu, Z.; Mistry, A.; Mukherjee, P. P. Mesoscale Physicochemical Interactions in Lithium–Sulfur Batteries: Progress and Perspective. *Journal of Electrochemical Energy Conversion and Storage* **2018**, *15* (1), 010802. https://doi.org/10.1115/1.4037785.

(24) Diao, Y.; Xie, K.; Xiong, S.; Hong, X. Shuttle Phenomenon – The Irreversible Oxidation Mechanism of Sulfur Active Material in Li–S Battery. *Journal of Power Sources* **2013**, *235*, 181–186. https://doi.org/10.1016/j.jpowsour.2013.01.132.

(25) Li, S.; Jiang, M.; Xie, Y.; Xu, H.; Jia, J.; Li, J. Developing High-Performance Lithium Metal Anode in Liquid Electrolytes: Challenges and Progress. *Advanced Materials* **2018**, *30* (17), 1706375. https://doi.org/10.1002/adma.201706375.

(26) Bhargav, A.; He, J.; Gupta, A.; Manthiram, A. Lithium-Sulfur Batteries: Attaining the Critical Metrics. *Joule* **2020**, *4* (2), 285–291. https://doi.org/10.1016/j.joule.2020.01.001.

(27) Fang, R.; Zhao, S.; Sun, Z.; Wang, D.-W.; Cheng, H.-M.; Li, F. More Reliable Lithium-Sulfur Batteries: Status, Solutions and Prospects. *Advanced Materials* **2017**, *29* (48), 1606823. https://doi.org/10.1002/adma.201606823.

(28) Brückner, J.; Thieme, S.; Grossmann, H. T.; Dörfler, S.; Althues, H.; Kaskel, S. Lithium–Sulfur Batteries: Influence of C-Rate, Amount of Electrolyte and Sulfur Loading on Cycle

Performance. *Journal of Power Sources* **2014**, *268*, 82–87. https://doi.org/10.1016/j.jpowsour.2014.05.143.

(29) Kumaresan, K.; Mikhaylik, Y.; White, R. E. A Mathematical Model for a Lithium–Sulfur Cell. *J. Electrochem. Soc.* **2008**, *155* (8), A576–A582. https://doi.org/10.1149/1.2937304.

(30) Mistry, A. N.; Mukherjee, P. P. "Shuttle" in Polysulfide Shuttle: Friend or Foe? *J. Phys. Chem. C* **2018**, *122* (42), 23845–23851. https://doi.org/10.1021/acs.jpcc.8b06077.

(31) Mikhaylik, Y. V.; Akridge, J. R. Polysulfide Shuttle Study in the Li/S Battery System. *J. Electrochem. Soc.* **2004**, *151* (11), A1969–A1976. https://doi.org/10.1149/1.1806394.

(32) Danner, T.; Zhu, G.; Hofmann, A. F.; Latz, A. Modeling of Nano-Structured Cathodes for Improved Lithium-Sulfur Batteries. *Electrochimica Acta* **2015**, *184*, 124–133. https://doi.org/10.1016/j.electacta.2015.09.143.

(33) Marinescu, M.; Zhang, T.; Offer, G. J. A Zero Dimensional Model of Lithium–Sulfur Batteries during Charge and Discharge. *Phys. Chem. Chem. Phys.* **2016**, *18* (1), 584–593. https://doi.org/10.1039/C5CP05755H.

(34) Erisen, N.; Eroglu, D. Modeling the Discharge Behavior of a Lithium-sulfur Battery. *Int J Energy Res* **2020**, *44* (13), 10599–10611. https://doi.org/10.1002/er.5701.

(35) Zhang, T.; Marinescu, M.; Walus, S.; Offer, G. J. Modelling Transport-Limited Discharge Capacity of Lithium-Sulfur Cells. *Electrochimica Acta* **2016**, *219*, 502–508. https://doi.org/10.1016/j.electacta.2016.10.032.

(36) Waluś, S.; Barchasz, C.; Bouchet, R.; Leprêtre, J.-C.; Colin, J.-F.; Martin, J.-F.; Elkaïm, E.; Baehtz, C.; Alloin, F. Lithium/Sulfur Batteries Upon Cycling: Structural Modifications and Species Quantification by In Situ and Operando X-Ray Diffraction Spectroscopy. *Adv. Energy Mater.* **2015**, *5* (16), 1500165. https://doi.org/10.1002/aenm.201500165.

(37) Gorlin, Y.; Patel, M. U. M.; Freiberg, A.; He, Q.; Piana, M.; Tromp, M.; Gasteiger, H. A. Understanding the Charging Mechanism of Lithium-Sulfur Batteries Using Spatially Resolved Operando X-Ray Absorption Spectroscopy. *Journal of The Electrochemical Society* **2016**, *163* (6), A930–A939.

(38) Drvarič Talian, S.; Moškon, J.; Dominko, R.; Gaberšček, M. Reactivity and Diffusivity of Li Polysulfides: A Fundamental Study Using Impedance Spectroscopy. *ACS Appl. Mater. Interfaces* **2017**, *9* (35), 29760–29770. https://doi.org/10.1021/acsami.7b08317.

(39) Barchasz, C.; Molton, F.; Duboc, C.; Leprêtre, J.-C.; Patoux, S.; Alloin, F. Lithium/Sulfur Cell Discharge Mechanism: An Original Approach for Intermediate Species Identification. *Anal. Chem.* **2012**, *84* (9), 3973–3980. https://doi.org/10.1021/ac2032244.

(40) Schön, P.; Hintz, F.; Krewer, U. Electrochemical Analysis of the Reaction Mechanism of Sulfur Reduction as a Function of State of Charge. *Electrochimica Acta* **2019**, *295*, 926–933. https://doi.org/10.1016/j.electacta.2018.08.153.

(41) Schön, P.; Krewer, U. Revealing the Complex Sulfur Reduction Mechanism Using Cyclic Voltammetry Simulation. *Electrochimica Acta* **2021**, *373*, 137523. https://doi.org/10.1016/j.electacta.2020.137523.

(42) Lu, Y.-C.; He, Q.; Gasteiger, H. A. Probing the Lithium–Sulfur Redox Reactions: A Rotating-Ring Disk Electrode Study. *J. Phys. Chem. C* **2014**, *118* (11), 5733–5741. https://doi.org/10.1021/jp500382s.

(43) Thangavel, V.; Mastouri, A.; Guéry, C.; Morcrette, M.; Franco, A. A. Understanding the Reaction Steps Involving Polysulfides in 1 M LiTFSI in TEGDME : DOL Using Cyclic Voltammetry Experiments and Modelling. *Batteries & Supercaps* **2021**, *4*, 152–162. https://doi.org/10.1002/batt.202000175.

(44) Safari, M.; Kwok, C. Y.; Nazar, L. F. Transport Properties of Polysulfide Species in Lithium–Sulfur Battery Electrolytes: Coupling of Experiment and Theory. *ACS Cent. Sci.* **2016**, *2* (8), 560–568. https://doi.org/10.1021/acscentsci.6b00169.
(45) Shim, J.; Ko, T. J.; Yoo, K. Study for an Effect of LiNO3 on Polysulfide Multistep Reaction in Li/S Battery. *Journal of Industrial and Engineering Chemistry* **2019**, *80*, 283–291. https://doi.org/10.1016/j.jiec.2019.08.006.
(46) Gupta, A.; Bhargav, A.; Manthiram, A. Highly Solvating Electrolytes for Lithium–Sulfur Batteries. *Adv. Energy Mater.* **2019**, *9* (6), 1803096. https://doi.org/10.1002/aenm.201803096.
(47) Parke, C. D.; Subramaniam, A.; Subramanian, V. R.; Schwartz, D. T. Realigning the Chemistry and Parameterization of Lithium-Sulfur Battery Models to Accommodate Emerging Experimental Evidence and Cell Configurations. *ChemElectroChem* **2021**, *8* (6), 1098–1106. https://doi.org/10.1002/celc.202001575.
(48) Pascal, T. A.; Wujcik, K. H.; Wang, D. R.; Balsara, N. P.; Prendergast, D. Thermodynamic Origins of the Solvent-Dependent Stability of Lithium Polysulfides from First Principles. *Phys. Chem. Chem. Phys.* **2017**, *19* (2), 1441–1448. https://doi.org/10.1039/C6CP06889H.
(49) Kamphaus, E. P.; Balbuena, P. B. First-Principles Investigation of Lithium Polysulfide Structure and Behavior in Solution. *J. Phys. Chem. C* **2017**, *121* (39), 21105–21117. https://doi.org/10.1021/acs.jpcc.7b04822.
(50) Ghaznavi, M.; Chen, P. Sensitivity Analysis of a Mathematical Model of Lithium–Sulfur Cells: Part II: Precipitation Reaction Kinetics and Sulfur Content. *Journal of Power Sources* **2014**, *257*, 402–411. https://doi.org/10.1016/j.jpowsour.2013.12.145.
(51) Ghaznavi, M.; Chen, P. Analysis of a Mathematical Model of Lithium-Sulfur Cells Part III: Electrochemical Reaction Kinetics, Transport Properties and Charging. *Electrochimica Acta* **2014**, *137*, 575–585. https://doi.org/10.1016/j.electacta.2014.06.033.
(52) Danner, T.; Latz, A. On the Influence of Nucleation and Growth of S8 and Li2S in Lithium-Sulfur Batteries. *Electrochimica Acta* **2019**, *322*, 134719. https://doi.org/10.1016/j.electacta.2019.134719.
(53) Park, C.; Ronneburg, A.; Risse, S.; Ballauff, M.; Kanduč, M.; Dzubiella, J. Structural and Transport Properties of Li/S Battery Electrolytes: Role of the Polysulfide Species. *J. Phys. Chem. C* **2019**, *123* (16), 10167–10177. https://doi.org/10.1021/acs.jpcc.8b10175.
(54) Zhang, T.; Marinescu, M.; O'Neill, L.; Wild, M.; Offer, G. Modeling the Voltage Loss Mechanisms in Lithium–Sulfur Cells: The Importance of Electrolyte Resistance and Precipitation Kinetics. *Phys. Chem. Chem. Phys.* **2015**, *17* (35), 22581–22586. https://doi.org/10.1039/C5CP03566J.
(55) Yoo, K.; Song, M.-K.; Cairns, E. J.; Dutta, P. Numerical and Experimental Investigation of Performance Characteristics of Lithium/Sulfur Cells. *Electrochimica Acta* **2016**, *213*, 174–185. https://doi.org/10.1016/j.electacta.2016.07.110.
(56) Zhang, T.; Marinescu, M.; Walus, S.; Kovacik, P.; Offer, G. J. What Limits the Rate Capability of Li-S Batteries during Discharge: Charge Transfer or Mass Transfer? *J. Electrochem. Soc.* **2018**, *165* (1), A6001–A6004. https://doi.org/10.1149/2.0011801jes.
(57) Xiong, C.; Zhao, T. S.; Ren, Y. X.; Jiang, H. R.; Zhou, X. L. Mathematical Modeling of the Charging Process of Li-S Batteries by Incorporating the Size-Dependent Li2S Dissolution. *Electrochimica Acta* **2019**, *296*, 954–963. https://doi.org/10.1016/j.electacta.2018.11.159.

(58) Ren, Y. X.; Zhao, T. S.; Liu, M.; Tan, P.; Zeng, Y. K. Modeling of Lithium-Sulfur Batteries Incorporating the Effect of Li2S Precipitation. *Journal of Power Sources* **2016**, *336*, 115–125. https://doi.org/10.1016/j.jpowsour.2016.10.063.

(59) Andrei, P.; Shen, C.; Zheng, J. P. Theoretical and Experimental Analysis of Precipitation and Solubility Effects in Lithium-Sulfur Batteries. *Electrochimica Acta* **2018**, *284*, 469–484. https://doi.org/10.1016/j.electacta.2018.07.045.

(60) Peng, H.-J.; Huang, J.-Q.; Liu, X.-Y.; Cheng, X.-B.; Xu, W.-T.; Zhao, C.-Z.; Wei, F.; Zhang, Q. Healing High-Loading Sulfur Electrodes with Unprecedented Long Cycling Life: Spatial Heterogeneity Control. *J. Am. Chem. Soc.* **2017**, *139*, 8458–8466.

(61) Yu, S.-H.; Huang, X.; Schwarz, K.; Huang, R.; Arias, T. A.; Brock, J. D.; Abruña, H. D. Direct Visualization of Sulfur Cathodes: New Insights into Li–S Batteries *via Operando* X-Ray Based Methods. *Energy Environ. Sci.* **2018**, *11* (1), 202–210. https://doi.org/10.1039/C7EE02874A.

(62) Fan, F. Y.; Chiang, Y.-M. Electrodeposition Kinetics in Li-S Batteries: Effects of Low Electrolyte/Sulfur Ratios and Deposition Surface Composition. *J. Electrochem. Soc.* **2017**, *164* (4), A917–A922. https://doi.org/10.1149/2.0051706jes.

(63) Mistry, A.; Mukherjee, P. P. Precipitation–Microstructure Interactions in the Li-Sulfur Battery Electrode. *J. Phys. Chem. C* **2017**, *121* (47), 26256–26264. https://doi.org/10.1021/acs.jpcc.7b09997.

(64) Shah, K.; Subramaniam, A.; Mishra, L.; Jang, T.; Bazant, M. Z.; Braatz, R. D.; Subramanian, V. R. Editors' Choice—Perspective—Challenges in Moving to Multiscale Battery Models: Where Electrochemistry Meets and Demands More from Math. *J. Electrochem. Soc.* **2020**, *167* (13), 133501. https://doi.org/10.1149/1945-7111/abb37b.

(65) Liu, Z.; Hubble, D.; Balbuena, P. B.; Mukherjee, P. P. Adsorption of Insoluble Polysulfides $Li_2S_x$ (x = 1, 2) on $Li_2S$ Surfaces. *Phys. Chem. Chem. Phys.* **2015**, *17* (14), 9032–9039. https://doi.org/10.1039/C4CP06118G.

(66) Seh, Z. W.; Li, W.; Cha, J. J.; Zheng, G.; Yang, Y.; McDowell, M. T.; Hsu, P.-C.; Cui, Y. Sulphur–TiO2 Yolk–Shell Nanoarchitecture with Internal Void Space for Long-Cycle Lithium–Sulphur Batteries. *Nat Commun* **2013**, *4* (1), 1331. https://doi.org/10.1038/ncomms2327.

(67) Ji, X.; Evers, S.; Black, R.; Nazar, L. F. Stabilizing Lithium–Sulphur Cathodes Using Polysulphide Reservoirs. *Nat Commun* **2011**, *2* (1), 325. https://doi.org/10.1038/ncomms1293.

(68) Thangavel, V.; Xue, K.-H.; Mammeri, Y.; Quiroga, M.; Mastouri, A.; Guéry, C.; Johansson, P.; Morcrette, M.; Franco, A. A. A Microstructurally Resolved Model for Li-S Batteries Assessing the Impact of the Cathode Design on the Discharge Performance. *J. Electrochem. Soc.* **2016**, *163* (13), A2817–A2829. https://doi.org/10.1149/2.0051614jes.

(69) Jayaprakash, N.; Shen, J.; Moganty, S. S.; Corona, A.; Archer, L. A. Porous Hollow Carbon@Sulfur Composites for High-Power Lithium–Sulfur Batteries. *Angewandte Chemie International Edition* **2011**, *50* (26), 5904–5908. https://doi.org/10.1002/anie.201100637.

(70) Shim, J.; Striebel, K. A.; Cairns, E. J. The Lithium/Sulfur Rechargeable Cell. *Journal of The Electrochemical Society* **2002**, *149* (10), A1321–A1325.

(71) Cheon, S.-E.; Ko, K.-S.; Cho, J.-H.; Kim, S.-W.; Chin, E.-Y.; Kim, H.-T. Rechargeable Lithium Sulfur Battery. *Journal of The Electrochemical Society* **2003**, *150* (6), A796–A799.

(72) Zhao, J.; Yang, Y.; Katiyar, R. S.; Chen, Z. Phosphorene as a Promising Anchoring Material for Lithium–Sulfur Batteries: A Computational Study. *J. Mater. Chem. A* **2016**, *4* (16), 6124–6130. https://doi.org/10.1039/C6TA00871B.

(73) Monroe, C.; Newman, J. The Impact of Elastic Deformation on Deposition Kinetics at LithiumÕPolymer Interfaces. *Journal of The Electrochemical Society* **2005**, *152* (2), A396–A404.

(74) Barai, P.; Higa, K.; Srinivasan, V. Impact of External Pressure and Electrolyte Transport Properties on Lithium Dendrite Growth. *J. Electrochem. Soc.* **2018**, *165* (11), A2654–A2666. https://doi.org/10.1149/2.0651811jes.

(75) Bai, P.; Guo, J.; Wang, M.; Kushima, A.; Su, L.; Li, J.; Brushett, F. R.; Bazant, M. Z. Interactions between Lithium Growths and Nanoporous Ceramic Separators. *Joule* **2018**, *2* (11), 2434–2449. https://doi.org/10.1016/j.joule.2018.08.018.

(76) Wood, K. N.; Kazyak, E.; Chadwick, A. F.; Chen, K.-H.; Zhang, J.-G.; Thornton, K.; Dasgupta, N. P. Dendrites and Pits: Untangling the Complex Behavior of Lithium Metal Anodes through Operando Video Microscopy. *ACS Cent. Sci.* **2016**, *2* (11), 790–801. https://doi.org/10.1021/acscentsci.6b00260.

(77) Subramaniam, A.; Chen, J.; Jang, T.; Geise, N. R.; Kasse, R. M.; Toney, M. F.; Subramanian, V. R. Analysis and Simulation of One-Dimensional Transport Models for Lithium Symmetric Cells. *J. Electrochem. Soc.* **2019**, *166* (15), A3806–A3819. https://doi.org/10.1149/2.0261915jes.

(78) Chen, X.; Hou, T.-Z.; Li, B.; Yan, C.; Zhu, L.; Guan, C.; Cheng, X.-B.; Peng, H.-J.; Huang, J.-Q.; Zhang, Q. Towards Stable Lithium-Sulfur Batteries: Mechanistic Insights into Electrolyte Decomposition on Lithium Metal Anode. *Energy Storage Materials* **2017**, *8*, 194–201. https://doi.org/10.1016/j.ensm.2017.01.003.

(79) Liu, Z.; Bertolini, S.; Balbuena, P. B.; Mukherjee, P. P. Li $_2$ S Film Formation on Lithium Anode Surface of Li–S Batteries. *ACS Appl. Mater. Interfaces* **2016**, *8* (7), 4700–4708. https://doi.org/10.1021/acsami.5b11803.

(80) Marinescu, M.; O'Neill, L.; Zhang, T.; Walus, S.; Wilson, T. E.; Offer, G. J. Irreversible vs Reversible Capacity Fade of Lithium-Sulfur Batteries during Cycling: The Effects of Precipitation and Shuttle. *J. Electrochem. Soc.* **2018**, *165* (1), A6107–A6118. https://doi.org/10.1149/2.0171801jes.

(81) Hofmann, A. F.; Fronczek, D. N.; Bessler, W. G. Mechanistic Modeling of Polysulfide Shuttle and Capacity Loss in Lithium–Sulfur Batteries. *Journal of Power Sources* **2014**, *259*, 300–310. https://doi.org/10.1016/j.jpowsour.2014.02.082.

(82) Choi, J.-W.; Kim, J.-K.; Cheruvally, G.; Ahn, J.-H.; Ahn, H.-J.; Kim, K.-W. Rechargeable Lithium/Sulfur Battery with Suitable Mixed Liquid Electrolytes. *Electrochimica Acta* **2007**, *52* (5), 2075–2082. https://doi.org/10.1016/j.electacta.2006.08.016.

(83) Kamyab, N.; Coman, P. T.; Madi Reddy, S. K.; Santhanagopalan, S.; White, R. E. Mathematical Model for Li-S Cell with Shuttling-Induced Capacity Loss Approximation. *J. Electrochem. Soc.* **2020**, *167* (13), 130532. https://doi.org/10.1149/1945-7111/abbbbf.

(84) Al-Mahmoud, S. M.; Dibden, J. W.; Owen, J. R.; Denuault, G.; Garcia-Araez, N. A Simple, Experiment-Based Model of the Initial Self-Discharge of Lithium-Sulphur Batteries. *Journal of Power Sources* **2016**, *306*, 323–328. https://doi.org/10.1016/j.jpowsour.2015.12.031.

(85) Moy, D.; Manivannan, A.; Narayanan, S. R. Direct Measurement of Polysulfide Shuttle Current: A Window into Understanding the Performance of Lithium-Sulfur Cells. *J. Electrochem. Soc.* **2015**, *162* (1), A1–A7. https://doi.org/10.1149/2.0181501jes.

(86) Wen, G.; Rehman, S.; Tranter, T. G.; Ghosh, D.; Chen, Z.; Gostick, J. T.; Pope, M. A. Insights into Multiphase Reactions during Self-Discharge of Li-S Batteries. *Chem. Mater.* **2020**, *32* (11), 4518–4526. https://doi.org/10.1021/acs.chemmater.0c00235.

(87) Mistry, A. N.; Mukherjee, P. P. Electrolyte Transport Evolution Dynamics in Lithium–Sulfur Batteries. *J. Phys. Chem. C* **2018**, *122* (32), 18329–18335. https://doi.org/10.1021/acs.jpcc.8b05442.

(88) Shebert, G. L.; Zamani, S.; Yi, C.; Joo, Y. L. Polysulfide Entrapment and Retardation in Gel Electrolyte Li–S Batteries: Experiments and Modeling. *J. Mater. Chem. A* **2020**, *8* (8), 4341–4353. https://doi.org/10.1039/C9TA14234G.

(89) Zhu, K.; Wang, C.; Chi, Z.; Ke, F.; Yang, Y.; Wang, A.; Wang, W.; Miao, L. How Far Away Are Lithium-Sulfur Batteries From Commercialization? *Front. Energy Res.* **2019**, *7*, 123. https://doi.org/10.3389/fenrg.2019.00123.

(90) Liu, J.; Bao, Z.; Cui, Y.; Dufek, E. J.; Goodenough, J. B.; Khalifah, P.; Li, Q.; Liaw, B. Y.; Liu, P.; Manthiram, A.; Meng, Y. S.; Subramanian, V. R.; Toney, M. F.; Viswanathan, V. V.; Whittingham, M. S.; Xiao, J.; Xu, W.; Yang, J.; Yang, X.-Q.; Zhang, J.-G. Pathways for Practical High-Energy Long-Cycling Lithium Metal Batteries. *Nat Energy* **2019**, *4* (3), 180–186. https://doi.org/10.1038/s41560-019-0338-x.

(91) Erisen, N.; Emerce, N. B.; Erensoy, S. C.; Eroglu, D. Modeling the Effect of Key Cathode Design Parameters on the Electrochemical Performance of a Lithium-Sulfur Battery. *Int J Energy Res* **2018**, *42* (8), 2631–2642. https://doi.org/10.1002/er.4045.

(92) Michaelis, C.; Erisen, N.; Eroglu, D.; Koenig, G. M. Electrochemical Performance and Modeling of Lithium-Sulfur Batteries with Varying Carbon to Sulfur Ratios. *Int J Energy Res* **2019**, *43* (2), 874–883. https://doi.org/10.1002/er.4318.

(93) Emerce, N. B.; Eroglu, D. Effect of Electrolyte-to-Sulfur Ratio in the Cell on the Li-S Battery Performance. *J. Electrochem. Soc.* **2019**, *166* (8), A1490–A1500. https://doi.org/10.1149/2.0621908jes.

(94) Bilal, H. M.; Eroglu, D. Assessment of Li-S Battery Performance as a Function of Electrolyte-to-Sulfur Ratio. *J. Electrochem. Soc.* **2021**, *168* (3), 030502. https://doi.org/10.1149/1945-7111/abe7a2.

(95) McCloskey, B. D. Attainable Gravimetric and Volumetric Energy Density of Li–S and Li Ion Battery Cells with Solid Separator-Protected Li Metal Anodes. *J. Phys. Chem. Lett.* **2015**, *6* (22), 4581–4588. https://doi.org/10.1021/acs.jpclett.5b01814.

(96) Lee, J. H.; Kang, J.; Kim, S.-W.; Halim, W.; Frey, M. W.; Joo, Y. L. Effective Suppression of the Polysulfide Shuttle Effect in Lithium–Sulfur Batteries by Implementing RGO–PEDOT:PSS-Coated Separators via Air-Controlled Electrospray. *ACS Omega* **2018**, *3* (12), 16465–16471. https://doi.org/10.1021/acsomega.8b02551.

(97) Deng, Z.; Zhang, Z.; Lai, Y.; Liu, J.; Li, J.; Liu, Y. Electrochemical Impedance Spectroscopy Study of a Lithium/Sulfur Battery: Modeling and Analysis of Capacity Fading. *J. Electrochem. Soc.* **2013**, *160* (4), A553–A558. https://doi.org/10.1149/2.026304jes.

(98) Qiu, X.; Hua, Q.; Zheng, L.; Dai, Z. Study of the Discharge/Charge Process of Lithium–Sulfur Batteries by Electrochemical Impedance Spectroscopy. *RSC Adv.* **2020**, *10* (9), 5283–5293. https://doi.org/10.1039/C9RA10527A.

(99) Waluś, S.; Barchasz, C.; Bouchet, R.; Alloin, F. Electrochemical Impedance Spectroscopy Study of Lithium–Sulfur Batteries: Useful Technique to Reveal the Li/S Electrochemical Mechanism. *Electrochimica Acta* **2020**, *359*, 136944. https://doi.org/10.1016/j.electacta.2020.136944.

(100) Fronczek, D. N.; Bessler, W. G. Insight into Lithium–Sulfur Batteries: Elementary Kinetic Modeling and Impedance Simulation. *Journal of Power Sources* **2013**, *244*, 183–188. https://doi.org/10.1016/j.jpowsour.2013.02.018.

(101) Ghaznavi, M.; Chen, P. Sensitivity Analysis of a Mathematical Model of Lithium–Sulfur Cells Part I: Applied Discharge Current and Cathode Conductivity. *Journal of Power Sources* **2014**, *257*, 394–401. https://doi.org/10.1016/j.jpowsour.2013.10.135.

(102) Parke, C. D.; Subramaniam, A.; Kolluri, S.; Schwartz, D. T.; Subramanian, V. R. An Efficient Electrochemical Tanks-in-Series Model for Lithium Sulfur Batteries. *J. Electrochem. Soc.* **2020**, *167* (16), 163503. https://doi.org/10.1149/1945-7111/abcc30.

(103) Xu, C.; Cleary, T.; Li, G.; Wang, D.; Fathy, H. Parameter Identification and Sensitivity Analysis for Zero-Dimensional Physics-Based Lithium-Sulfur Battery Models. *ASME Letters in Dynamic Systems and Control* **2021**, *1* (4), 041001. https://doi.org/10.1115/1.4050125.

(104) Ramadesigan, V.; Chen, K.; Burns, N. A.; Boovaragavan, V.; Braatz, R. D.; Subramanian, V. R. Parameter Estimation and Capacity Fade Analysis of Lithium-Ion Batteries Using Reformulated Models. *J. Electrochem. Soc.* **2011**, *158* (9), A1048–A1054. https://doi.org/10.1149/1.3609926.

(105) Xu, C.; Cleary, T.; Wang, D.; Li, G.; Rahn, C.; Wang, D.; Rajamani, R.; Fathy, H. K. Online State Estimation for a Physics-Based Lithium-Sulfur Battery Model. *Journal of Power Sources* **2021**, *489*, 229495. https://doi.org/10.1016/j.jpowsour.2021.229495.

(106) Mishra, L.; Subramaniam, A.; Jang, T.; Shah, K.; Uppaluri, M.; Roberts, S. A.; Subramanian, V. R. Perspective—Mass Conservation in Models for Electrodeposition/Stripping in Lithium Metal Batteries. *J. Electrochem. Soc.* **2021**, *168* (9), 092502. https://doi.org/10.1149/1945-7111/ac2091.

(107) Son, Y.; Lee, J.-S.; Son, Y.; Jang, J.-H.; Cho, J. Recent Advances in Lithium Sulfide Cathode Materials and Their Use in Lithium Sulfur Batteries. *Adv. Energy Mater.* **2015**, *5* (16), 1500110. https://doi.org/10.1002/aenm.201500110.

(108) Steudel, R.; Chivers, T. The Role of Polysulfide Dianions and Radical Anions in the Chemical, Physical and Biological Sciences, Including Sulfur-Based Batteries. *Chem. Soc. Rev.* **2019**, *48* (12), 3279–3319. https://doi.org/10.1039/C8CS00826D.

(109) Newman, J.; Thomas-Alyea, K. *Electrochemical Systems*, 3rd ed.; John Wiley & Sons, Inc.: Hoboken, New Jersey, 2004.

(110) Delasalle, J. Claire Parfitt (Warwick) Thesis - Characterization, Modelling, Management LiS for Spacecraft Applications. 339.

(111) Xu, G.; Yan, Q.; Wang, S.; Kushima, A.; Bai, P.; Liu, K.; Zhang, X.; Tang, Z.; Li, J. A Thin Multifunctional Coating on a Separator Improves the Cyclability and Safety of Lithium Sulfur Batteries. *Chem. Sci.* **2017**, *8* (9), 6619–6625. https://doi.org/10.1039/C7SC01961K.

(112) Cuisinier, M.; Hart, C.; Balasubramanian, M.; Garsuch, A.; Nazar, L. F. Radical or Not Radical: Revisiting Lithium–Sulfur Electrochemistry in Nonaqueous Electrolytes. *Advanced Energy Materials* **2015**, *5* (16), 1401801. https://doi.org/10.1002/aenm.201401801.

(113) Wild, M.; O'Neill, L.; Zhang, T.; Purkayastha, R.; Minton, G.; Marinescu, M.; Offer, G. J. Lithium Sulfur Batteries, a Mechanistic Review. *Energy Environ. Sci.* **2015**, *8* (12), 3477–3494. https://doi.org/10.1039/C5EE01388G.

(114) Satopaa, V.; Albrecht, J.; Irwin, D.; Raghavan, B. Finding a "Kneedle" in a Haystack: Detecting Knee Points in System Behavior. In *2011 31st International Conference on*

*Distributed Computing Systems Workshops*; IEEE: Minneapolis, MN, USA, 2011; pp 166–171. https://doi.org/10.1109/ICDCSW.2011.20.

(115) Assary, R. S.; Curtiss, L. A.; Moore, J. S. Toward a Molecular Understanding of Energetics in Li–S Batteries Using Nonaqueous Electrolytes: A High-Level Quantum Chemical Study. *J. Phys. Chem. C* **2014**, *118* (22), 11545–11558. https://doi.org/10.1021/jp5015466.

(116) Sun, M.; Wang, X.; Wang, J.; Yang, H.; Wang, L.; Liu, T. Assessment on the Self-Discharge Behavior of Lithium–Sulfur Batteries with $LiNO_3$ -Possessing Electrolytes. *ACS Appl. Mater. Interfaces* **2018**, *10* (41), 35175–35183. https://doi.org/10.1021/acsami.8b11890.

(117) Pathak, M.; Murbach, M. D.; Pathak, C.; Jang, T.-J.; Qi, Y.; Schwartz, D. T.; Subramanian, V. R. Fast Impedance Simulation of Lithium-Ion Batteries with Pseudo-Two Dimensional Electrochemical Models. *J. Electrochem. Soc.* **2018**, *165* (7), A1324–A1337. https://doi.org/10.1149/2.0831805jes.

(118) Teo, L.; Subramanian, V. R.; Schwartz, D. T. Dynamic Electrochemical Impedance Spectroscopy of Lithium-Ion Batteries: Revealing Underlying Physics through Efficient Joint Time-Frequency Modeling. *J. Electrochem. Soc.* **2021**, *168* (1), 010526. https://doi.org/10.1149/1945-7111/abda04.

(119) Macdonald, D. D. Why Electrochemical Impedance Spectroscopy Is the Ultimate Tool in Mechanistic Analysis. *ECS Transactions* **2009**, *19* (20), 55–79.

(120) Urquidi-Macdonald, M.; Real, S.; Macdonald, D. D. Applications of Kramers-Kronig Transforms in the Analysis of Electrochemical Impedance Data-III. Stability and Linearity. *Electrochimica Acta* **1990**, *35* (10), 1559–1566. https://doi.org/10.1016/0013-4686(90)80010-L.

(121) Bandarenka, A. S. Exploring the Interfaces between Metal Electrodes and Aqueous Electrolytes with Electrochemical Impedance Spectroscopy. *Analyst* **2013**, *138* (19), 5540–5554. https://doi.org/10.1039/c3an00791j.

(122) Gavaghan, D. J.; Bond, A. M. Complete Numerical Simulation of the Techniques of Alternating Current Linear Sweep and Cyclic Voltammetry: Analysis of a Reversible Process by Conventional and Fast Fourier Transform Methods. *Journal of Electroanalytical Chemistry* **2000**, *480* (1–2), 133–149. https://doi.org/10.1016/S0022-0728(99)00476-3.

(123) Sacci, R.L., Harrington, D. A. Dynamic Electrochemical Impedance Spectroscopy. *ECS Transactions* **2009**, *19* (20), 31–42.

(124) Sacci, R. L.; Seland, F.; Harrington, D. A. Dynamic Electrochemical Impedance Spectroscopy, for Electrocatalytic Reactions. *Electrochimica Acta* **2014**, *131*, 13–19. https://doi.org/10.1016/j.electacta.2014.02.120.

(125) Ragoisha, G. A.; Bondarenko, A. S. Potentiodynamic Electrochemical Impedance Spectroscopy. *Electrochimica Acta* **2005**, *50* (7–8), 1553–1563. https://doi.org/10.1016/j.electacta.2004.10.055.

(126) Stoynov, Z. B.; Savova-Stoynov, B. Impedance Study of Non-Stationary Systems: Four-Dimensional Analysis. *Journal of Electroanalytical Chemistry* **1985**, *183*, 133–144.

(127) Dong, T. K.; Kirchev, A.; Mattera, F.; Kowal, J.; Bultel, Y. Dynamic Modeling of Li-Ion Batteries Using an Equivalent Electrical Circuit. *Journal of The Electrochemical Society* **2011**, *158* (3), A326–A336. https://doi.org/10.1149/1.3543710.

(128) Karden, E.; Buller, S.; De Doncker, R. W. A Method for Measurement and Interpretation of Impedance Spectra for Industrial Batteries. *Journal of Power Sources* **2000**, *85* (1), 72–78. https://doi.org/10.1016/S0378-7753(99)00385-7.

(129) Juang, L. W.; Kollmeyer, P. J.; Zhao, R.; Jahns, T. M.; Lorenz, R. D. The Impact of DC Bias Current on the Modeling of Lithium Iron Phosphate and Lead-Acid Batteries Observed Using Electrochemical Impedance Spectroscopy. *2014 IEEE Energy Conversion Congress and Exposition, ECCE 2014* **2014**, 2575–2581. https://doi.org/10.1109/ECCE.2014.6953745.

(130) Huang, J.; Zhang, J.; Li, Z.; Song, S.; Wu, N. Exploring Differences between Charge and Discharge of Limn2o4/Li Half-Cell with Dynamic Electrochemical Impedance Spectroscopy. *Electrochimica Acta* **2014**, *131*, 228–235. https://doi.org/10.1016/j.electacta.2014.02.030.

(131) Stoynov, Z.; Savova-Stoynov, B.; Kossev, T. Non-Stationary Impedance Analysis of Lead/Acid Batteries. *Journal of Power Sources* **1990**, *30* (1–4), 275–285. https://doi.org/10.1016/0378-7753(93)80085-4.

(132) Itagaki, M.; Honda, K.; Hoshi, Y.; Shitanda, I. In-Situ EIS to Determine Impedance Spectra of Lithium-Ion Rechargeable Batteries during Charge and Discharge Cycle. *Journal of Electroanalytical Chemistry* **2015**, *737*, 78–84. https://doi.org/10.1016/j.jelechem.2014.06.004.

(133) Huang, J.; Ge, H.; Li, Z.; Zhang, J. Dynamic Electrochemical Impedance Spectroscopy of a Three-Electrode Lithium-Ion Battery during Pulse Charge and Discharge. *Electrochimica Acta* **2015**, *176*, 311–320. https://doi.org/10.1016/j.electacta.2015.07.017.

(134) Huang, J.; Li, Z.; Zhang, J. Dynamic Electrochemical Impedance Spectroscopy Reconstructed from Continuous Impedance Measurement of Single Frequency during Charging/Discharging. *Journal of Power Sources* **2015**, *273*, 1098–1102. https://doi.org/10.1016/j.jpowsour.2014.07.067.

(135) Itagaki, M.; Kobari, N.; Yotsuda, S.; Watanabe, K.; Kinoshita, S.; Ue, M. In Situ Electrochemical Impedance Spectroscopy to Investigate Negative Electrode of Lithium-Ion Rechargeable Batteries. *Journal of Power Sources* **2004**, *135* (1–2), 255–261. https://doi.org/10.1016/j.jpowsour.2004.04.004.

(136) Itagaki, M.; Kobari, N.; Yotsuda, S.; Watanabe, K.; Kinoshita, S.; Ue, M. LiCoO2 Electrode/Electrolyte Interface of Li-Ion Rechargeable Batteries Investigated by in Situ Electrochemical Impedance Spectroscopy. *Journal of Power Sources* **2005**, *148*, 78–84. https://doi.org/10.1016/j.jpowsour.2005.02.007.

(137) Moss, P. L.; Au, G.; Plichta, E. J.; Zheng, J. P. An Electrical Circuit for Modeling the Dynamic Response of Li-Ion Polymer Batteries. *Journal of The Electrochemical Society* **2008**, *155* (12), A986–A994. https://doi.org/10.1149/1.2999375.

(138) Huang, J.; Zhang, J. Theory of Impedance Response of Porous Electrodes: Simplifications, Inhomogeneities, Non-Stationarities and Applications. *Journal of The Electrochemical Society* **2016**, *163* (9), A1983–A2000. https://doi.org/10.1149/2.0901609jes.

(139) Lin, X.; Kim, Y.; Mohan, S.; Siegel, J. B.; Stefanopoulou, A. G. Modeling and Estimation for Advanced Battery Management. *Annual Review of Control, Robotics, and Autonomous Systems* **2019**, *2* (1), 393–426. https://doi.org/10.1146/annurev-control-053018-023643.

(140) Doyle, M.; Fuller, T. F.; Newman, J. Modeling of Galvanostatic Charge and Discharge of the Lithium/Polymer/Insertion Cell. *Journal of The Electrochemical Society* **1993**, *140* (6), 1526–1533. https://doi.org/10.1149/1.2221597.

(141) Fuller, T. F.; Doyle, M.; Newman, J. Simulation and Optimization of the Dual Lithium Ion Insertion Cell. *Journal of The Electrochemical Society* **1994**, *141* (1), 1–10. https://doi.org/10.1149/1.2054684.

(142) Newman, J.; Tiedemann, Wi. Porous Electrode Theory with Battery Applications. *American Institute of Chemical Engineers Journal* **1975**, *21* (25).

(143) Boovaragavan, V.; Harinipriya, S.; Subramanian, V. R. Towards Real-Time (Milliseconds) Parameter Estimation of Lithium-Ion Batteries Using Reformulated Physics-Based Models. *Journal of Power Sources* **2008**, *183* (1), 361–365. https://doi.org/10.1016/j.jpowsour.2008.04.077.

(144) Meyers, J. P.; Doyle, M.; Darling, R. M.; Newman, J. The Impedance Response of a Porous Electrode Composed of Intercalation Particles. *Journal of The Electrochemical Society* **2000**, *147* (8), 2930–2940. https://doi.org/10.1149/1.1393627.

(145) Doyle, M.; Meyers, J. P.; Newman, J. Computer Simulations of the Impedance Response of Lithium Rechargeable Batteries. *Journal of The Electrochemical Society* **2000**, *147* (1), 99–110. https://doi.org/10.1149/1.1393162.

(146) Pathak, M.; Murbach, M. D.; Pathak, C.; Jang, T.-J.; Qi, Y.; Schwartz, D. T.; Subramanian, V. R. Fast Impedance Simulation of Lithium-Ion Batteries with Pseudo-Two Dimensional Electrochemical Models. *Journal of The Electrochemical Society* **2018**, *165* (7), A1324–A1337. https://doi.org/10.1149/2.0831805jes.

(147) Northrop, P. W. C.; Ramadesigan, V.; De, S.; Subramanian, V. R. Coordinate Transformation, Orthogonal Collocation, Model Reformulation and Simulation of Electrochemical-Thermal Behavior of Lithium-Ion Battery Stacks. *Journal of The Electrochemical Society* **2011**, *158* (12), A1461–A1477. https://doi.org/10.1149/2.058112jes.

(148) Newman, J. S.; Tobias, C. W. Theoretical Analysis of Current Distribution in Porous Electrodes. *Journal of The Electrochemical Society* **1962**, *109* (12), 1183–1191. https://doi.org/10.1149/1.2425269.

(149) Bazant, M. Z. Theory of Chemical Kinetics and Charge Transfer Based on Nonequilibrium Thermodynamics. *Accounts of Chemical Research* **2013**, *46* (5), 1144–1160. https://doi.org/10.1021/ar300145c.

(150) Guo, Y.; Smith, R. B.; Yu, Z.; Efetov, D. K.; Wang, J.; Kim, P.; Bazant, M. Z.; Brus, L. E. Li Intercalation into Graphite: Direct Optical Imaging and Cahn-Hilliard Reaction Dynamics. *Journal of Physical Chemistry Letters* **2016**, *7* (11), 2151–2156. https://doi.org/10.1021/acs.jpclett.6b00625.

(151) Shah, K.; Subramaniam, A.; Mishra, L.; Jang, T.; Bazant, M. Z.; Braatz, R. D.; Subramanian, V. R. Editors' Choice—Perspective—Challenges in Moving to Multiscale Battery Models: Where Electrochemistry Meets and Demands More from Math. *Journal of The Electrochemical Society* **2020**, *167* (13), 133501. https://doi.org/10.1149/1945-7111/abb37b.

(152) Koseoglou, M.; Tsioumas, E.; Ferentinou, D.; Jabbour, N.; Papagiannis, D.; Mademlis, C. Lithium Plating Detection Using Dynamic Electrochemical Impedance Spectroscopy in Lithium-Ion Batteries. *Journal of Power Sources* **2021**, *512*, 230508. https://doi.org/10.1016/j.jpowsour.2021.230508.

# Appendix I: Derivation of modified frequency domain equations used in the time-separated method – an example

Let us take the charge balance in a porous electrode as an example to illustrate the derivation of the modified frequency domain impedance equations. The charge balance is written as the total applied current density being the sum of current density in the solid phase and current density in the electrolyte phase.

$$-\sigma_{\mathrm{eff,p}}\left(\frac{\partial \Phi_p^s}{\partial x}\right)-\kappa_{\mathrm{eff,p}}\left(\frac{\partial \Phi_p}{\partial x}\right)+\frac{2\kappa_{\mathrm{eff,p}}RT\left(1-t_+\right)}{F}\left(\frac{\partial \ln c_p}{\partial x}\right)=I \qquad \text{(AI.1)}$$

where the variables and parameters are defined in Tables 1-4. Note that the subscript *p* here refers to the positive electrode. $\mathrm{K}_{eff,p}$ , is the effective ionic conductivity of the electrolyte that is dependent on the concentration of lithium-ions in the electrolyte, $c_p$ , by the relation

$$\begin{aligned}\kappa_{eff,p} = \varepsilon_p^{Brugg}[&4.1253*10^{-2}+5.007*10^{-4}*c_p-4.7212*10^{-7}*c_p{}^2\\ &+1.5094*10^{-10}*c_p{}^3-1.6018*10^{-14}*c_p{}^4]\end{aligned} \qquad \text{(AI.2)}$$

$c_p$ , is one of the dependent variables we are solving for and can be expanded using $c_{p,k}=c^{'}_{p,k}-jc^{''}_{p,k}$ ,

$$\begin{aligned}c_p &= \mathrm{Re}\left\{\sum\nolimits_{k=0}^{\infty} c_{p,k}\exp(jk\omega t)\right\}\\ &=\overline{c_{p,0}}+\mathrm{Re}\left\{c^{'}_{p,1}\cos(\omega t)+jc^{'}_{p,1}\sin(\omega t)-jc^{''}_{p,1}\cos(\omega t)+c^{''}_{p,1}\sin(\omega t)\right\}\\ &=\overline{c_{p,0}}+c^{'}_{p,1}\cos(\omega t)+c^{''}_{p,1}\sin(\omega t)\\ &=\overline{c_{p,0}}+c_{p,1}\end{aligned} \qquad \text{(AI.3)}$$

Note that for notation purposes, we use the expression,

$$c_{p,1}=c^{'}_{p,1}\cos(2\pi\omega_1 t')+c^{''}_{p,1}\sin(2\pi\omega_1 t') \qquad \text{(AI.4)}$$

We perform a Taylor expansion of $\mathrm{K}_{eff,p}(c_p)$ about the mean term $\overline{c_{p,0}}(x;t_b)$, which gives

$$\mathrm{K}_{eff,p} = \overline{\mathrm{K}_{eff,p,0}}(x,t_b) + \left.\frac{d\mathrm{K}_{eff,p}}{dc_p}\right|_{c_p=\overline{c_{p,0}}(x,t_b)} \mathrm{Re}\{c_{p,1}(x;\omega_1,t_b)e^{(j2\pi\omega_1 t')}\} \tag{AI.5}$$

where $\mathrm{K}_{eff,p,0}(x,t_b) = \mathrm{K}_{eff,p}\big|_{c_p=\overline{c_{p,0}}(x,t_b)}$.

We also perform a Taylor expansion of the $\dfrac{\partial ln\, c_p}{\partial x}$ term about $\overline{c_{p,0}}(x;t_b)$,

$$\frac{\partial ln\, c_p}{\partial x} = \frac{1}{c_p}\frac{\partial c_p}{\partial x} = \left[\frac{1}{\overline{c_{p,0}}} - \frac{1}{\overline{c_{p,0}}^2}c_{p,1} + \ldots\right]\frac{\partial c_p}{\partial x} \tag{AI.6}$$

We substitute Equations (A5) and (A6) into (A1) and expand accordingly, only keeping the terms that are first order with respect to $c_{p,1}$.

We use Equation (A3) on the result and collect all $\cos(2\pi\omega_1 t')$ terms as real and $\sin(2\pi\omega_1 t')$ terms as imaginary to obtain final expressions that can be found as governing equations in Table 7.

$$\frac{\partial}{\partial x}\left[\sigma_{eff,p}\frac{\partial \Phi^{s'}_{p,1}}{\partial x}\right] + \frac{\partial}{\partial x}\left[\overline{\kappa_{eff,p,0}}\frac{\partial \Phi'_{p,1}}{\partial x} + \left.\frac{\partial \kappa_{eff,p}}{\partial c_p}\right|_{c_p=\overline{c_{p,0}}} c'_{p,1}\frac{\partial \overline{\Phi_{p,0}}}{\partial x}\right]$$

$$= \frac{\partial}{\partial x}\left[\frac{2\,\overline{\kappa_{eff,p,0}}\,RT\,(1-t_+)}{F}\left\{\frac{1}{\overline{c_{p,0}}}\frac{\partial c'_{p,1}}{\partial x} - \frac{c'_{p,1}}{\overline{c_{p,0}}^2}\frac{\partial \overline{c_{p,0}}}{\partial x}\right\} + \frac{2RT(1-t_+)}{F}\left.\frac{\partial \kappa_{eff,p}}{\partial c_p}\right|_{c_p=\overline{c_{p,0}}}\frac{c'_{p,1}}{\overline{c_{p,0}}}\frac{\partial \overline{c_{p,0}}}{\partial x}\right] \tag{AI.7}$$

$$\frac{\partial}{\partial x}\left[\sigma_{eff,p}\frac{\partial \Phi^{s''}_{p,1}}{\partial x}\right] + \frac{\partial}{\partial x}\left[\overline{\kappa_{eff,p,0}}\frac{\partial \Phi''_{p,1}}{\partial x} + \left.\frac{\partial \kappa_{eff,p}}{\partial c_p}\right|_{c_p=\overline{c_{p,0}}} c''_{p,1}\frac{\partial \overline{\Phi_{p,0}}}{\partial x}\right]$$

$$= \frac{\partial}{\partial x}\left[\frac{2\,\overline{\kappa_{eff,p,0}}\,RT\,(1-t_+)}{F}\left\{\frac{1}{\overline{c_{p,0}}}\frac{\partial c''_{p,1}}{\partial x} - \frac{c''_{p,1}}{\overline{c_{p,0}}^2}\frac{\partial \overline{c_{p,0}}}{\partial x}\right\} + \frac{2RT(1-t_+)}{F}\left.\frac{\partial \kappa_{eff,p}}{\partial c_p}\right|_{c_p=\overline{c_{p,0}}}\frac{c''_{p,1}}{\overline{c_{p,0}}}\frac{\partial \overline{c_{p,0}}}{\partial x}\right] \tag{AI.8}$$

# Appendix II: Obtaining impedance governing equations – an example using the $S_{8(l)}$ molar species balance

Time domain $S_{8(l)}$ molar species balance:

$$\frac{\partial \varepsilon_c C_{S_{8(l)}}}{\partial t} = -\frac{\partial N_{S_{8(l)}}}{\partial x} + r_{S_{8(l)}} - R_{c,S_{8(l)}} \qquad \text{(AII.1)}$$

Diffusive flux of $S_{8(l)}$:

$$N_{S_{8(l)}} = -D_{eff,S_{8(l)}} \frac{\partial C_{S_{8(l)}}}{\partial x} \qquad \text{(AII.2)}$$

Generation/consumption of $S_{8(l)}$ from electrochemical reaction 2:

$$r_{S_{8(l)}} = \frac{a}{2F} i_2 \qquad \text{(AII.3)}$$

Specific interfacial area:

$$a = a_0 \left( \frac{\varepsilon_c}{1 - \varepsilon_{S8,init} - efc} \right)^{\xi} \qquad \text{(AII.4)}$$

Butler-Volmer kinetics to describe electrochemical reaction 2:

$$i_2 = i_{0,2} (C_{S_8^{2-}})^{\alpha/2} (C_{S_{8(l)}})^{(1-\alpha)/2} \left[ e^{\frac{(1-\alpha)F}{RT}\eta_2} - e^{\frac{-\alpha F}{RT}\eta_2} \right] \qquad \text{(AII.5)}$$

Overpotential of electrochemical reaction 2:

$$\eta_2 = \phi_s - \phi_e - U_2 \qquad \text{(AII.6)}$$

Equilibrium potential of electrochemical reaction 2:

$$U_2 = U_2^{\theta} - \frac{RT}{F}\left( -\frac{1}{2} ln\left[\frac{C_{S_{8(l)}}}{1000}\right] + \frac{1}{2} ln\left[\frac{C_{S_8^{2-}}}{1000}\right]\right) \tag{AII.7}$$

Generation/consumption of $S_{8(l)}$ from precipitation reaction:

$$R_{S_{8(l)}} = -k_{f,S_8}\varepsilon_{S_8}(C_{S_{8(l)}} - K_{sp,S_8}) \tag{AII.8}$$

Since we are trying to find the first order impedance which is linear, we take the Taylor expansion about the mean value for any of the nonlinear expressions – exponentials, logarithms, powers – in Equations (AII.2), (AII.4), (AII.5), and (AII.7) above. Following, to convert the time domain governing equations to the frequency domain, each dependent variable is expressed as the sum of a steady state DC component and a small perturbation term, see Equation (4.15). We also use the expressions

$$X_1 = X_1^{'} - jX_1^{"} \tag{AII.8}$$

$$X_1 = X_1^{'}\cos(\omega t) + X_1^{"}\sin(\omega t) \tag{AII.9}$$

Substituting equations (4.15) and linearized (AII.2)-(AII.8) into the overall species balance governing equation (AII.1), we can collect the first order terms and further split them up into real and imaginary components (collecting sines and cosines). The result of this time domain equation is the two frequency domain equations:

$$\begin{aligned}
&\varepsilon_{c,1}^{"}\,\omega C_{S_{8(l)},0} + \varepsilon_{c,0}\,\omega C_{S_{8(l)},1}^{"} = \frac{D_{0,S_{8(l)}}\varepsilon_{c,0}^{brug}}{L_{cat}^2}\frac{d^2 C_{S_{8(l)},1}^{'}}{dx^2} \\
&+ \frac{a_0\,\varepsilon_{c,0}^{\xi}}{(1-\varepsilon_{c,S8,init} - efc)^{\xi}}\frac{\alpha}{RT} i_{0,2}(C_{S_8^{2-},0})^{\alpha/2}(C_{S_{8(l)},0})^{(1-\alpha)/2}\left(\phi_{s,1}^{'} - \phi_{e,1}^{'} + \frac{RT}{F}\left[-\frac{C_{S_{8(l)},1}^{'}}{2C_{S_{8(l)},0}} + \frac{C_{S_8^{2-},1}^{'}}{2C_{S_8^{2-},0}}\right]\right) \\
&- k_{f,S_8}\varepsilon_{S_8,0}C_{S_{8(l)},1}^{'} - k_{f,S_8}\varepsilon_{S_8,1}^{'}(C_{S_{8(l)},0} - K_{sp,S_8})
\end{aligned} \tag{AII.10}$$

$$\begin{aligned}
&-\varepsilon'_{c,1}\,\omega C_{S_{8(l)},0}-\varepsilon_{c,0}\,\omega C'_{S_{8(l)},1}=\frac{D_{0,S_{8(l)}}\,\varepsilon_{c,0}^{brug}}{L_{cat}^{2}}\frac{d^{2}C''_{S_{8(l)},1}}{dx^{2}}\\
&+\frac{a_{0}\,\varepsilon_{c,0}^{\xi}}{(1-\varepsilon_{c,S8,init}-efc)^{\xi}}\frac{\alpha}{RT}i_{0,2}(C_{S_{8}^{2-},0})^{\alpha/2}(C_{S_{8(l)},0})^{(1-\alpha)/2}\left(\phi''_{s,1}-\phi''_{e,1}+\frac{RT}{F}\left[-\frac{C''_{S_{8(l)},1}}{2C_{S_{8(l)},0}}+\frac{C''_{S_{8}^{2-},1}}{2C_{S_{8}^{2-},0}}\right]\right)\qquad\text{(AII.11)}\\
&-k_{f,S_{8}}\varepsilon_{S_{8},0}C''_{S_{8(l)},1}-k_{f,S_{8}}\varepsilon''_{S_{8},1}(C_{S_{8(l)},0}-K_{sp,S_{8}})
\end{aligned}$$